
**Pacific Northwest
National Laboratory**

Operated by Battelle for the
U.S. Department of Energy

Intermittent Turbulence in the Very Stable Ekman Layer

J C Barnard

January 2001

Prepared for the U.S. Department of Energy
under Contract DE-AC06-76RL01830



DISCLAIMER

This report was prepared as an account of work sponsored by an agency of the United States Government. Neither the United States Government nor any agency thereof, nor Battelle Memorial Institute, nor any of their employees, makes **any warranty, express or implied, or assumes any legal liability or responsibility for the accuracy, completeness, or usefulness of any information, apparatus, product, or process disclosed, or represents that its use would not infringe privately owned rights.** Reference herein to any specific commercial product, process, or service by trade name, trademark, manufacturer, or otherwise does not necessarily constitute or imply its endorsement, recommendation, or favoring by the United States Government or any agency thereof, or Battelle Memorial Institute. The views and opinions of authors expressed herein do not necessarily state or reflect those of the United States Government or any agency thereof.

PACIFIC NORTHWEST NATIONAL LABORATORY
operated by
BATTELLE
for the
UNITED STATES DEPARTMENT OF ENERGY
under Contract DE-AC06-76RL01830

Printed in the United States of America

Available to DOE and DOE contractors from the
Office of Scientific and Technical Information,
P.O. Box 62, Oak Ridge, TN 37831-0062;
ph: (865) 576-8401
fax: (865) 576-5728
email: reports@adonis.osti.gov

Available to the public from the National Technical Information Service,
U.S. Department of Commerce, 5285 Port Royal Rd., Springfield, VA 22161
ph: (800) 553-6847
fax: (703) 605-6900
email: orders@ntis.fedworld.gov
online ordering: <http://www.ntis.gov/ordering.htm>



This document was printed on recycled paper.

INTERMITTENT TURBULENCE IN THE
VERY STABLE EKMAN LAYER

James Coles Barnard

A dissertation submitted in partial fulfillment of
the requirements for the degree of

Doctor of Philosophy

University of Washington

2000

Program Authorized to Offer Degree: Mechanical Engineering

University of Washington
Graduate School

This is to certify that I have examined this copy of a doctoral dissertation by

James Coles Barnard

and have found that it is complete and satisfactory in all respects, and that any
and all revisions required by the final examining committee have been made.

Chair of Supervisory Committee:

James J. Riley

Reading Committee:

James J. Riley

Robert A. Brown

Parker MacCready

Date:

Doctoral Dissertation

In presenting this dissertation in partial fulfillment of the requirements for the Doctoral degree at the University of Washington, I agree that the Library shall make its copies freely available for inspection. I further agree that extensive copying of this dissertation is allowable only for scholarly purposes, consistent with "fair use" as prescribed in the U.S. Copyright Law. Requests for copying or reproduction of this dissertation may be referred to Bell and Howell Information and Learning, 300 North Zeeb Road, Ann Arbor, MI 48106-1346, to whom the author has granted "the right to reproduce and sell (a) copies of the manuscript in microform and/or (b) printed copies of the manuscript made from microform."

Signature _____

Date _____

University of Washington

Abstract

INTERMITTENT TURBULENCE IN THE
VERY STABLE EKMAN LAYER

James Coles Barnard

Chairperson of the Supervisory Committee: Professor James J. Riley
Department of Mechanical Engineering

This study describes a Direct Numerical Simulation (DNS) of a very stable Ekman layer in which a constant downward heat flux is applied at the lower boundary, thus cooling the fluid above. Numerical experiments were performed in which the strength of the imposed heat flux was varied. For downward heat fluxes above a certain critical value the turbulence becomes intermittent and, as the heat flux increases beyond this value, the flow tends to relaminarize because of the very strong ambient stratification.

We adopt Mahrt's (1999) definition of the very stable boundary layer as a boundary layer in which intermittent, rather than continuous turbulence, is observed. Numerical experiments were used to test various hypothesis of where in "stability parameter space" the very stable boundary layer is found. These experiments support the findings of Howell and Sun (1999) that the boundary layer will exhibit intermittency and therefore be categorized as "very stable", when the stability parameter, z/L , exceeds unity. Another marker for the very stable boundary layer, Derbyshire's (1990) maximum heat flux criterion, was also examined.

Using a case study drawn from the simulations where turbulence intermittency was observed, the mechanism that causes the intermittence was investigated. It was found that patchy turbulence originates from a vigorous inflectional, Ekman-like instability --

a roll cell -- that lifts colder air over warmer air. The resulting convective instability causes an intense burst of turbulence. This turbulence is short-lived because the lifting motion of the roll cell, as well as the roll cell itself, is partially destroyed after the patchy turbulence is generated.

Examples of intermittent turbulence obtained from the simulations appear to be consistent with observations of intermittency even though the Reynolds number of the DNS is relatively low (400).

TABLE OF CONTENTS

List of figures	iii
List of tables.....	viii
CHAPTER 1: INTRODUCTION.....	1
1.1 The very stable Ekman layer.....	1
1.2 Turbulence in the very stable boundary layer.....	11
1.3 Issues.....	16
CHAPTER 2: DIRECT NUMERICAL SIMULATION OF THE VERY STABLE BOUNDARY LAYER – BACKGROUND AND NUMERICAL METHOD	18
2.1 Reynolds number similarity and the comparison of DNS with atmospheric measurements.....	18
2.2 Governing equations	22
2.2.1 Governing equations and boundary conditions	23
2.2.2 Nondimensionalization of the governing equations	27
2.3 Numerical method.....	30
2.3.1 Solution of the diffusive heat equation	30
2.3.2 Numerical method for the momentum and temperature perturbation equations	31
Spatial discretization – horizontal directions	33
Spatial discretization and mapping – vertical direction.....	36
Time advancement scheme	49
Summary of numerical algorithm	51
2.3.3 Assessing model performance	53
Neutral stratification.....	53

Stable stratification.....	62
The continuous spectrum of eigenvalues	64
Summary – evaluation of model performance	66
CHAPTER 3: DIRECT NUMERICAL SIMULATION OF THE VERY	
STRATIFIED EKMAN LAYER - RESULTS	68
3.1 Definition of the very stable boundary layer in terms of various stability	
parameters.....	68
3.1.1 z/Λ and the flux intermittency factor	73
3.1.2 The maximum heat flux criterion	80
3.2 Mechanisms of intermittency	88
3.2.1 Flow visualization.....	91
Flow cross sections.....	93
Mean flow visualization	105
Summary – flow visualization	107
3.2.2 A detailed exploration of the intermittency mechanism	107
Ekman layer instability.....	108
Counterclockwise rotation of the roll vortices	118
Intermittency and the inertial oscillation.....	121
Summary.....	131
CHAPTER 4: CONCLUSIONS.....	136
Bibliography.....	141
APPENDIX A: the continuous spectrum of the laminar, stratified Ekman layer	151

LIST OF FIGURES

Number	Page
<u>Figure 1</u> : The turbulent, kinematic heat flux as a function of z/L . Adapted from Mahrt (1998).	3
<u>Figure 2</u> : Flux intermittency factor for the turbulent heat flux, plotted as a function of z/L . (L is the local Obukhov length). The standard deviations of the flux intermittency factor are shown as the vertical bars with the corresponding solid symbols. From Howell and Sun (1999).	4
<u>Figure 3</u> : The modeled boundary layer height, h , and the Monin-Obukhov length, L , as a functions of B_0/B_{\max} . The symbols \ddot{y} , x , and Δ refer to, respectively, a large eddy simulation, a gradient-transport model, and a second-order closure model. Figure from Derbyshire (1990).	7
<u>Figure 4</u> : Time series of vertical velocity standard deviation (top panel); dissipation rate (middle panel), and temperature variance dissipation rate (lower panel). The measurements are from a minisodar and are for two nights; the height of the measurements is 36 m. The curves represent a 20-min running mean. (Figure from Coulter, 1990).	15
<u>Figure 5</u> : A test of Nieuwstadt's (1984) local scaling hypothesis using the stably stratified DNS of Coleman et al. (1992). (a) Gradient Richardson number; (b) RMS velocity fluctuations, solid and dashed lines are total and vertical velocity fluctuations, respectively; (c) RMS temperature fluctuations; (d) eddy viscosity, the dashed and solid lines are two definitions of eddy viscosity. \ddot{y} ; Nieuwstadt's (1984) unfiltered data; $\bar{\cdot}$, filtered data.	22

Figure 6: Time series of the friction velocity, u_* / G (top panel), and the angle, \mathbf{b} , that the surface stress vector makes with the geostrophic wind (bottom panel)..... 55

Figure 7: Three components of the Reynolds stress; $-\langle uv \rangle$ is solid line —; $-\langle vw \rangle$ is dashed line -----, $-\langle uv \rangle$ is dotted line; x -axis is aligned with geostrophic wind. The top panel depicts Reynolds stress from this study while the bottom panel is from Coleman et al. (1990b) 59

Figure 8: One-dimensional energy spectrum for the vertical velocity, w . The spectrum is taken in a direction parallel to the x -axis. 60

Figure 9: Contour plot of the vertical velocity, w , at a height $z/D = 0.03$ 62

Figure 10: Part of the eigenvalue spectrum derived from a linear stability analysis of the laminar Ekman layer. The dots are the continuous spectrum while the circled dots represent the discrete spectrum. The dashed lines are a closed- form solution for the continuous spectrum, with $Pr = 0.7$ 65

Figure 11: Time series of the surface friction velocity, u_* / G . The times series are plotted for three values of the bulk Richardson number, Ri_b . The surface heat flux is turned on at time $tf = 15$. The case $Ri_b = 0.001$ only extends to time $tf = 45$ 70

Figure 12: Time series of the \mathbf{b} , the angle that the surface stress makes with the geostrophic wind. Three time series are plotted corresponding to Ri_b equal to 0.001, 0.004, and 0.005. The case $Ri_b = 0.001$ extends only to $tf = 45$ 71

Figure 13: Kinematic turbulent heat flux, $Ri_b = 0.005$ 72

Figure 14: Flux intermittency factor as a function of the stability parameter, z/L . The flux intermittency factor is flat over a wide range of the stability parameter and only begins to increase for $z/L > 1$. (This figure is taken from Howell and Sun, 1999). 75

<u>Figure 15</u> : Flux intermittency factor, I_f , calculated from the DNS simulations.....	78
<u>Figure 16</u> : The gradient Richardson number plotted versus the local stability parameter, z/L (adapted from Nieuwstadt, 1984). The curve is from a model based on the local scaling theory while the filled circles with error bar represent values of the gradient Richardson number derived from field studies.	79
<u>Figure 17</u> : The imposed surface heat flux (dashed line) and the interior turbulent heat flux (dots) plotted versus Ri_b . A smooth curve has been fit to the turbulent heat flux points.	85
<u>Figure 18</u> : Detailed view of the surface friction velocity (u_*/G) and the angle that the surface stress makes with the geostrophic wind, \mathbf{b}	93
<u>Figure 19</u> : The upper panel shows the vertical velocity measured at a height of $z/D = 0.751$ in a stably stratified flow while the bottom panel shows the vertical velocity, measured at the same height, in a neutrally stratified flow.....	94
<u>Figure 20</u> : The top panel shows a cross section of the temperature in the $y-z$ plane with the wind components (v, w) indicated by the vectors, $tf = 39.5$. Contours of w are shown in the bottom panel in an $x-y$ plane at a height of $z/D = 1.38$, and the vectors depict the wind components (u, v)	97
<u>Figure 21</u> : Same as Figure 20, but $tf = 40.0$	99
<u>Figure 22</u> : Same as Figure 20, but $tf = 40.50$	100
<u>Figure 23</u> : Same as Figure 20, but $tf = 41.0$	101
<u>Figure 24</u> : Same as Figure 20, but $tf = 41.75$	102
<u>Figure 25</u> : Same as Figure 20, but $tf = 42.0$	103
<u>Figure 26</u> : Same as Figure 20, but $tf = 42.1$	104

<u>Figure 27</u> : Vertical cross section of the flow, $tf = 42.5$. The roll cell responsible for the patchy turbulence seen in the previous figures, positioned above $y = 13$, is beginning its decay.....	104
<u>Figure 28</u> : The top panel contains profiles of the mean flow component u while the bottom panel contains profiles of the mean flow component v	106
<u>Figure 29</u> : Comparison between four variables derived from linear stability theory (lines) and from the simulations (black dots). The variables are the roll cell orientation, \mathbf{e}_r ; the roll cell wavenumber, $\mathbf{a} = 2\mathbf{p}/\mathbf{l}$, where \mathbf{l} is the roll cell's wavelength; the phase speed, and the growth rate.	115
<u>Figure 30</u> : Cross sections of the flow in the y,z plane at time $tf = 42.10$. The vectors show the v, w components of the flow and the black lines are approximate representation of the flow streamlines. The upper panel is the total flow (mean + perturbation) while the bottom panel is the perturbation flow	120
<u>Figure 31</u> : Surface friction velocity, u_* / G , and the angle that the surface stress makes with the geostrophic wind, \mathbf{b} , for the test simulation in which the inertial oscillation is erased.	123
<u>Figure 32</u> : Vertical velocity contours for the TS runs (inertial oscillation removed). The top panel shows the vertical velocity, w , contoured in the $y-z$ plane, and the bottom panel shows w contoured in the $x-y$ plane. Note the regular structure of these cells.....	124
<u>Figure 33</u> : Time integrated terms of the mean flow kinetic energy balance. The top panel shows the balance with the inertial oscillation present, while the bottom panel shows the balance without the oscillation.	126
<u>Figure 34</u> : Profiles of the v -component of the mean flow plotted for various times. For the sake of comparison, the v -component of the laminar Ekman layer is shown by the dashed line.	128

Figure 35: The top panel shows the TKE while the bottom panel shows the various terms in the vertically integrated TKE equation. These quantities have been derived from our case study with $Ri_b = 0.005$ 131

Figure 36: Top panel is a running standard deviation of dimensional width 20 minutes applied to the vertical velocity time series shown in Figure 19. The middle panel is the same for vertical velocities measured at a calibrated height of 34 meters, and the bottom panel (from Coulter, 1990) represents the same quantity, but derived from observations at a height of about 36 meters 134

LIST OF TABLES

Number	Page
<u>Table 1</u> : Observations of sporadic turbulence in the stable boundary layer. (Adapted from ReVelle [1993]).	14
<u>Table 2</u> : Scales of the dependent and independent variables	28
<u>Table 3</u> : Coefficients for time advancement scheme	50
<u>Table 4</u> : Numerical parameters for neutrally stratified model runs	54
<u>Table 5</u> : Values of the friction velocity, u_* / G , and the stress angle, \mathbf{b} , for various model runs.	56
<u>Table 6</u> : Growth rates from model and linear stability theory, $Re = 400$, $Pr = 0.7$.	63
<u>Table 7</u> : Average turbulent fluxes and flux standard deviations as functions of the bulk Richardson number, Ri_b .	86

ACKNOWLEDGMENTS

The author wishes to thank the many people who made this study possible. Professor Jim Riley provided constant encouragement, expert technical advice, and occasional prodding without which this thesis would not have been possible. I am grateful to Dr. Lee Harrison who suggested that I obtain a PhD. I am also indebted to Dr. Ralph Foster with whom I had many enlightening conversations and will have many similar conversations in the future.

My colleagues at Pacific Northwest National Laboratory (PNNL) provided continuing encouragement with this endeavor. I cannot provide sufficient thanks to John Schmelzer, Chris Doran, Dave Whiteman, Elaine Chapman, Rich Barchet, Carl Berkowitz, Don Slater, Will Shaw, Signe Wurstner, Erik Pearson, and Larry Wendell.

My parents, brother and sister are to be profusely thanked, too, for helping me through this long process, which was occasionally an ordeal! And, of course, Dave Stangland, Joe Eckerle, and Michael Beard provided constant and abiding friendship throughout my lengthy trudge through academia.

Parts of this research were supported by the U.S. Department of Energy and for this support I am grateful.

DEDICATION

To MGH

To all tortoises – Part II

CHAPTER 1: INTRODUCTION

The Ekman layer serves as a prototype for the boundary layer of the ocean and atmosphere. Because of its relevance to these geophysical flows, the Ekman layer has been the focus of many studies since the formulation of the laminar theory in 1905 (Ekman, 1905). In the past few decades, Ekman's original focus on the laminar boundary layer has been greatly expanded to examine more realistic models of geophysical boundary layers in which turbulence and thermal stratification play major roles. These studies are obviously important in their own right as inquiries into fundamental fluid mechanics, and from a more practical point of view, they support engineering work that might, for example, look at the important problem of diffusion of contaminants in stably stratified atmospheric boundary layers (e.g., Kemp and Thomson, 1996; Gryning, 1999; Rao; 1999). The engineer's need to understand how stable thermal stratification affects the geophysical (Ekman) boundary layer continues to motivate many studies of oceanic and atmospheric boundary layers. As one may expect, the strength (and vertical extent) of the stratification exerts considerable governance over the dynamics of the stratified Ekman layer. The very stable Ekman layer, with its potential for varied physical phenomena including intermittent turbulence (Mahrt, 1985; Mahrt, 1998), boundary layer collapse, and propagation of gravity waves (Einaudi and Finnigan, 1981; Finnigan and Einaudi, 1981) perhaps poses the greatest challenge to the boundary layer research community. This challenge is just now being addressed.

1.1 THE VERY STABLE EKMAN LAYER

The very stable boundary layer (VSBL) may be identified in terms of the unique physical phenomena that are frequently witnessed under very stable conditions.

Perhaps the characteristic that most distinguishes the VSBL from its less stable counterpart is the intermittent nature of turbulence (Mahrt, 1999). Because intermittency is such an important feature of the very stable regime, a stable boundary layer may be considered as “very stable” when intermittent turbulence is observed. This intermittent nature stands out in marked contrast to the continuous state of turbulence found in weakly stable and moderately stable boundary layers.

The line between the various stability regimes may be characterized by the value of a suitably chosen stability parameter. The stability parameter z/L was considered by Mahrt (1998) and Mahrt et al. (1998) in an analysis using data from the MICROFRONTS project conducted in Kansas, March 1995 (described in part in Howell and Sun, 1999). This parameter forms an important part of Monin-Obukhov similarity theory (Garratt, 1992) and it is composed of the height above the ground, z , and L , the Monin-Obukhov (MO) length, $L = -u_*^3 / \mathbf{k} \frac{g}{\mathbf{q}_0} \overline{w'q'}$. In the expression for L , \mathbf{k} is the Von Karman constant, g is the gravitational constant, \mathbf{q}_0 is the reference potential temperature, and u_* and $\overline{w'q'}$ are the surface friction velocity and surface temperature flux, respectively.

Based on the value of z/L , Mahrt et al. (1998) classified the stable boundary into three regimes. The weakly stable regime is defined roughly as range of values, z/L , such that $0 < z/L < \mathbf{e} \ll 1$, where \mathbf{e} is the maximum stability for the weakly stable regime. In this regime, the magnitude of the downward turbulent heat flux *increases* with increasing z/L . For the MICROFRONTS data, \mathbf{e} is about equal to 0.05 at $z = 10$ m (see Figure 1, adapted from Mahrt 1998. In this figure a downward heat flux is defined as being negative so that flux becomes *more negative* as z/L increases in the weakly stable regime.). As noted by Mahrt et al. (1998), the exact value of \mathbf{e} may not be universal. For stability parameters in a “transition” range $\mathbf{e} < z/L < O(1)$, the

downward heat flux *decreases* with increasing stability. This range of stability is also termed moderately stable regime. The point $z/L = O(1)$ demarks the stability at which the VSBL begins. In the VSBL, the turbulent heat flux is small and continues to decrease as z/L becomes even larger.

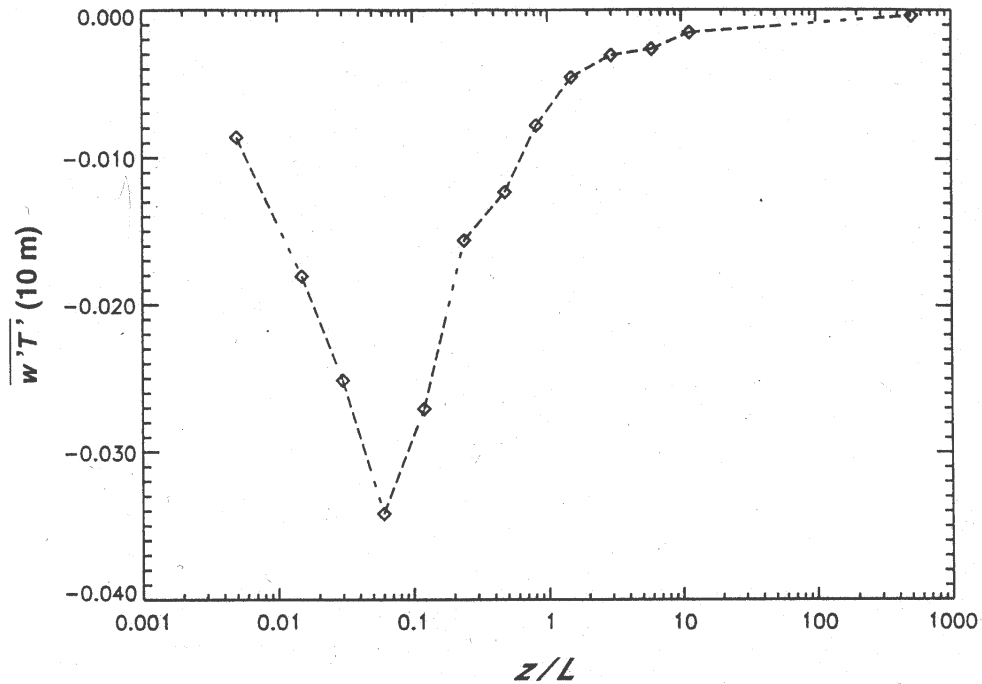


Figure 1: The turbulent, kinematic heat flux as a function of z/L . Adapted from Mahrt (1998).

That the magnitude of the downward turbulent heat flux reaches a maximum as the stability increases and then declines with further increases in stratification is easily explained. At one extreme, neutral stratification, the turbulence may be very vigorous but no heat is transported because the potential temperature fluctuations upon which the turbulence acts are essentially zero. In other words, the turbulence merely pushes

around air, all of the same potential temperature, and no heat is transported. At the other extreme a strong potential temperature gradient will completely extinguish the means of transporting heat -- the turbulence -- and no heat transport is possible. Between these two extremes, a combination of turbulence and temperature gradient exists that maximizes the downward transport of heat.

Support for Mahrt et al.'s (1998) assertion that intermittency, and therefore the VSBL, occurs when $z/L \geq 1$ comes from observational evidence. Some of this evidence is displayed in Figure 2, taken from Howell and Sun (1999). This figure shows a flux

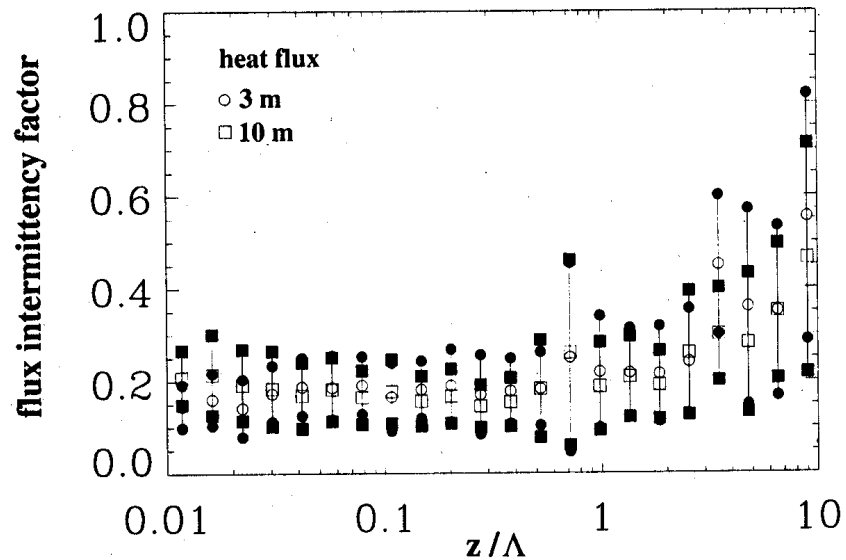


Figure 2: Flux intermittency factor for the turbulent heat flux, plotted as a function of z/L . (L is the local Obukhov length). The standard deviations of the flux intermittency factor are shown as the vertical bars with the corresponding solid symbols. From Howell and Sun (1999).

intermittency factor plotted versus local stability parameter, z/L . The local Obukhov length, L , is calculated in terms of local turbulent fluxes instead of the values very close to the surface. Because Mahrt et al. (1998) calculated L from fluxes at a height of 10 meters, it is very likely true that $L(10 \text{ meters}) = L$ (from Mahrt et al., 1998) and, for all practical purposes, we can substitute z/L for z/L in this figure..

The flux intermittency factor is a measure of how much the flux varies over an interval of 10 minutes. A value of zero means that the flux was constant over the interval, while a value approaching one implies significant intermittency. Because we associate flux intermittency with the VSBL, the identification of the range of z/L over which the intermittency factor begins to increase towards a value of one also uncovers the range of z/L over which we classify the boundary layer as being very stable. Clearly, as shown in Figure 2, the intermittency increases dramatically only after z/L exceeds one, and these data support the proposition that the VSBL exists for stability parameters (z/L) greater than one. That the very stable regime has turbulence properties significantly different from the weakly stable regime is also supported by the wind tunnel experiment of Ohya et al. (1997) and in the observations of Smedman (1988).

It is also possible to demarcate the very stable regime from the moderately stable regime using a maximum heat flux criterion developed by Derbyshire (1990). In contrast to the observational work presented above, Derbyshire's criterion stems solely from theory. Such theory is related to the intuitive notion that the atmosphere can handle only so much surface cooling until the ambient stratification becomes strong enough to cause the properties of the turbulence to undergo a change from continuous to sporadic turbulence. For sufficiently strong cooling, the turbulence may cease entirely.

In somewhat more quantitative terms, the theory can be viewed in the following manner. A downward surface heat flux is imposed at the lower boundary of the atmosphere. This flux is made progressively larger. When this downward heat flux exceeds a critical value, B_{\max} , continuous turbulence ceases, and it is replaced by intermittent turbulence. Thus, B_{\max} may be considered as a boundary separating the VSBL from the moderately stable boundary layer. For typical mid-latitude conditions, Derbyshire (1990) calculated B_{\max} to be about 40 W/m^2 -- a magnitude that seems very reasonable. This heat flux may be interpreted as the maximum surface heat flux for which continuous turbulence is maintained; for fluxes larger than this maximum, turbulence in the boundary layer may become intermittent and ultimately the boundary layer may collapse.

Support for the maximum heat flux concept comes from modeling studies presented in Derbyshire (1990). For example, Figure 3 (adapted from Derbyshire, 1990) shows the height of the stable Ekman layer derived from three models plotted versus an imposed surface heat flux, expressed as B_0/B_{\max} . The models here: (1) a large eddy simulation (LES) - indicated in the figure by the symbol, \ddot{y} ; (2) a gradient-transport model (GTM) indicated by an "x"; and (3) the second-order closure model of Brost and Wyngaard (1978), represented by the triangle, Δ . Unfortunately, few details regarding the GTM model are given in Derbyshire (1990). The LES model is that described in Mason and Derbyshire (1990).

In the model runs depicted in Figure 3, either a constant cooling rate or a constant heat flux was specified at the lower boundary. As expected, Figure 3 shows a decrease in height, h , of the stable Ekman layer as the downward heat flux increases for all three models. The various lines in this figure are Derbyshire's extension of Nieuwstadt's (1984, 1985) stable boundary layer theory to span the range between very stable and neutral flow. The different lines correspond to different calibrations of the theory.

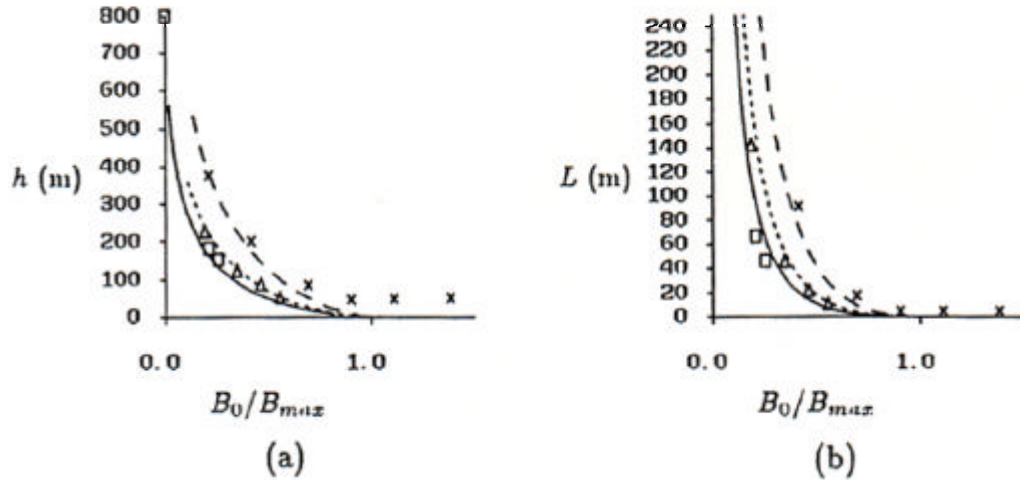


Figure 3: The modeled boundary layer height, h , and the Monin-Obukhov length, L , as a functions of B_0/B_{max} . The symbols \square , \times , and Δ refer to, respectively, a large eddy simulation, a gradient-transport model, and a second-order closure model. Figure from Derbyshire (1990).

The theory agrees with the models reasonably well. Considering the models and theory together, one could conclude that the boundary layer height tends to zero as B_0/B_{max} goes to one. This collapse in height is best interpreted as the cessation of continuous turbulence and/or the collapse of the entire boundary layer. The only contravening evidence to this picture is the behavior of the GTM for $B_0/B_{max} > 1$. In this parameter range, the boundary layer height in the GTM model assumes a constant value greater than zero and the turbulence is highly intermittent. (In support of this finding, we note that the data analysis of Arya [1981] suggests that, for very stable boundary layers, collapse does not occur.) Despite the divergence of the GTM

behavior from the rest of the models, the overall results support the hypothesis that turbulence within the boundary layer undergoes a significant change as B_0/B_{\max} tends to one, and the change is one from continuous to intermittent turbulence. We repeat that this intermittency is the characteristic “signature” of the VSBL and, therefore, the specification of $B_0/B_{\max} = 1$ as the point separating the moderately stable and very stable regimes seems justified.

However, the specification of the boundary between moderately stable and very stable in terms of a maximum downward heat flux seems to contradict the observations of Mahrt et al. (1998). In terms of stability, they found that the point of the maximum downward turbulent heat flux, $z/L = e \ll 1$, was the upper limit of a weakly stable regime in which no intermittency is evident. Also, their analysis indicates that the onset of the VSBL occurs only when z/L exceeds one, at which point *the heat flux is much less than its maximum*. In contrast, Derbyshire asserts that the beginning of the very stable regime coincides with the maximum heat flux. These two placements of the maximum heat flux, one defining the boundary between weakly stable and moderately stable, and the other defining the boundary between stable and very stable, pose a seeming contradiction (see Mahrt et al., 1998).

However, there are four caveats that bear on this apparent contradiction and these must be addressed. The first of these is that the observations are from one field study only, and conclusions drawn from just a single study are not always reliable. In fact, as stated by Mahrt et al. (1998), “there is no evidence that the value of z/L corresponding to the maximum downward heat flux is universal.” Perhaps measurements from another field study would show something different; for example, maybe the boundary layer would show very stable behavior as the heat flux approached a maximum.

Second, the comparison between the models and the observations could be flawed because of the lower boundary condition applied to the models: either a constant heat

flux or a constant cooling rate (i.e., $dq/dt = -\text{constant}$). These boundary conditions are tied to the interior of the model using the traditional Monin-Obukhov heat and temperature profiles. Whether these profiles are valid for moderate to very stable conditions is questionable. Mahrt (1999) and Högström (1996) are some of the more recent papers that raise uncertainty about the use of standard Monin-Obukhov theory for the more stable regimes. If for strong stability Monin-Obukhov similarity breaks down as suggested by the available evidence, then the connection of lower boundary condition to the model will be defective, perhaps leading to serious errors in the model simulations, such as a collapse of the boundary layer.

Third, the model simulations could be seriously in error and therefore misleading. For example, one potential source of major errors in LES is the poor resolution of the “large eddies” near the surface. Close to the surface the large eddies scale with the height above the surface, z , and these eddies will be underresolved; moreover, as thermal stratification reduces the length scale of the turbulence ($\approx L$), the lack of resolution close to the wall¹ and elsewhere is exacerbated. The poor resolution of the turbulent eddies near the wall may increase flux errors, which in turn, worsen the coupling of the boundary conditions with the interior of the model so that the entire simulation feels the effect of the near-wall resolution problems. In an effort to alleviate these difficulties, Brown et al. (1994) added a backscatter term (Mason and Thompson, 1992) to the original stable LES model of Mason and Derbyshire (1990). The backscatter² may ameliorate resolution problems, and hence simulations from LES models with backscatter are presumably more reliable proxies of reality than models

¹ Engineers like to refer to solid boundaries as “walls”.

² In the turbulent energy cascade, energy is transferred from larger eddies to smaller eddies. Some stochastic “backscatter” of energy occurs that transfers energy to larger scales, but in the mean this “upscale” transfer is less than the downscale transfer so that the net transfer is still from larger to smaller eddies. Adding a backscatter feature to a subgrid scale model presumably makes it more realistic.

without this feature. (Although we must be mindful that backscatter itself cannot solve all the resolution woes; for example, the ability of LES to predict gradients in the near-wall region depends also upon the type of subgrid parameterization chosen for the LES [Khana and Brasseur, 1997]). For the present we shall assume that the backscatter improves model simulations directly in the near-wall region, and therefore indirectly throughout the whole modeling domain. Yet, even when this improvement is added to an LES, the height of the boundary layer still tends to zero as B_0/B_{\max} became close to one (see Figure 1d in Brown et al., 1994). Thus, the evidence from the improved LES model still supports the conclusion that the boundary layer fundamentally changes as $B_0/B_{\max} \rightarrow 1$.

Finally, for a given value of the heat flux, Figure 1 indicates that *two* values of the stability parameter (falling in one of the two ranges: $z/L < e$ [weakly stable] or $z/L > e$ [moderately to very stable]) may be associated with any *one* value of heat flux. The possibility of two solutions for a given heat flux was noted by De Bruin (1994) and observations that bolster this proposition have been described by Malhi (1995). McNider et al. (1995) also examined the predictability of the stable boundary layer using tools from non-linear dynamics and they, too, noted the dual nature of the solutions. That is, for a range of some external parameters, the stable boundary layer could exist in two possible states. Perhaps the modeling results presented in Derbyshire (1990), Mason and Derbyshire (1990), and Brown et al. (1994) have tracked only one of the two solutions. Whether Derbyshire's model-based conclusions would have been different had the models tracked the other solution remains unknown. At this time, we don't know if the models are capable of uncovering the other solution or not³.

³ The reason why the models preferred one solution over the other is probably related to the initial condition: neutrally stratified flow. It is well known that nonlinear systems are sensitive to initial conditions, and if one had substituted a strongly stratified initial condition for the original (neutral) initial condition, the model integration may have locked onto the second solution.

The fact that we cannot reconcile a prediction derived from theory with the observations is emblematic of our general lack of knowledge of both the VSBL and the modeling of this boundary layer. Indeed, the divergence between the observations (Mahrt, 1998; Mahrt et al., 1998; Howell and Sun, 1999) and models (Mason and Derbyshire, 1990; Derbyshire, 1990) calls into question our very ability to model VSBLs at all (for example, see Mahrt [1998]). Clearly, if we are to enhance our understanding of the VSBL through the use of models, then we must strive to understand the ills of the existing models, and develop new models in which these ills are alleviated. We also need to understand more about the nature of the VSBL itself. For example, is Monin-Obukhov theory applicable to the surface layer? Or indeed, does a surface layer exist at all? These questions, as well as many others, remain unanswered.

1.2 TURBULENCE IN THE VERY STABLE BOUNDARY LAYER

The cause of the turbulence intermittency found in the VSBL is another important issue that remains unresolved. Unlike turbulence found in slightly stable boundary layers, the turbulence in the VSBL is presumed to be intermittent in both space and time; and as we have emphasized above, this intermittency is *the* defining characteristic of the VSBL. That the turbulence is sporadic has been documented in many field studies and various theoretical efforts have attempted to explain the intermittency. Riley and Lelong (2000) have examined various aspects of turbulence in stable conditions. ReVelle (1993) has reviewed theories of sporadic turbulence as well as some of the field observations in which sporadic turbulence and bursting phenomena are observed. These theories include the mechanism of Blackadar (1979), various gravity wave phenomena in the boundary layer including critical layer absorption (see for example, Nappo, [1991]; Winters and D'Asaro [1989]; Winters and D'Asaro [1994]; Lombard and Riley, [1996a, 1996b]; Dörnbrack, [1998]), Kelvin-

Helmholtz (K-H) instabilities (Drazin and Reid, 1989), the so-called “upside down boundary layer (Mahrt, 1999; Smedman, 1988), and the formation of roll vortices (Thorpe and Guymmer, 1977). The physical principles underlying these phenomena are well known, although sometimes the name associated with the principle is not. For example, when one hears of the “Blackadar mechanism”, one might not know that this name is associated with the classic way that sporadic turbulence is generated in the stable boundary layer.⁴ Therefore we shall describe this mechanism as well the related idea of the upside-down boundary layer.

The Blackadar mechanism is based on a Richardson number modulation of the flow, where it is assumed that turbulence ceases when the critical value of the gradient Richardson number is exceeded. Here the gradient Richardson number, Ri , is defined

in the customary manner, $Ri = \frac{g}{\mathbf{q}_o} \left(\frac{\partial \mathbf{q}}{\partial z} \right) / \left(\frac{\partial u}{\partial z} \right)^2$. In the early evening hours, once

the surface heating by solar radiation has ceased, the bottom of the boundary layer is cooled by the emission of long-wave radiation to space. This cooling leads to enhanced stability in the lower part of the boundary layer, which in turn, may cause Ri in this part of the boundary layer to exceed the critical value, Ri_c , usually assumed to be close to the classical, inviscid value of $1/4$. Turbulence is therefore shut off. Surface drag is no longer transmitted to the interior of the flow because of the cessation of turbulence adjacent to the surface. The resulting imbalance of the drag, pressure gradient, and Coriolis forces accelerates the interior flow leading to a nocturnal jet.

The picture now is one of little or no turbulence in a region close to the surface, and the formation of a nocturnal jet above the area of diminished turbulence. As the jet gains strength, the shear below the jet increases and the Richardson number may again

⁴ This mechanism was also described by Businger in 1973 and in the author’s opinion it could just as well be called the “Businger mechanism”.

fall below the critical value and turbulence emerges just below the jet. This picture describes the “upside down” boundary layer described by Smedman (1988). Eventually the turbulence below the jet may make its way to the ground, and the quiescent flow near the ground then becomes turbulent again. Surface drag is now effectively transmitted through the boundary layer and the shear tends to decrease, and in some parts of the boundary layer, Ri again exceeds Ri_c and the turbulence stops, and the process repeats. This cycle of the buildup and decrease of shear resulting in Richardson number swings through Ri_c leads to sporadic turbulence in the boundary layer.

Given a particular set of turbulence observations in which intermittency is evident, it often cannot be readily determined if the Blackadar mechanism described above leads to the intermittency, or whether another mechanism is responsible. Part of the problem in choosing one mechanism over another is the fact that the observations are always spatially and temporally limited and the entire boundary layer is not “seen” and therefore important information is missing that may allow the mechanism to be identified. Despite this problem, a number of field studies in which sporadic turbulence has been found have attempted to ascribe a cause to the intermittency.

ReVelle (1993) summarizes some of the field studies in which turbulent bursting is observed; see Table 1 below (adapted from ReVelle, 1993). In this table, a “burst” means a period of turbulence in an otherwise quiescent flow, and the duration of the burst is simply the duration of the turbulence. These observations of bursting occur on temporal and spatial scales that are thought to be small compared to the scales of the entire boundary layer. With this scale difference in mind, these specialized observations must be kept distinct from more generic observations of the stable boundary layer in which coarser scale properties are measured and described, such as the mean temperature and wind profiles. (See, for example, Mahrt [1985]; Sorbjan, [1988]).

Table 1: Observations of sporadic turbulence in the stable boundary layer. (Adapted from ReVelle [1993]).

Source	Duration of calm periods (min)	Total burst duration (min)	Average Number of bursts per night
Nappo (1991)	15-19	15	13-18
Schubert (1977)	150	15	3
Coulter (1990)	> 360	15	3

The observations referred to in Table 1 were taken over flat terrain. (although Nappo [1991] includes some observations in complex terrain; these observations have been excluded from Table 1). The measurements of Schubert (1977) were obtained from a combination of acoustic sounder and anemometers deployed at two levels on a tall tower. The anemometer measurements at the upper level indicate a windiness that occurs throughout the entire evening while the wind measurements at lower level clearly show quiescent periods interspersed with turbulent bursts. He conjectured that the bursts were caused by something akin to the Blackadar mechanism. Coulter (1990) used acoustic means (a minisodar) to probe the boundary layer, but he attributed the presence of sporadic turbulence to Kelvin-Helmholtz (K-H) waves (although he left some room for alternative explanations). From an array of masts instrumented with anemometers and temperature sensors, Nappo devised a simple analysis to detect the turbulent bursts. Nappo speculated that such bursts were probably responsible for most of transport of atmospheric pollutants (in particular ozone, see Harrison et al., 1978) to the ground. He went on to note that such bursts

would not be handled well by traditional numerical models. The nature of the instrumentation -- a point measurement of wind and temperature -- did not provide enough information to ascertain what was causing the intermittency.

A vivid example of turbulence intermittency is depicted in Figure 4 taken from Coulter (1990). This figure shows several bursts of turbulence of duration 15-30 minutes during the course of one night (although data from two nights are shown in the figure). Reading the panels from top to bottom, this figure shows the standard deviation of the vertical velocity, the dissipation rate, and the temperature variance dissipation rate. For

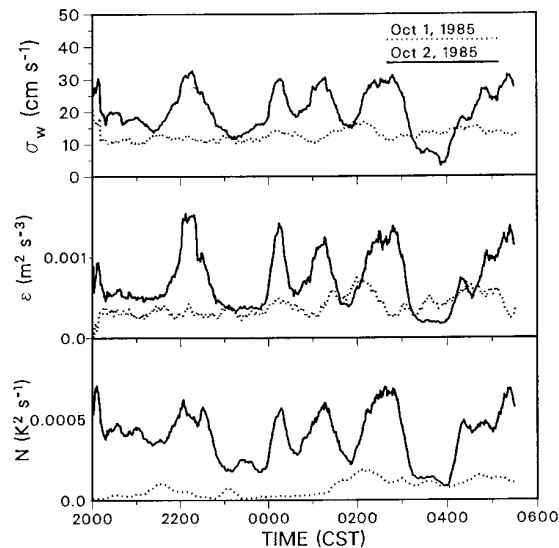


Figure 4: Time series of vertical velocity standard deviation (top panel); dissipation rate (middle panel), and temperature variance dissipation rate (lower panel). The measurements are from a minisodar and are for two nights; the height of the measurements is 36 m. The curves represent a 20-min running mean. (Figure from Coulter, 1990).

the night of October 2, the sporadic nature of the turbulence is very evident as shown by the marked variation in these quantities with time. Obviously, intermittency is a real observable phenomenon in the stable boundary layer. It is interesting to note that the ambient meteorological conditions for the nights of October 1st and 2nd are very similar; yet, in one night, sporadic turbulence occurred, while during the other night it was absent. There is no explanation for this curiosity.

1.3 ISSUES

The discussion above has served to highlight just a few of the important issues regarding the flow associated with the VSBL. We have seen that our understanding of the VSBL, as well as our ability to model it, is so primitive that even resolving different claims over the role of the maximum heat flux in delineating the start of the VSBL is an unsolved problem. Because of our very modest level of understanding the VSBL we can only devise for ourselves a set of simple, but very important, research goals.

This first of our goals is fundamental to understanding the VSBL: how do we mark off the boundaries of the VSBL in the parameter spaces of various stability parameters? As previously discussed Derbyshire (1990) used the surface heat flux as a proxy for the stability of the boundary layer. He then set the beginning of the VSBL at the maximum imposed surface heat flux for which continuous turbulence could be supported. For fluxes greater than this maximum heat flux, modeling studies indicated that the turbulence became intermittent, and in some cases the turbulence as well as the boundary layer collapsed. In contrast, the approach of Mahrt et al. (1998) was based almost entirely on observations, and they found that the point of maximum heat flux separates a weakly stable and moderately stable boundary layer. Based on this finding it seems that the maximum flux cannot be associated with start of the VSBL, in contradiction to conjecture of Derbyshire. The confusion witnessed here stems from

the two approaches based either on theory and modeling, or based on observations. The contradictory results from these approaches motivate us to examine these issues: What are good working values, in terms of various stability parameters, of where the very stable regime begins? And, is the demarcation of the VSBL in stability parameter space applicable to both models and observations.

The next issue we wish to explore -- and this is the crux of this study -- is the mechanisms associated with the formation of sporadic turbulence in the VSBL. We have already mentioned several ways speculated to cause that turbulence intermittency over flat terrain. The observations in which intermittency occurs are too sparse and incomplete to permit the identification of the exact cause of the intermittency and therefore our understanding of a cause (or causes) remains inadequate. Because of the limitations inherent to observational studies (i.e., lack of spatial and temporal coverage, and the inability to measure all variables of concern), we will resort to a modeling study and model the flow using a Direct Numerical Simulation (DNS) of turbulence. The DNS is designed for the highly idealized flow of an Ekman boundary layer over flat terrain with an imposed downward surface heat flux. By varying the strength of this flux, we can vary the stability of the modeled atmosphere and observe how the stability affects the turbulence, and attempt to ferret out the mechanism responsible for the intermittent nature of turbulence in the VSBL.

CHAPTER 2: DIRECT NUMERICAL SIMULATION OF THE VERY STABLE BOUNDARY LAYER – BACKGROUND AND NUMERICAL METHOD

We are proposing to investigate the VSBL using a DNS of a very stable Ekman layer. The DNS technique avoids some of the pitfalls of other models because all scales of turbulence are resolved from the molecular dissipation scale to the largest eddies. Thus, there is no need to apply an *ad hoc* subgrid scale (SGS) model to drain down the energy of the large eddies⁵ as is done in an LES. (Rogallo and Moin [1984] review the differences between LES and DNS. For a more recent evaluation of the LES technique, see Mason [1994]). For the VSBL, the DNS seems indispensable because as mentioned by Derbyshire (1999) many phenomena seen in VSBLs such as sporadic breakdowns have not yet been seen in LESs of moderately stable boundary layers. Moreover, the inability of present LES technology to simulate the VSBL has recently been underscored in an article by Saiki et al. (2000). (See also Kosovic and Curry (2000) for another example of recent LES modeling applied to stable boundary layers). One goal of the Saiki et al. study was to use LES to model the VSBL but attempts to realize this goal failed. This failure led the authors to conclude that in order to simulate the VSBL a better SGS model is needed.

2.1 REYNOLDS NUMBER SIMILARITY AND THE COMPARISON OF DNS WITH ATMOSPHERIC MEASUREMENTS

The DNS technique resolves all scales of turbulence without the need for an artificial SGS model. Of course, if we choose to resolve the smallest, dissipation scales of turbulence, then we are limited by computational resources on how large a domain we

may model and this restriction implies that DNS can only model flows at low Reynolds number, Re . Despite the restriction to low Reynolds number, the DNS technique has been applied to both laboratory and geophysical flows. Recently, it has been possible to match the Reynolds number of a laboratory flow with that of a DNS (de Bruyn Kops and Riley, 1998) and the correspondence between the DNS and measurements was extremely good. Such good agreement can only buttress our faith in the DNS method. In an apparently less realistic application, the DNS method has been applied to flows with large Reynolds number including Ekman layers. In these simulations the DNS can be thought of as an approximation to the actual, high Reynolds number flow, and the hope is that some of the important flow features of the high Reynolds number flow will show up relatively intact in a low Reynolds number DNS. Put in other terms, since the Reynolds number of the DNS is high enough to permit turbulent flow, we hope that to some degree the concept of “Reynolds number similarity” holds (Townsend, 1980), which would imply that flow phenomena captured in the DNS are Reynolds number independent (or approximately so). Therefore, if such similarity holds, then results derived for low Reynolds simulations can be generalized to higher Reynolds number.

Coleman (1999) has suggested that Reynolds number similarity is apparent even at the low Reynolds number of current DNSs and therefore, a DNS may be applicable to flows with much larger Re . In his study, DNSs for neutrally stratified Ekman layers at Reynolds numbers equal to 400, 500, and 1000 were compared with laboratory studies of Ekman layers (e.g., Caldwell et al., 1972) as well as various LES runs (Andr n and Moeng, 1993; Andr n et al., 1994). When total stress profiles from the three DNSs are plotted in appropriate scaled nondimensional coordinates a near collapse of the profiles is evident. (The total stress, \mathbf{t} , is defined as $\mathbf{t} = \sqrt{\mathbf{t}_x^2 + \mathbf{t}_y^2}$, where \mathbf{t}_x and \mathbf{t}_y are down- and cross-stream components of the horizontal stress.) This collapse indicates the near

⁵ The subgrid model for the DNS can be viewed as being molecular viscosity; this model is correct

independence of the stress magnitude to Re , i.e., Reynolds number similarity is emerging even at these low Reynolds numbers. From an intuitive standpoint this seems utterly remarkable given the relatively low Reynolds number (400) of one of the model runs!

Additional evidence of Reynolds number similarity can be seen in a series of three papers {Coleman et al., 1990a, 1992, 1994}, in which a neutrally stratified, a stably stratified, and a convective Ekman layer are simulated, respectively, using the DNS technique. These studies illustrate in greater detail some of the strengths and limitations of using DNS to understand various aspects of the higher Reynolds number flow for which the DNSs serves as proxies. For example, both the neutral DNS and convective DNS are relevant to an investigation of the conditions that encourage the formation of roll vortices in the boundary layer. Etling and Brown (1993) have reviewed the mechanisms suspected to be responsible for the development of such vortices: dynamic instabilities (inflection-point and parallel) associated with the background mean flow (an Ekman layer), and thermal instabilities. There is still a question concerning the relative importance of these mechanisms in instigating and maintaining the vortices, and perhaps DNS can provide insight into this problem. In the DNS simulations, roll vortices were only observed in convective conditions for moderate heating rates (as depicted by stability parameter z_i/L , where z_i is the inversion height); no vortices were present in the neutral case. The simulations therefore suggest that the thermal instability is more important than the dynamic instabilities. (Indeed, evidences of vortices are most often observed in moderately convective circumstances such as cold air outbreaks over the ocean; see Hartman et al., 1997). But here we run into the questions imposed, in part, by the low Reynolds number of the neutral DNS runs: Is the development of roll vortices in the neutral simulation hindered by the low Reynolds number of the simulation? At the present time, this question cannot be

everywhere in the modeling domain.

answered and, in this respect, the conclusions drawn from the DNS are equivocal, although the emergence of Reynolds number similarity exhibited in Coleman (1999) suggest that the Reynolds number is not a major factor for neutrally stratified flow.

The stably stratified simulations of Coleman et al. (1992) were performed for light to moderate thermal stratification and hence, they are not representative of the very stable case that we are concerned with here. However, Coleman et al.'s (1992) simulation illustrates again the usefulness of a low Reynolds number DNS as a tool for making sense of its large Reynolds number counterpart. One important theoretical concept of the stable boundary layer is "local scaling" (Nieuwstadt, 1984) in which appropriately nondimensionalized turbulent quantities (e.g., variances and covariances) become functions of z/L only, where L is a *local* Monin-Obukhov length, defined in terms of the local heat flux and local friction velocity. Such a scaling seems intuitively plausible because under very stratified conditions the vertical inhibition of transport by the stratification implies that the turbulence should only depend on local conditions.

Figure 5 shows an example of local scaling applied to one of Coleman et al.'s (1992) DNS runs with relatively low stratification. As mentioned by Coleman et al., the mild stratification of the DNS runs and the low Reynolds number make the test of local scaling tenuous. Given these rigorous conditions the agreement between modeled and measured results is surprisingly good for two of the four variables modeled, the gradient Richardson number (panel "a" in Figure 5) and the RMS velocity fluctuations (panel "b"). If a comparison between Nieuwstadt's (1984) so-called "filtered data"⁶ and the RMS temperature fluctuations is made, then agreement between the modeled and observed variables for this quantity also becomes good. Considering the comparison portrayed in Figure 5 we may conclude that local scaling holds up reasonably well even in a low Reynolds number DNS.

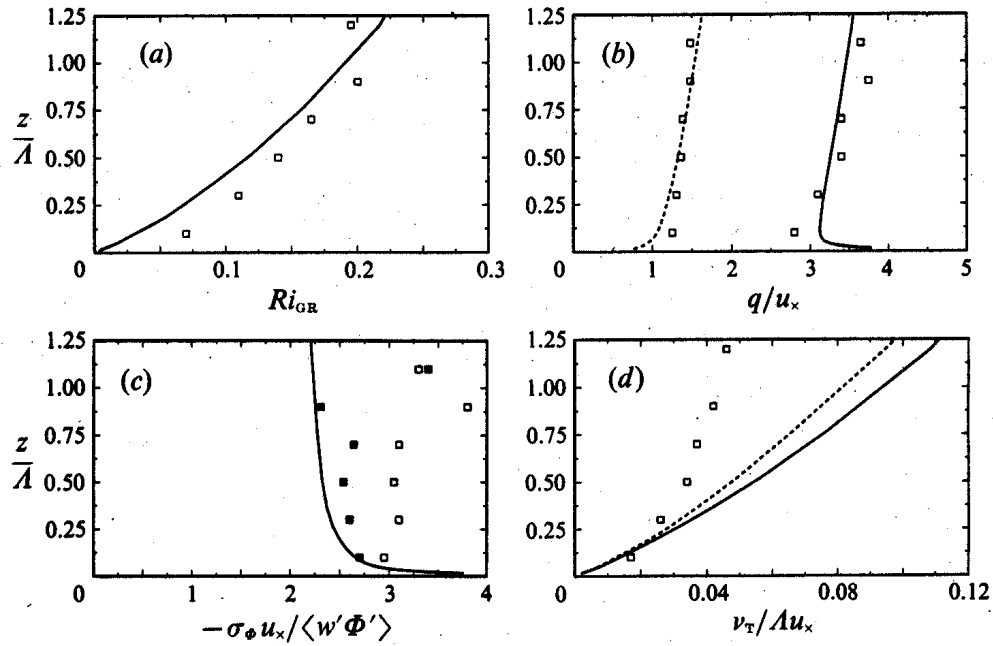


Figure 5: A test of Nieuwstadt's (1984) local scaling hypothesis using the stably stratified DNS of Coleman et al. (1992). (a) Gradient Richardson number; (b) RMS velocity fluctuations, solid and dashed lines are total and vertical velocity fluctuations, respectively; (c) RMS temperature fluctuations; (d) eddy viscosity, the dashed and solid lines are two definitions of eddy viscosity. $\check{\nu}$; Nieuwstadt's (1984) unfiltered data; \square , filtered data.

2.2 GOVERNING EQUATIONS

The evidence supporting Reynolds number similarity even at relatively low Re , as well as the generally favorable comparison between the simulation results and data, bolster

⁶ The filtered data was composed by running a high-pass filter through the original data set to remove, as well as possible, contamination by gravity waves.

confidence in the low Reynolds number DNS as a description of idealized boundary layer flows with much larger Reynolds numbers. We now describe the construction of the DNS including the presentation of the governing equations and the description of the numerical methods used to solve these equations.

2.2.1 GOVERNING EQUATIONS AND BOUNDARY CONDITIONS

The governing equations of the flow considered here are derived from the Navier-Stokes equations, the continuity equation for incompressible flow, and the energy equation for incompressible flow⁷; these are

$$\frac{D\mathbf{u}}{Dt} = -\frac{1}{\mathbf{r}}\nabla p + 2\mathbf{O}\times(\mathbf{G}-\mathbf{u}) - \mathbf{g} + \mathbf{n}\nabla^2\mathbf{u} \quad (2.1)$$

$$\nabla\cdot\mathbf{u} = 0 \quad (2.2)$$

$$\frac{\partial\Theta}{\partial t} + \nabla\cdot(\mathbf{u}\Theta) = \mathbf{k}\nabla^2\Theta \quad (2.3)$$

where \mathbf{u} is the vector of velocity components (u , v , w), \mathbf{W} is the rotation rate of the system aligned along the positive z -axis, \mathbf{G} is the geostrophic wind in the direction of the positive x -axis, Θ is the (potential) temperature, \mathbf{n} and \mathbf{k} are the kinematic viscosity and thermal diffusivity, respectively, and \mathbf{r} is the fluid density. The substantial derivative, Du/Dt is defined in the usual manner

$$\frac{Du}{Dt} = \frac{\partial u}{\partial t} + u\frac{\partial u}{\partial x} + v\frac{\partial u}{\partial y} + w\frac{\partial u}{\partial z} \quad (2.4)$$

Below, we shall link the temperature and density together through the Boussinesq approximation; this linkage closes the set of equations listed above.

The Ekman flow is driven by a uniform pressure gradient, $\partial p_E/\partial y$, along the positive y -axis (p_E is the pressure associated with this uniform gradient),

$$0 = -\frac{1}{\mathbf{r}} \frac{\partial p_E}{\partial y} + 2\mathbf{W} \times \mathbf{G} \quad (2.5)$$

and this pressure gradient can be subtracted from the momentum equation to yield:

$$\frac{D\mathbf{u}}{Dt} = -\frac{1}{\mathbf{r}} \nabla p - 2\mathbf{O} \times \mathbf{u} - \mathbf{g} + \eta \nabla^2 \mathbf{u} \quad (2.6)$$

where the constant pressure gradient has been removed from the pressure gradient term in the momentum equation, eq. 2.1 (To avoid the proliferation of symbols, we shall retain p as the symbol for pressure in the eq. 2.5, although this “new” pressure does not include p_E .)

For our model simulations, we are using a constant heat flux, B_0 , as the lower boundary condition. To implement this boundary condition, we first define the total temperature as a sum of three terms:

$$\Theta = \Theta_0 + \Theta_d(z, t) + \Theta'(x, y, z, t) \quad (2.7)$$

where Θ_0 is a constant background temperature, $\Theta_d(z, t)$ is a “diffusive” component of the temperature, to be defined shortly, and $\Theta'(x, y, z, t)$ is a temperature perturbation. We can substitute the expression for Θ into the energy equation, and in a manner analogous to regular perturbation theory, split the equation into two components, one for the diffusive component,

$$\frac{\partial \Theta_d}{\partial t} = \mathbf{k} \frac{\partial^2 \Theta_d}{\partial z^2} \quad (2.8)$$

⁷ Derivation of the energy equation appropriate for incompressible flow is discussed in Panton (1984).

and a companion equation for the perturbation component,

$$\frac{\partial \Theta'}{\partial t} + \nabla \cdot (\mathbf{u}\Theta') + w \frac{\partial \Theta_d}{\partial z} = \mathbf{k} \nabla^2 \Theta' \quad (2.9)$$

The splitting of the total temperature into Θ_d and Θ' is merely done for convenience in satisfying the lower boundary condition. For Θ' a no-flux boundary condition is imposed at $z = 0$ and the surface heat flux boundary condition, $-k \frac{\partial \Theta_d}{\partial z} = H_0$, is applied to find Θ_d (k is the thermal conductivity, and H_0 is the surface heat flux). At $z = \infty$, both temperatures must tend to zero. With the initial condition, $\Theta_d(z, t = 0) = 0$, eq. 2.7 is easily solved for Θ_d . We note that with these boundary conditions the temperature perturbation, Θ' , is subject to diffusive as well as advective transport everywhere except very close to the surface.

Using the definition of the total temperature (eq. 2.6) we can apply the Boussinesq approximation (Tritton, 1988; Brown, 1974) to the vertical component of the momentum equation. First, following the Boussinesq approximation we assume that density variations are only important in the buoyancy term of vertical momentum equation and that density variations may be related to fluctuations in temperature by the relation $\frac{\Delta \Theta}{\Theta_0} = -\frac{\Delta \mathbf{r}}{\mathbf{r}_0}$, where $\Delta \Theta$ ($\ll \Theta_0$) and $\Delta \mathbf{r}$ ($\ll \rho_0$) represent fluctuations in temperature and density, and \mathbf{r}_0 is the background density. Invoking these approximations, the vertical momentum equation may be written

$$\frac{Dw}{Dt} = -\frac{1}{\mathbf{r}_0} \frac{\partial p}{\partial z} + g \frac{(\Theta_0 + \Theta_d + \Theta')}{\Theta_0} + \nu \nabla^2 w \quad (2.10)$$

Defining a slowly varying hydrostatic pressure, $p_h(z,t)$, that satisfies the equation

$$-\frac{1}{\mathbf{r}_0} \frac{\partial p_h}{\partial z} + g \frac{(\Theta_0 + \Theta_d)}{\Theta_0} = 0 \quad (2.11)$$

we may define the total pressure, p , as $p = p_h(z,t) + p'(x,y,z,t)$, where p' is the perturbation pressure. Subtracting eq. 2.11 from eq. 2.10 yields the Bossinesq form of the vertical momentum equation

$$\frac{Dw}{Dt} = -\frac{1}{\mathbf{r}_0} \frac{\partial p'}{\partial z} + g \frac{\Theta'}{\Theta_0} + \nu \nabla^2 w \quad (2.12)$$

We briefly digress to mention that neither the perturbation pressure, p' nor the perturbation temperature, Θ' is necessarily zero when averaged over a horizontal plane. Denote the horizontal average with brackets, $\langle \rangle$. To find the average, of say p' over a horizontal plane, $\langle p' \rangle$, we integrate in this manner:

$$\langle p' \rangle = \lim_{L_x, L_y \rightarrow \infty} \frac{1}{L_x} \frac{1}{L_y} \int_{x=-L_x/2}^{x=L_x/2} \int_{y=-L_y/2}^{y=L_y/2} p'(x,y,z) dx dy \quad (2.13)$$

A diagnostic equation for $\langle p' \rangle$ may be found by assuming horizontal homogeneity and taking the horizontal average of eq. 2.12; this gives, with $\langle w \rangle = 0$

$$\left\langle \frac{\partial w^2}{\partial z} \right\rangle = -\frac{1}{\mathbf{r}_0} \left\langle \frac{\partial p'}{\partial z} \right\rangle + g \left\langle \frac{\Theta'}{\Theta_0} \right\rangle \quad (2.14)$$

We may now summarize the dimensional form of the governing equations for momentum as

$$\frac{Du}{Dt} = -\frac{1}{\mathbf{r}_0} \frac{\partial p'}{\partial x} + \mathbf{n} \nabla^2 u + fv \quad (2.15)$$

$$\frac{Dv}{Dt} = -\frac{1}{r_0} \frac{\partial p'}{\partial y} + \mathbf{n} \nabla^2 v - fu \quad (2.16)$$

$$\frac{Dw}{Dt} = -\frac{1}{r_0} \frac{\partial p'}{\partial z} + \mathbf{n} \nabla^2 w + g \frac{\Theta'}{\Theta_0} \quad (2.17)$$

where f is the Coriolis parameter ($= 2W$). The additional governing equations are the continuity equation, $\nabla \cdot \mathbf{u} = 0$, and the two energy equations, eq. 2.8 and eq. 2.9. The unknowns are the three components of the velocity, u, v, w ; the perturbation pressure, p' and the diffusive temperature, Θ_d ; and the perturbation temperature, Θ' . The background density, r_0 , is a specified parameter, as are f , g , κ , and ν . We therefore have a closed system of six equations and six unknowns. The boundary conditions for the temperatures Θ' and Θ_d have been described above, and the velocity components must satisfy the no-slip condition at the surface, and as $z \rightarrow \infty$, we have $(u, v, w) = (\mathbf{G}, 0, 0)$. Because the model domain must be finite in the x and y directions, periodic boundary conditions are applied for all variables in these directions. The application of periodic boundary conditions presumes that the modeling domain is sufficiently large in the two horizontal directions to capture the largest eddies of the flow. That this condition is satisfied has been discussed in Coleman et al. (1990b).

2.2.2 NONDIMENSIONALIZATION OF THE GOVERNING EQUATIONS

The governing equations may be nondimensionalized in the conventional manner by finding appropriate scales for the independent and dependent variables. We first provide scales for the independent variables, length and time. The customary length scale for the laminar Ekman layer, D , is given by $\sqrt{2\nu/f}$ (Tritton, 1988) and we adopt this as the length scale of the flow. An appropriate time scale is D/G , where G is the magnitude of the geostrophic wind. It is important to realize that alternative length and time scales exist that are also appropriate for Ekman layers. For example, a customary

length scale for the neutrally stratified turbulent Ekman layer is u_* / f , (Tennekes and Lumley, 1989) where u_* is the surface friction velocity. An alternative time scale is $1/f$. Occasionally the results from the model simulations are best cast in terms of these scales and we will advise the reader when such scales are used. Table 2 lists the scales for the independent and dependent variables.

Table 2: Scales of the dependent and independent variables

variable	scale
Length (x,y,z)	$\sqrt{2n/f} = D$
Time (t)	D/G
Velocity (u,v,w)	G
Pressure, p'	$\rho_0 G^2$
Temperature, Θ' and Θ_d	$D \frac{\partial \Theta_d}{\partial z} \Big _{surface} \left(= \frac{ B_0 D}{k} \right)$

Using these scales, the equations easily are nondimensionalized (where we have again dropped the primes and all variables are nondimensional unless otherwise noted)

$$\frac{Du}{Dt} = -\frac{\partial p}{\partial x} + \frac{1}{\text{Re}} \nabla^2 u + \frac{1}{\text{Ro}} v \quad (2.18)$$

$$\frac{Dv}{Dt} = -\frac{\partial p}{\partial y} + \frac{1}{\text{Re}} \nabla^2 v - \frac{1}{\text{Ro}} u \quad (2.19)$$

$$\frac{Dw}{Dt} = -\frac{\partial p}{\partial z} + \frac{1}{\text{Re}} \nabla^2 w + \text{Ri}_b \Theta \quad (2.20)$$

$$\nabla \cdot \mathbf{u} = 0 \quad (2.21)$$

$$\frac{\partial \Theta_d}{\partial t} = \frac{1}{\text{RePr}} \frac{\partial^2 \Theta_d}{\partial z^2} \quad (2.22)$$

$$\frac{\partial \Theta}{\partial t} + \nabla \cdot (\mathbf{u}\Theta) + w \frac{\partial \Theta_d}{\partial z} = \frac{1}{\text{RePr}} \nabla^2 \Theta \quad (2.23)$$

where Re and the Prandtl number, Pr, are defined in the usual manner, $\text{Re} = GD/\mathbf{n}$, and $\text{Pr} = \mathbf{n}/\mathbf{k}$. In this particular instance the Rossby number G/fD , is equal to exactly one-half the Reynolds number, so once the Reynolds number is specified, the Rossby number is known. The bulk Richardson number, Ri_b , is defined as

$$\text{Ri}_b = \frac{\frac{g}{\Theta_0} \left(\frac{\partial \Theta_d}{\partial z} \Big|_{\text{surface}} \right)_{\text{dim}}}{\left(\frac{G}{D} \right)^2} \quad (2.24)$$

In the definition of the bulk Richardson number, the temperature derivative is a dimensional temperature derivative (hence the subscript “dim”) and this derivative is linearly proportional to the surface heat flux. With the temperature scale defined in Table 2, the lower boundary condition on the diffusive temperature is

$$\frac{\partial \Theta_d}{\partial z} \Big|_{\text{surface}} = H_0 = 1 \quad (2.25)$$

where H_0 is the nondimensional surface heat flux, and the derivative $\partial \Theta_d / \partial z \Big|_{\text{surface}}$ is formed from the nondimensional variables Θ_d and z . With this definition of H_0 the nondimensional heat flux is always a constant equal to one. This amounts to nondimensionalizing the surface heat flux with the scale kD/Θ_s , where Θ_s is the temperature scale. The effects of the variable *dimensional* heat flux enter into the

model equations only through the bulk Richardson number such that variations in the Ri_b are linearly proportional to variations in the surface heat flux.

2.3 NUMERICAL METHOD

2.3.1 SOLUTION OF THE DIFFUSIVE HEAT EQUATION

The solution of the diffusive heat equation (eq 2.22) can be found independently from the remainder of the governing equations and we present the solution here. Given the lower boundary condition eq. 2.25 and the initial condition $\Theta_d(z, t = 0) = 0$, the heat diffusion equation is easily solved using standard methods; we get

$$\Theta_d(t, z) = -2\sqrt{\frac{t}{\text{RePr}p}} \exp\left(-\frac{\text{RePr}}{t} \frac{z^2}{4}\right) + z \operatorname{erfc}\left(\sqrt{\frac{\text{RePr}}{t}} \frac{z}{2}\right) \quad (2.26)$$

where erfc is the complementary error function. The derivative of Θ_d with respect to z is a component of eq. 2.23 and this derivative is easily calculated:

$$\frac{\partial \Theta_d}{\partial z} = \operatorname{erfc}\left(\sqrt{\frac{\text{RePr}}{t}} \frac{z}{2}\right) \quad (2.27)$$

Note that the derivative is always positive implying that temperature increases upward, which implies the downward transfer of heat from the atmosphere to the surface; i.e., the atmosphere is being cooled. Note also that at $z = 0$ the derivative is one and thus the lower boundary condition, eq. 2.25, is satisfied.

2.3.2 NUMERICAL METHOD FOR THE MOMENTUM AND TEMPERATURE PERTURBATION EQUATIONS

The numerical technique is fully spectral in all three spatial dimensions and third-order accurate in time. The technique is exhaustively described in Coleman et al. (1990b). However, because we are addressing a different problem than Coleman et al., some modification of their method is needed to fit our unique problem. In terms of model physics, the difference between our problem and that examined by Coleman et al. manifests itself in the lower boundary condition for temperature. In Coleman et al., the surface temperature was held fixed whereas we are specifying a constant heat flux at the surface. There are also further changes that stem from the need to provide more vertical resolution in the interior of the fluid than was specified in Coleman et al. Because the exposition of the numerical method in Coleman et al. is very detailed, we shall simply outline our strategy here with a special emphasis on the modifications required to accommodate the above changes.

The numerical method employs a weighted-residual Galerkin technique and has been described in the literature in many places, for example see Spalart et al. (1991) and Canuto et al. (1988). A unique feature of the method is the expansion of the velocity component in terms of non-divergent basis functions that automatically satisfy the boundary conditions and the continuity equation. The fact that the continuity equation is automatically satisfied means that there is no need to calculate the pressure through, say, an unwieldy Poisson equation. This results in a large savings of computer time and significantly reduces the complexity of the code.

It is convenient to cast the equations in terms of variables that satisfy homogeneous boundary conditions at the surface and at the top of the modeling domain, or $z = \infty$. (We have already stated that periodic boundary conditions are applied to all variables in the horizontal directions.) The temperature perturbation, Θ' , already satisfies

homogeneous boundary conditions for there is a no-flux requirement specified at the surface while as $z \rightarrow \infty$, Θ' must tend to zero. The vertical component of the velocity, w , conforms to homogeneous boundary conditions; obviously w is zero at the surface and at $z = \infty$. Thus, we must only examine the variables u and v . We introduce computational variables u^* and v^* such that these variables are deviations from the laminar Ekman solution; to wit, $u = e^{-z}(1 - \cos(z)) + u^*$ and $v = e^{-z} \sin(z) + v^*$ ⁸. Such variables obviously satisfy the requirements of homogeneity. We label the two components of the laminar Ekman solution as $U_{BS} (= e^{-z}(1 - \cos(z)))$ and $V_{BS} (= e^{-z} \sin(z))$. Substituting the expressions for u and v into the three momentum equations and the temperature perturbation equation yields

$$\frac{Du^*}{Dt} = -\frac{\partial p}{\partial x} + \frac{1}{\text{Re}} \nabla^2 u^* + \frac{1}{\text{Ro}} v^* - \left(U_{BS} \frac{\partial u^*}{\partial x} + V_{BS} \frac{\partial u^*}{\partial y} + w \frac{dU_{BS}}{dz} \right) \quad (2.28)$$

$$\frac{Dv^*}{Dt} = -\frac{\partial p}{\partial y} + \frac{1}{\text{Re}} \nabla^2 v^* - \frac{1}{\text{Ro}} u^* - \left(U_{BS} \frac{\partial v^*}{\partial x} + V_{BS} \frac{\partial v^*}{\partial y} + w \frac{dV_{BS}}{dz} \right). \quad (2.29)$$

$$\frac{Dw}{Dt} = -\frac{\partial p}{\partial z} + \frac{1}{\text{Re}} \nabla^2 w + \text{Ri}_b \Theta - \left(U_{BS} \frac{\partial w}{\partial x} + V_{BS} \frac{\partial w}{\partial y} \right) \quad (2.30)$$

$$\frac{\partial \Theta}{\partial t} + \nabla \cdot (\mathbf{u}\Theta) + w \frac{\partial \Theta_d}{\partial z} = \frac{1}{\text{RePr}} \nabla^2 \Theta - \left(U_{BS} \frac{\partial \Theta}{\partial x} + V_{BS} \frac{\partial \Theta}{\partial y} \right) \quad (2.31)$$

and, of course, the continuity equation applies to the computational variables such that $\partial u^*/\partial x + \partial v^*/\partial y + \partial w/\partial z = 0$. Finally, the non-linear part of the momentum equations may be written in vector form as $\mathbf{u} \cdot \nabla \mathbf{u} = \mathbf{w} \times \mathbf{u} + \nabla \mathbf{u} \cdot \mathbf{u}/2$, where \mathbf{w} is the vorticity ($\nabla \times \mathbf{u}$). This ‘‘rotational’’ formulation is advantageous for several reasons. First, the

⁸ Remember that z has already been nondimensionalized by D .

rotational form conserves kinetic energy for inviscid flow (see Canuto et al., 1988, page 208). Second, the rotational form explicitly includes vorticity, which is a strong indicator of turbulence, and therefore the rotational form is presumed to be better for simulating turbulent flows. We define a new pressure, $p^* = p + \mathbf{u} \cdot \mathbf{u}/2$, and the equations can be cast into their final form⁹

$$\frac{\partial u^*}{\partial t} + NL^x = -\frac{\partial p^*}{\partial x} + \frac{1}{\text{Re}} \nabla^2 u^* + \frac{1}{\text{Ro}} v^* - \left(U_{BS} \frac{\partial u^*}{\partial x} + V_{BS} \frac{\partial u^*}{\partial y} + w \frac{dU_{BS}}{dz} \right) \quad (2.32)$$

$$\frac{\partial v^*}{\partial t} + NL^y = -\frac{\partial p^*}{\partial y} + \frac{1}{\text{Re}} \nabla^2 v^* - \frac{1}{\text{Ro}} u^* - \left(U_{BS} \frac{\partial v^*}{\partial x} + V_{BS} \frac{\partial v^*}{\partial y} + w \frac{dV_{BS}}{dz} \right) \quad (2.33)$$

$$\frac{\partial w}{\partial t} + NL^z = -\frac{\partial p^*}{\partial z} + \frac{1}{\text{Re}} \nabla^2 w + \text{Ri}_b \Theta - \left(U_{BS} \frac{\partial w}{\partial x} + V_{BS} \frac{\partial w}{\partial y} \right) \quad (2.34)$$

where $(NL^x, NL^y, NL^z) = \mathbf{w} \times \mathbf{u}$; i.e., the vector NL represents the three components of the non-linear terms. It is interesting to note that if the non-linear terms are dropped from eqs. (2.28-2.31) and we set $\partial \Theta_d / \partial z$ equal to one, we obtain the linear stability equations for the stratified Ekman layer with the Brunt-Väisälä frequency, N , ($= \frac{g}{\Theta_0} \left(\frac{\partial \Theta_d}{\partial z} \right)_{\text{dim}}$) constant throughout the flow.

Spatial Discretization – Horizontal Directions

Given periodic boundary conditions, we may take the Fourier transform of the above equations (eqs. 2.31 –2.34) in the horizontal directions to obtain semi-discrete equations. More formally, this may be thought of a Galerkin process where the dependent variables are expanded in a terms Fourier basis (test)

⁹ It may seem gratuitous to again list the equations; these numerous listings are motivated by clarity.

functions, $\mathbf{f}_{k_x, k_y}(x, y) = e^{-i\frac{2\mathbf{p}k_x}{L_x}x} e^{-i\frac{2\mathbf{p}k_y}{L_y}y}$; where, k_x and k_y are integer wavenumbers, i is $\sqrt{-1}$, and L_x and L_y are the lengths of the modeling domain in the x - and y -directions, respectively. For the rest of this study, we shall assume that $L_x = L_y = L$. The expansion is merely a two-dimensional Fourier series of finite length

$$u(x, y, z, t) = \sum_{k_x, k_y} \hat{u}(k_x, k_y, z, t) e^{-i\frac{2\mathbf{p}k_x}{L}x} e^{-i\frac{2\mathbf{p}k_y}{L}y} \quad (2.35)$$

where the “^” over the variables denotes the Fourier coefficient of the variable. In the Galerkin formulation the trial functions, \mathbf{y}_{k_x, k_y} , are simply the complex conjugate of the test functions. Substituting the Fourier expansions for the variables in the governing equations, and then taking the inner product of the equation with a given trial function yields an equation discretized by wavenumber in Fourier space. For example, we have for the \mathbf{k}^{th} component of the w -momentum equation

$$\begin{aligned} \frac{\partial \hat{w}_{\mathbf{k}}}{\partial t} + \mathbf{N}L^z_{\mathbf{k}} = & \\ -\frac{\partial \hat{p}_{\mathbf{k}}^*}{\partial z} + \frac{1}{\text{Re}} \left(\frac{\partial^2}{\partial z^2} - \left(\frac{2\mathbf{p}|\mathbf{k}|}{L} \right)^2 \right) \hat{w}_{\mathbf{k}} + \text{Ri}_b \hat{\Theta}_{\mathbf{k}} & \quad (2.36) \\ - \left(U_{BS} \left(-i \frac{2\mathbf{p}k_x}{L} \hat{w}_{\mathbf{k}} \right) + V_{BS} \left(-i \frac{2\mathbf{p}k_y}{L} \hat{w}_{\mathbf{k}} \right) \right) & \end{aligned}$$

where the boldface, \mathbf{k} , is the vector (k_x, k_y) . The other momentum equations and the temperature equation can be discretized in a similar manner; see Coleman et al. (1990b) for details.

A clever trick introduced by Leonard and Wray (1982) decomposes the Fourier transformed velocity components in a “+” vector and a “-” vector and this decomposition leads to the use of non-divergent basis functions which, in turn,

eliminates the need to find the pressure explicitly. First we define horizontal components of the velocity parallel and perpendicular to the wavevector (Spalart et al., 1991)

$$\hat{u}_{\mathbf{k}}^{\square} = \frac{k_x \hat{u}_{\mathbf{k}}^* + k_y \hat{v}_{\mathbf{k}}^*}{|\mathbf{k}|} \quad \hat{u}_{\mathbf{k}}^{\perp} = \frac{-k_y \hat{u}_{\mathbf{k}}^* + k_x \hat{v}_{\mathbf{k}}^*}{|\mathbf{k}|} \quad (2.37)$$

Using these components the U^+ and U^- vector modes are defined as $(\hat{u}_{\mathbf{k}}^{\square}, 0, w)$ and $(0, \hat{u}_{\mathbf{k}}^{\perp}, 0)$, respectively. In Fourier space the continuity equation may be written as

$$-i \frac{2\mathbf{p}}{L} |\mathbf{k}| \hat{u}_{\mathbf{k}}^{\square} + \frac{\partial \hat{w}_{\mathbf{k}}}{\partial z} = 0 \quad (2.38)$$

and we see that only the U^+ mode is involved in the continuity equation. The U^- mode is not part of the continuity equation and the velocity component $\hat{u}_{\mathbf{k}}^{\perp}$ must only satisfy the boundary conditions, while $\hat{u}_{\mathbf{k}}^{\square}$ and w must satisfy not only the boundary conditions but the continuity equation as well.

For the sake of completeness, we list the equations for $\hat{u}_{\mathbf{k}}^{\square}$, $\hat{u}_{\mathbf{k}}^{\perp}$, $\hat{w}_{\mathbf{k}}$, and $\hat{\Theta}_{\mathbf{k}}$, for $\mathbf{k} \neq 0$, (and we drop the superscript “*” on the pressure terms)

$$\begin{aligned} & \frac{\partial \hat{u}_{\mathbf{k}}^{\square}}{\partial t} + \frac{k_x \square NL^x_{\mathbf{k}} + k_y \square NL^y_{\mathbf{k}}}{|\mathbf{k}|} = \\ & i \frac{2\mathbf{p}}{L} |\mathbf{k}| \hat{p}_{\mathbf{k}} + \frac{1}{\text{Re}} \left(\frac{\partial^2}{\partial z^2} - \left(\frac{2\mathbf{p} |\mathbf{k}|}{L} \right)^2 \right) \hat{u}_{\mathbf{k}}^{\square} \\ & + \frac{1}{\text{Ro}} \hat{u}_{\mathbf{k}}^{\perp} + \left(i \frac{2\mathbf{p} |\mathbf{k}| U_{BS}^{\square}}{L} \hat{u}_{\mathbf{k}}^{\square} - \hat{w}_{\mathbf{k}} \frac{dU_{BS}^{\square}}{dz} \right) \end{aligned} \quad (2.39)$$

$$\begin{aligned} \frac{\partial \hat{u}_k^\perp}{\partial t} + \frac{k_x \hat{NL}_k^y - k_y \hat{NL}_k^x}{|\mathbf{k}|} = \\ \frac{1}{\text{Re}} \left(\frac{\partial^2}{\partial z^2} - \left(\frac{2\mathbf{p}|\mathbf{k}|}{L} \right)^2 \right) \hat{u}_k^\perp - \frac{1}{\text{Ro}} \hat{u}_k^\square + \left(i \frac{2\mathbf{p}|\mathbf{k}|U_{BS}^\square}{L} \hat{u}_k^\perp - \hat{w}_k \frac{dU_{BS}^\perp}{dz} \right) \end{aligned} \quad (2.40)$$

$$\begin{aligned} \frac{\partial \hat{w}_k}{\partial t} + \hat{NL}_k^z = \\ - \frac{\partial \hat{p}_k}{\partial z} + \frac{1}{\text{Re}} \left(\frac{\partial^2}{\partial z^2} - \left(\frac{2\mathbf{p}|\mathbf{k}|}{L} \right)^2 \right) \hat{w}_k + \text{Ri}_b \hat{\Theta}_k + i \frac{2\mathbf{p}|\mathbf{k}|U_{BS}^\square}{L} \hat{w}_k \end{aligned} \quad (2.41)$$

$$\begin{aligned} \frac{\partial \hat{\Theta}_k}{\partial t} + \left(-i \frac{2\mathbf{p}k_x}{L}, -i \frac{2\mathbf{p}k_y}{L}, \frac{\partial}{\partial z} \right) \cdot \hat{\mathbf{u}}_{\Theta_k} + \hat{w}_k \frac{\partial \Theta_d}{\partial z} = \\ \frac{1}{\text{RePr}} \left(\frac{\partial^2}{\partial z^2} - \left(\frac{2\mathbf{p}|\mathbf{k}|}{L} \right)^2 \right) \hat{\Theta}_k + i \frac{2\mathbf{p}|\mathbf{k}|U_{BS}^\square}{L} \hat{\Theta}_k \end{aligned} \quad (2.42)$$

where U_{BS}^\square and U_{BS}^\perp are analogs to \hat{u}_k^\square and \hat{u}_k^\perp , respectively. Note that the pressure is absent from the equation for \hat{u}_k^\perp (eq. 2.40). For the case $\mathbf{k} = \mathbf{0}$, \square and \perp decomposition is not valid but a similar set of equations can be derived for $\hat{u}_{\mathbf{k}=\mathbf{0}}^*$ and $\hat{v}_{\mathbf{k}=\mathbf{0}}^*$ (and $\hat{w}_{\mathbf{k}=\mathbf{0}}$ and $\hat{\Theta}_{\mathbf{k}=\mathbf{0}}$, as well).

Spatial Discretization and Mapping – Vertical Direction

Once the \square and \perp decomposition is finished, the next task is to discretize in the vertical direction. The idea here is to express the vertical variation of the Fourier components of the velocity and temperature in terms of a set of basis functions; for example, we may express \hat{u}_k^\perp in this manner

$$\hat{u}_{\mathbf{k}}^{\perp}(z, t) = \sum_{l=0}^{l=M-1} \mathbf{a}_{\mathbf{k},l}^{\perp}(t) r_{\mathbf{k},l}^{\perp}(z) \quad (2.43)$$

where $\mathbf{a}_{\mathbf{k},l}^{\perp}(t)$ is an expansion coefficient, and $r_{\mathbf{k},l}^{\perp}(z)$ is the basis function. By design $\hat{u}_{\mathbf{k}}^{\perp}$ is not involved in the continuity equation. To ensure continuity we require that the basis functions used to expand $\hat{u}_{\mathbf{k}}^{\square}$ and $\hat{w}_{\mathbf{k}}$ explicitly satisfy the continuity equation

$$-i \frac{2\mathbf{p}|\mathbf{k}|}{L} r_{\mathbf{k},l}^{\square} + \frac{\partial r_{\mathbf{k},l}^{\hat{w}}}{\partial z} = 0 \quad (2.44)$$

where $r_{\mathbf{k},l}^{\square}$ and $r_{\mathbf{k},l}^{\hat{w}}$ are the appropriate basis functions for $\hat{u}_{\mathbf{k}}^{\square}$ and $\hat{w}_{\mathbf{k}}$, respectively. For each l , the basis function $r_{\mathbf{k},l}^{\hat{w}}$ is the same for all $\mathbf{k} \neq 0$. (We shall discuss the case $\mathbf{k} = 0$ below.) In terms of computation, this means we only need to find $r_{\mathbf{k},l}^{\hat{w}}$ once for all l and then store them. We then differentiate these functions and store the differentiated results. To find $r_{\mathbf{k},l}^{\square}$ we just divide these “differentiated functions” by $i2\mathbf{p}|\mathbf{k}|/L$, and there is no need to explicitly calculate and store $r_{\mathbf{k},l}^{\square}$.

An important feature of the vertical discretization is that the vertical domain is semi-infinite, $z \in [0, \infty)$. Very fine resolution is necessary near the wall, both to resolve the viscous sub-layer and the vortical region above, but above the vortical region such fine resolution is not necessary. To provide resolution where it is needed a mapping scheme is designed to map the vertical domain to a finite interval spanned by the variable, $\mathbf{z} \in [a, b]$. Spalart et al. (1991) have advocated an exponential mapping such that $z \rightarrow \mathbf{z}$ using the relationship, $\mathbf{z} = e^{-\frac{z}{z_{map}}}$, where z_{map} is the mapping length scale. As pointed out by Spalart et al. and others (e.g., Boyd, 1982; Metcalfe et al., 1987), exponential mappings lead to an excellent enhancement of resolution in the vortical (i.e., turbulent)

region near the wall but suffer from poor convergence due to Gibbs phenomena¹⁰. Algebraic mappings retain exponential convergence but may not be able to concentrate resolution where it is needed and an even greater drawback is the difficulty of portraying the irrotational part of the flow (which decays in the vertical as e^{-kz} , where k is the wavenumber). The inability to capture this decay exactly slows down the *initial* convergence of spectral methods using an algebraic mapping and to circumnavigate this problem requires the expense of employing more basis functions. Despite this potential difficulty, we use the algebraic mapping

$$z = z_0 \frac{1 + \mathbf{z}}{1 - \mathbf{z}} \quad (2.45)$$

where z_0 is a mapping parameter set equal to 2. With this mapping the vertical coordinate z is mapped the coordinate \mathbf{z} such that a value of $z = 0$ corresponds with $\mathbf{z} = -1$ and $z = \infty$ corresponds with $\mathbf{z} = 1$. Although this mapping provides a little less resolution near the wall than an exponential mapping (given a fixed number of vertical nodes, of course!), a little more resolution is concentrated in the interior of the fluid. This enhancement of interior resolution was sought to provide a means of propagating gravity waves, should these waves arise during the simulations. As demonstrated by Grosch and Orzag (1977), waves directed towards regions of inadequate resolution tend to bounce back from these regions. (In fact, there was little evidence of major gravity wave activity in the simulations but this was not known prior to the simulations). To what extent convergence is delayed by the algebraic mapping is not known, but no convergence problems were evident suggesting that the convergence was adequate.

¹⁰ Spalart et al. (1991) got around the poor convergence by including an extra basis function to resolve the slowing decaying (in z) irrotational component of the flow.

With the mapping described above (eq. 2.45) the equations (2.39 – 2.42) are solved in the mapped coordinate system, $\mathbf{z} \in [-1,1]$. The Fourier components of velocity and temperature are expressed in terms of basis functions that are functions of $\mathbf{z}(z)$. We now find these functions. As pointed out by Coleman et al. (1990a) spectral accuracy may be achieved (for so-called “well-behaved” functions) using a basis set constructed from the singular Sturm-Liouville problem (see, for example, Canuto et al., 1988, page 54). Jacobi polynomials are the only set of polynomials that satisfy the singular Sturm-Liouville problem, and accordingly we form our basis set from the celebrated class of Jacobi polynomials known by the name Legendre. For our particular mapping, such polynomials lead to solution matrices with low bandwidth, thus speeding up the computations.

To represent \hat{w}_k (and therefore \hat{u}_k^\square) we define the functions g that automatically satisfy the boundary conditions on \hat{w}_k ; this is, $\hat{w}_k \rightarrow 0$ as $z \rightarrow \infty$ and at $z = 0$, \hat{w}_k and $\partial\hat{w}_k/\partial z$ must both equal to zero. To obtain the single zero at infinity and the double zero at the surface, we multiply the Legendre polynomial by the factors indicated below

$$g_l(\mathbf{z}) = (1-\mathbf{z})(1+\mathbf{z})^2 P_l(\mathbf{z}) \quad (2.46)$$

where $P_l(\mathbf{z})$ is the l^{th} Legendre polynomial. Clearly $g_l(\mathbf{z})$ has a double zero at $\mathbf{z} = -1$ ($z = 0$) and a single zero at $\mathbf{z} = 1$ ($z = \infty$). These “ g ” functions led to the following expansions for \hat{w}_k and \hat{u}_k^\square

$$\hat{w}_k(z, t) = \sum_{l=0}^{l=M-1} \mathbf{a}_{k,l}^\square(t) g_l(\mathbf{z}(z)) \quad (2.47)$$

and

$$\hat{u}_{\mathbf{k}}^{\square}(z, t) = \sum_{l=0}^{l=M-1} \mathbf{a}_{\mathbf{k},l}^{\square}(t) \frac{1}{i^{\frac{2p|\mathbf{k}|}{L}}} \frac{d}{dz} g_l(\mathbf{z}(z)) \quad (2.48)$$

where $\mathbf{z}(z)$ is the inverse of eq. 2.45, or $\mathbf{z}(z) = (z - z_0)/(z + z_0)$. Note that the same coefficient, $\mathbf{a}_{\mathbf{k},l}^{\square}$, is used in the expansions for $\hat{w}_{\mathbf{k}}$ and $\hat{u}_{\mathbf{k}}^{\square}$. This follows because these two quantities are related through the continuity equation so that if we know one of them, we also know the other. Such expansions may be considered to be “backward transforms” that transform the coefficients \mathbf{a} to Fourier space.

A different set of functions are used to portray $\hat{u}_{\mathbf{k}}^{\perp}$; these functions only require a single zero at both the surface and $z = \infty$. Accordingly, these functions are

$$h_l(\mathbf{z}) = (1 - \mathbf{z})(1 + \mathbf{z})P_l(\mathbf{z}) \quad (2.49)$$

and $\hat{u}_{\mathbf{k}}^{\perp}$ is given by the expansion

$$\hat{u}_{\mathbf{k}}^{\perp}(z, t) = \sum_{l=0}^{l=M-1} \mathbf{a}_{\mathbf{k},l}^{\perp}(t) h_l(\mathbf{z}(z)) \quad (2.50)$$

The expansion for the temperature perturbation requires consideration of the lower boundary condition on this quantity, $\partial\hat{\Theta}_{\mathbf{k}}/\partial z|_{z=0} = 0$. A suitable set of basis functions that satisfy this condition is easily formulated. Consider the functions $e_l(\mathbf{z})$ defined as

$$e_l(\mathbf{z}(z)) = (\mathbf{z} + \mathbf{b}_l)(1 - \mathbf{z})P_l(\mathbf{z}) \quad (2.51)$$

where \mathbf{b}_l is some unknown parameter that depends on l . These functions are automatically congruent with the upper boundary conditions because as $z \rightarrow \infty$ (i.e., $\mathbf{z} \rightarrow 1$) the function is zero. Taking the first derivative with respect to z yields

$$\frac{de_l}{dz} = \frac{de}{dz} \frac{dz}{dz} = \left[(1 - \mathbf{b}_l - 2\mathbf{z})P_l + (\mathbf{z} + \mathbf{b}_l)(1 - \mathbf{z}) \frac{dP_l}{dz} \right] \frac{dz}{dz} \quad (2.52)$$

At $z = 0$ (i.e., $\mathbf{z} = -1$) we require a no-flux boundary condition and this requirement can be met by setting the term in brackets “[]” equal to zero and solving for \mathbf{b}_l . Recalling that $P_l(-1) = (-1)^l$ and that $dP_l/dz|_{z=-1} = -(-1)^l l(l+1)/2$, we can easily solve for \mathbf{b}_l ,

$$\mathbf{b}_l = \frac{l(l+1)+3}{l(l+1)+1} \quad (2.53)$$

With \mathbf{b}_l so defined, the e_l functions meet both the upper and lower boundary conditions, and the expansion for the temperature perturbation is

$$\hat{\Theta}_{\mathbf{k}}(z, t) = \sum_{l=0}^{l=M-1} \mathbf{a}_{\mathbf{k},l}^{\ominus}(t) e_l(\mathbf{z}(z)) \quad (2.54)$$

We now examine the case $\mathbf{k} = 0$. In this case, the decomposition described by eqs. 2.37 is not longer valid, and from the continuity equation we conclude that $\hat{w}_{\mathbf{k}=0} = 0$.¹¹ $\hat{u}_{\mathbf{k}=0}^{\square}$ and $\hat{u}_{\mathbf{k}=0}^{\perp}$ can be taken as the two orthogonal components of the mean perturbation velocity aligned with the positive x and y axis, respectively. Each component has a single zero at $z = 0$, and can therefore be expanded in terms of the “ h_l ” functions (eq. 2.49) described above. The perturbation temperature expansion for $\mathbf{k} = 0$ is identical to eq. 2.54.

Once the vertical expansions for all variables are known, for both $\mathbf{k} = 0$ and $\mathbf{k} \neq 0$, the spatial discretization proceeds in a somewhat roundabout manner motivated by the desire to solve the viscous part of eqs. 2.39 – 2.42 implicitly, thus allowing a larger

¹¹ Finally, the graduate student finds an equation he can solve!

time step. All other terms are solved explicitly. To visualize this process, we again rewrite eqs. 2.39 – 2.42 as

$$\frac{\partial \hat{u}_{\mathbf{k}}^{\square}}{\partial t} = i \frac{2\mathbf{p}}{L} |\mathbf{k}| \hat{p}_{\mathbf{k}} + \frac{1}{\text{Re}} \left(\frac{\partial^2}{\partial z^2} - \left(\frac{2\mathbf{p} |\mathbf{k}|}{L} \right)^2 \right) \hat{u}_{\mathbf{k}}^{\square} + F_{\mathbf{k}}^{\square} \quad (2.55)$$

$$\frac{\partial \hat{u}_{\mathbf{k}}^{\perp}}{\partial t} = \frac{1}{\text{Re}} \left(\frac{\partial^2}{\partial z^2} - \left(\frac{2\mathbf{p} |\mathbf{k}|}{L} \right)^2 \right) \hat{u}_{\mathbf{k}}^{\perp} + F_{\mathbf{k}}^{\perp} \quad (2.56)$$

$$\frac{\partial \hat{w}_{\mathbf{k}}}{\partial t} = -\frac{\partial \hat{p}_{\mathbf{k}}}{\partial z} + \frac{1}{\text{Re}} \left(\frac{\partial^2}{\partial z^2} - \left(\frac{2\mathbf{p} |\mathbf{k}|}{L} \right)^2 \right) \hat{w}_{\mathbf{k}} + F_{\mathbf{k}}^w \quad (2.57)$$

$$\frac{\partial \hat{\Theta}_{\mathbf{k}}}{\partial t} = \frac{1}{\text{Re Pr}} \left(\frac{\partial^2}{\partial z^2} - \left(\frac{2\mathbf{p} |\mathbf{k}|}{L} \right)^2 \right) \hat{\Theta}_{\mathbf{k}} + F_{\mathbf{k}}^{\Theta} \quad (2.58)$$

The vector $\mathbf{F}_{\mathbf{k}} = (F_{\mathbf{k}}^{\square}, F_{\mathbf{k}}^{\perp}, F_{\mathbf{k}}^w, F_{\mathbf{k}}^{\Theta})$ is a so-called forcing term, consisting of the following linear and non-linear components

$$F_{\mathbf{k}}^{\square} = \frac{1}{\text{Ro}} \hat{u}_{\mathbf{k}}^{\perp} + \left(i \frac{2\mathbf{p} |\mathbf{k}| U_{BS}^{\square}}{L} \hat{u}_{\mathbf{k}}^{\square} - \hat{w}_{\mathbf{k}} \frac{dU_{BS}^{\square}}{dz} \right) - \frac{k_x \overline{NL}_{\mathbf{k}}^x + k_y \overline{NL}_{\mathbf{k}}^y}{|\mathbf{k}|} \quad (2.59)$$

$$F_{\mathbf{k}}^{\perp} = -\frac{1}{\text{Ro}} \hat{u}_{\mathbf{k}}^{\square} + \left(i \frac{2\mathbf{p} |\mathbf{k}| U_{BS}^{\perp}}{L} \hat{u}_{\mathbf{k}}^{\perp} - \hat{w}_{\mathbf{k}} \frac{dU_{BS}^{\perp}}{dz} \right) - \frac{k_x \overline{NL}_{\mathbf{k}}^y - k_y \overline{NL}_{\mathbf{k}}^x}{|\mathbf{k}|} \quad (2.60)$$

$$F_{\mathbf{k}}^w = \text{Ri}_b \hat{\Theta}_{\mathbf{k}} + i \frac{2\mathbf{p} |\mathbf{k}| U_{BS}^{\square}}{L} \hat{w}_{\mathbf{k}} - \overline{NL}_{\mathbf{k}}^z \quad (2.61)$$

$$F_{\mathbf{k}}^{\Theta} = i \frac{2\mathbf{p}|\mathbf{k}|U_{BS}^{\square}}{L} \hat{\Theta}_{\mathbf{k}} - \left(-i \frac{2\mathbf{p}k_x}{L}, -i \frac{2\mathbf{p}k_y}{L}, \frac{\partial}{\partial z} \right) \cdot \mathbf{u}_{\Theta_{\mathbf{k}}} - \hat{w}_{\mathbf{k}} \frac{\partial \Theta_d}{\partial z} \quad (2.62)$$

Given the coefficients, $\mathbf{a} = (\mathbf{a}_{\mathbf{k}}^{\square}, \mathbf{a}_{\mathbf{k}}^{\perp}, \mathbf{a}_{\mathbf{k}}^{\Theta})$, one can find the linear components of the vector $\mathbf{F}_{\mathbf{k}}$ using the backward transformations (i.e., $\mathbf{a}_{\mathbf{k}}^{\square, \perp, \Theta} \rightarrow \hat{u}_{\mathbf{k}}^{\square}, \hat{w}_{\mathbf{k}}, \hat{u}_{\mathbf{k}}^{\perp}, \hat{\Theta}_{\mathbf{k}}$) embodied in eqs. 2.47, 2.48, 2.50 and 2.54.

Evaluation of the non-linear components is done in a manner that avoids aliasing (as opposed to a so-called pseudo-spectral method in which aliasing errors are permitted; see Canuto et al. [1988], page 83). For example, let us examine the non-linear term $NL_{\mathbf{k}}^x$ that is present in eqs. 2.59 and 2.60. In expanded form, this term is

$$\left(\overline{\mathbf{w}} \times \mathbf{u} \right)_{\mathbf{k}}^x = \overline{\mathbf{w}}^y w_{\mathbf{k}}^z - \overline{\mathbf{w}}^z w_{\mathbf{k}}^y \quad (2.63)$$

where \mathbf{w}^y and \mathbf{w}^z are the components of the vorticity vector in the y and z directions, respectively. The evaluation of this term begins by the backward transforms described above from which $\hat{u}_{\mathbf{k}}^{\square}, \hat{w}_{\mathbf{k}}, \hat{u}_{\mathbf{k}}^{\perp}$ are found. Using the inverse of eqs. 2.37, $\hat{u}_{\mathbf{k}}$ and $\hat{v}_{\mathbf{k}}$ are trivially determined. A Fast Fourier Transform (FFT) takes all three components of the velocity vector to real space. A similar process may be used to find the three components of the vorticity vector. To calculate the non-linear term of interest here, the appropriate components of the vorticity vector and the velocity vector are multiplied together (eq. 2.63), and the FFT then transforms the products back to Fourier space. The method of padding, also known as the 3/2 rule, (Canuto et al., 1988, pg. 84) is invoked to eliminate aliasing errors.

Once the vector \mathbf{F} is determined, the governing equations 2.55- 2.58 may be written in so-called semi-discrete form, in which the three spatial dimensions have been fully discretized leaving only time derivatives. Taking, for example, eqs. 2.55 and 2.57 that

compose the two non-zero components of the U^+ vector mode, the path to the semi-discrete form begins by substituting the series expansions for \hat{u}_k^\square (eq. 2.48) and \hat{w}_k (eq. 2.47) into eqs. 2.55 and 2.57 to yield

$$\begin{aligned} & \sum_{l=0}^{l=M-1} \frac{d\mathbf{a}_{k,l}^\square}{dt} \frac{1}{i \frac{2\mathbf{p}|\mathbf{k}|}{L}} \frac{d}{dz} g_l(\mathbf{z}(z)) = \\ & i \frac{2\mathbf{p}}{L} |\mathbf{k}| \hat{p}_k \tag{2.64} \\ & + \frac{1}{\text{Re}} \sum_{l=0}^{l=M-1} \mathbf{a}_{k,l}^\square \left(\frac{1}{i \frac{2\mathbf{p}|\mathbf{k}|}{L}} \frac{d^3}{dz^3} g_l(\mathbf{z}(z)) - \left(\frac{2\mathbf{p}|\mathbf{k}|}{L} \right)^2 \frac{1}{i \frac{2\mathbf{p}|\mathbf{k}|}{L}} \frac{d}{dz} g_l(\mathbf{z}(z)) \right) + F_k^\square \end{aligned}$$

$$\begin{aligned} & \sum_{l=0}^{l=M-1} \frac{d\mathbf{a}_{k,l}^\square}{dt} g_l(\mathbf{z}(z)) = -\frac{\partial \hat{p}_k^*}{\partial z} \tag{2.65} \\ & + \frac{1}{\text{Re}} \sum_{l=0}^{l=M-1} \mathbf{a}_{k,l}^\square \left(\frac{d^2}{dz^2} g_l(\mathbf{z}(z)) - \left(\frac{2\mathbf{p}|\mathbf{k}|}{L} \right)^2 g_l(\mathbf{z}(z)) \right) + F_k^w \end{aligned}$$

Using the Galerkin weighted residual method, we multiply this “vector” of two equations by the vector test functions, $s_{m,\mathbf{k}}^+$,

$$s_{m,\mathbf{k}}^+ = \begin{pmatrix} -\frac{1}{i \frac{2\mathbf{p}|\mathbf{k}|}{L}} \frac{d}{dz} g_m \\ g_m \end{pmatrix} \tag{2.66}$$

and integrate over the vertical dimension $\int_0^\infty (\) dz$ (applied using the 3/2 rule to avoid aliasing errors) to obtain semi-discrete equations of the form

$$\mathbf{A}_k^\square \frac{d\mathbf{a}_k^\square}{dt} = \mathbf{B}_k^\square \mathbf{a}_k^\square + \mathbf{T}_k^\square \tag{2.67}$$

where for each \mathbf{k} , $\mathbf{a}_{\mathbf{k}}$ is a vector with components $(\mathbf{a}_0, \dots, \mathbf{a}_{m-1})$, and $\mathbf{A}_{\mathbf{k}}^{\parallel}$ and $\mathbf{B}_{\mathbf{k}}^{\parallel}$ are square $M \times M$ matrices are matrices with the following elements (for $\mathbf{k} \neq 0$)

$$A_{l,m,\mathbf{k}}^{\square} = \int_0^{\infty} \left(g_l g_m + \frac{1}{\left(\frac{2\mathbf{p}|\mathbf{k}|}{L} \right)^2} \frac{dg_l}{dz} \frac{dg_m}{dz} \right) dz \quad (2.68)$$

$$B_{l,m,\mathbf{k}}^{\square} = -\frac{1}{\text{Re}} \int_0^{\infty} \left(\frac{1}{\left(\frac{2\mathbf{p}|\mathbf{k}|}{L} \right)^2} \frac{d^2 g_l}{dz^2} \frac{d^2 g_m}{dz^2} + 2 \frac{dg_l}{dz} \frac{dg_m}{dz} + \left(\frac{2\mathbf{p}|\mathbf{k}|}{L} \right)^2 g_l g_m \right) dz \quad (2.69)$$

and $\mathbf{T}_{\mathbf{k}}^{\parallel}$ is a vector of length M , with elements

$$T_{l,\mathbf{k}}^{\square} = \int_0^{\infty} \left(-F_{\mathbf{k}}^{\square} \frac{1}{i \frac{2\mathbf{p}|\mathbf{k}|}{L}} \frac{dg_l}{dz} + F_{\mathbf{k}}^w g_l \right) dz \quad (2.70)$$

The pressure terms in the U^+ equation set conveniently integrate to zero, thus demonstrating the advantage of using the non-divergent basis functions. The matrix $\mathbf{A}_{\mathbf{k}}^{\parallel}$ is somewhat sparse with a bandwidth of 13 while the matrix $\mathbf{B}_{\mathbf{k}}^{\parallel}$ is symmetric and negative definite. This property of $\mathbf{B}_{\mathbf{k}}^{\parallel}$ is a manifestation of the role of molecular viscosity, which only dissipates energy. Energy only enters into this system of equations through the “forcing” term $\mathbf{T}_{\mathbf{k}}^{\parallel}$.

In a similar manner as described above, semi-discrete equations can be derived for the U^- mode and the energy equations. The semi-discrete equation for the U^- mode takes a form analogous to eq. 2.67,

$$\mathbf{A}_{\mathbf{k}}^{\perp} \frac{d\mathbf{a}_{\mathbf{k}}^{\perp}}{dt} = \mathbf{B}_{\mathbf{k}}^{\perp} \mathbf{a}_{\mathbf{k}}^{\perp} + \mathbf{T}_{\mathbf{k}}^{\perp} \quad (2.71)$$

This equation is obtained by substituting the expansion for $\hat{u}_{\mathbf{k}}^{\perp}$, eq. 2.50, into the equation for $\hat{u}_{\mathbf{k}}^{\perp}$, eq. 2.56, multiplying by the “-” mode test functions, $s_{m,\mathbf{k}}^-$,

$$s_{m,\mathbf{k}}^- = h_m \quad (2.72)$$

and then integrating over the vertical coordinate as above. The matrix \mathbf{A}^{\perp} has the components

$$A_{l,m}^{\perp} = \int_0^{\infty} h_l h_m dz \quad (2.73)$$

and this matrix is pentadiagonal and does not depend on the wavenumber \mathbf{k} . The components of $\mathbf{B}^{\perp}_{\mathbf{k}}$ and $\mathbf{T}^{\perp}_{\mathbf{k}}$ are, respectively,

$$B_{l,m,\mathbf{k}}^{\perp} = -\frac{1}{\text{Re}} \int_0^{\infty} \left(\frac{dh_l}{dz} \frac{dh_m}{dz} + \left(\frac{2\mathbf{p}|\mathbf{k}|}{L} \right)^2 h_l h_m \right) dz \quad (2.74)$$

and

$$T_{l,\mathbf{k}}^{\perp} = \int_0^{\infty} (F_{\mathbf{k}}^{\perp} h_l) dz \quad (2.75)$$

Again, $\mathbf{B}^{\perp}_{\mathbf{k}}$ is negative definite.

Finally, the semi-discrete form of the energy equation, eq. 2.58, is found in an analogous way to the semi-discrete equations described above. We again substitute the expansion for $\hat{\Theta}_{\mathbf{k}}$ (eq. 2.54) into the energy equation, multiply by the test function, e_l , and integrate over the vertical coordinate. This procedure results in the semi-discrete equation

$$\mathbf{A}^\ominus \frac{d\mathbf{a}_k^\ominus}{dt} = \mathbf{B}_k^\ominus \mathbf{a}_k^\ominus + \mathbf{T}_k^\ominus \quad (2.76)$$

The pentadiagonal matrix \mathbf{A}^\ominus has elements

$$A_{l,m}^\ominus = \int_0^\infty (e_l e_m) dz \quad (2.77)$$

and the elements of \mathbf{B}_k^\ominus (negative definite) and \mathbf{T}_k^\ominus are, respectively,

$$B_{l,m,k}^\ominus = -\frac{1}{\text{RePr}} \int_0^\infty \left(\frac{de_l}{dz} \frac{de_m}{dz} + \left(\frac{2\mathbf{p}|\mathbf{k}|}{L} \right)^2 e_l e_m \right) dz \quad (2.78)$$

and

$$T_{l,k}^\ominus = \int_0^\infty (F_k^\ominus e_l) dz \quad (2.79)$$

We must also consider the case $\mathbf{k} = 0$. For this case, all derivatives in the x - and y -directions are zero and the mean vertical velocity, $\hat{w}_{\mathbf{k}=0}$, is also zero. The parallel-perpendicular decomposition described above (eq. 2.37) is, of course, no longer applicable, and we make take $\hat{u}_{\mathbf{k}=0}^\square$ as being aligned along the positive x -axis and $\hat{u}_{\mathbf{k}=0}^\perp$ as being aligned along the positive y -axis. The governing equations are then

$$\frac{\partial \hat{u}_{\mathbf{k}=0}^\square}{\partial t} = \frac{1}{\text{Re}} \frac{d^2 \hat{u}_{\mathbf{k}=0}^\square}{dz^2} + F_{\mathbf{k}=0}^\square \quad (2.80)$$

$$\frac{\partial \hat{u}_{\mathbf{k}=0}^\perp}{\partial t} = \frac{1}{\text{Re}} \frac{d^2 \hat{u}_{\mathbf{k}=0}^\perp}{dz^2} + F_{\mathbf{k}=0}^\perp \quad (2.81)$$

$$\hat{w}_{\mathbf{k}=0} = 0 \quad (2.82)$$

$$\frac{\partial \hat{\Theta}_{\mathbf{k}=0}}{\partial t} = \frac{1}{\text{RePr}} \frac{d^2 \hat{\Theta}_{\mathbf{k}=0}}{dz^2} + F_{\mathbf{k}=0}^{\Theta} \quad (2.83)$$

and the components of $\mathbf{F}_{\mathbf{k}=0}$ are given by

$$F_{\mathbf{k}=0}^{\square} = \frac{1}{\text{Ro}} \hat{u}_{\mathbf{k}=0}^{\perp} - \left(\overline{\mathbf{w}} \times \mathbf{u} \right)_{\mathbf{k}=0}^x \quad (2.84)$$

$$F_{\mathbf{k}=0}^{\perp} = -\frac{1}{\text{Ro}} \hat{u}_{\mathbf{k}=0}^{\square} - \left(\overline{\mathbf{w}} \times \mathbf{u} \right)_{\mathbf{k}=0}^y \quad (2.85)$$

$$F_{\mathbf{k}=0}^{\Theta} = -\frac{d}{dz} \overline{w} \Theta_{\mathbf{k}=0} \quad (2.86)$$

For $\mathbf{k} = 0$, the velocity components trivially satisfy the continuity equation, and the lower boundary condition is satisfied by a function with single zero at $z = 0$; therefore, we can expand these components in terms of the “ h ” functions defined in eq. 2.49. The semi-discrete equations for the $\hat{u}_{\mathbf{k}=0}^{\perp}$ and $\hat{\Theta}_{\mathbf{k}=0}$ are identical to those given above (eqs. 2.71 and 2.76) and the elements of the “**A**” (eqs. 2.73 and 2.77) and “**B**” (eqs. 2.74 and 2.78) matrices are the same, with \mathbf{k} set equal to zero. The vectors $\mathbf{T}_{\mathbf{k}=0}^{\perp}$ and $\mathbf{T}_{\mathbf{k}=0}^{\Theta}$ are formed using eqs. 2.85 and 2.86, respectively, multiplying these equations by the test function, h_l , and integrating over the vertical coordinate. The semi-discrete equation for $\hat{u}_{\mathbf{k}=0}^{\square}$ is identical to eq. 2.67, but with the $\mathbf{A}_{\mathbf{k}=0}^{\square} = \mathbf{A}_{\mathbf{k}=0}^{\perp}$ and $\mathbf{B}_{\mathbf{k}=0}^{\square} = \mathbf{B}_{\mathbf{k}=0}^{\perp}$, with the elements of $\mathbf{T}_{\mathbf{k}=0}^{\square}$ given by $\int_0^{\infty} F_{\mathbf{k}=0}^{\square} h_l dz$.

When finding $\mathbf{T}_{\mathbf{k}}^{\Theta}$ it is useful to use an integration by parts to simplify the computation of this vector. Explicitly, the expression for elements of $\mathbf{T}_{\mathbf{k}}^{\Theta}$ is

$$T_{l,k}^{\ominus} = \int_0^{\infty} \left(i \frac{2\mathbf{p}|\mathbf{k}|U_{BS}^{\square}}{L} \hat{\Theta}_k + i \frac{2\mathbf{p}k_x}{L} \overline{u}\Theta_k + i \frac{2\mathbf{p}k_y}{L} \overline{v}\Theta_k - \frac{\partial}{\partial z} \overline{w}\Theta_k - \hat{w}_k \frac{\partial \Theta_d}{\partial z} \right) e_l dz \quad (2.87)$$

In this integral, it is convenient to integrate the term $\int_0^{\infty} \left(\frac{\partial}{\partial z} \overline{w}\Theta_k \right) e_l dz$ by parts yielding

$$-\int_0^{\infty} (\overline{w}\Theta_k) \frac{d}{dz} e_l dz .$$

With this trick, we avoid the computation of the vertical derivative of $\overline{w}\Theta_k$ and instead use the derivative of e_l -- a derivative that is easily calculated and used in other parts of this numerical algorithm.

Time Advancement Scheme

The mixed implicit-explicit time advancement scheme employed here is identical to that described in Coleman et al. (1990b). (This scheme is attributed to unpublished work by Wray.) The time advancement algorithm begins with the semi-discrete equations for \hat{u}_k^{\square} , \hat{u}_k^{\perp} , and $\hat{\Theta}_k^{\square}$ (eqs. 2.67, 2.71, and 2.76, respectively). The viscous part of the flow has been isolated in the semi-discrete equations and is embodied in the **B** matrices and the time advancement associated with these terms is solved implicitly using the second-order accurate Crank-Nicolson method. Time advancement for the linear and non-linear forcing, contained in the **T** vectors, is done explicitly using a third-order accurate Runge-Kutta scheme. This mixed formulation is motivated in part by the need to have as large a time step as possible while still preserving numerical accuracy. Solving the viscous terms implicitly avoids the onerous requirement of a very small time step that comes with an explicit method.

In the method employed here, each full time step, Dt , is divided into three unequal

substeps, Dt_s , such that $\Delta t = \sum_{s=1}^{s=3} \Delta t_s$. For all three semi-implicit equations, the

algorithm that advances the solution, \mathbf{a} , over one full time step ($\mathbf{D} t$) from \mathbf{a}^n to \mathbf{a}^{n+3} , takes the form

$$\left(\mathbf{A} - \frac{\Delta t_s}{2} \mathbf{B}\right) \mathbf{a}^{n+s} = \left(\mathbf{A} + \frac{\Delta t_s}{2} \mathbf{B}\right) \mathbf{a}^{n-1+s} + \Delta t_s \mathbf{c}_s \mathbf{T}^{n-1+s} + \Delta t_s \mathbf{y}_s \mathbf{T}^{n-2+s} \quad (2.88)$$

where the index “ s ” varies from 1 to 3, \mathbf{A} is the “ \mathbf{A} ” matrix associated with the semi-implicit equations, and \mathbf{c}_s and \mathbf{y}_s are coefficients listed in Table 3 below.

Table 3: Coefficients for time advancement scheme

s	\mathbf{y}_s	\mathbf{c}_s	$\frac{\Delta t_s}{\Delta t}$
1	0	1	8/15
2	-17/8	25/8	2/15
3	-5/4	9/4	1/3

(In eq. 2.88 confusion can be avoided by realizing that advancement over a full time step requires three substeps and the time indices “ n ” are locked to these substeps. Thus over a full time step, Δt , n will range from n to $n+3$ and $\Delta t = t^{n+3} - t^n$, where t^n and t^{n+3} are the times at the beginning and end of the time step, respectively).

As shown by Coleman et al. (1990b), the maximum (full) time step may be estimated by the following equation

$$(\Delta t)_{\max} = \frac{\sqrt{3}}{3 \left(\frac{|u|_{\max}}{\Delta x} + \frac{|v|_{\max}}{\Delta y} + \frac{|w|_{\max}}{\Delta z} \right)} \quad (2.89)$$

In practice, this estimate was found to work quite well. A larger time step was permitted by a Galilean transformation of the u and v components of the velocity such that the u component was reduced by a factor of $1/2$ and the v component was reduced by about 15%.

Summary of Numerical Algorithm

Given the expansion coefficients $(\mathbf{a}_k^{\square})^n$, $(\mathbf{a}_k^{\perp})^n$, and $(\mathbf{a}_k^{\ominus})^n$ at the time t^n , the full numerical algorithm updates these coefficients to the next time t^{n+3} in the following manner:

- 1) The coefficients $(\mathbf{a}_k^{\square})^n$, $(\mathbf{a}_k^{\perp})^n$, and $(\mathbf{a}_k^{\ominus})^n$ are transformed to the quantities \hat{u}_k^{\square} , \hat{w}_k , \hat{u}_k^{\perp} , and $\hat{\Theta}_k$, using the expansions described above (eqs. 2.48, 2.47, 2.50 and 2.54, respectively).
- 2) Spatial derivatives ($\partial/\partial x$, $\partial/\partial y$, $\partial/\partial z$) of the Fourier transformed velocity components are found. Derivatives with respect to either horizontal direction are calculated trivially in the customary manner: $\partial \hat{w}_k / \partial x = -i2\mathbf{p}k_x / L \cdot \hat{w}_k$, etc. For derivatives with respect to z , this calculation requires a slight modification of the expansions (eqs. 2.47, 2.48, and 2.50). For example, to find $\partial \hat{w}_k / \partial z$ eq. 2.47 is changed to

$$\frac{\partial \hat{w}_k(z, t)}{\partial z} = \sum_{l=0}^{l=M-1} \mathbf{a}_{k,l}^{\square}(t) \frac{d}{dz} g_l(\mathbf{z}(z)) \quad (2.90)$$

- 3) Once the Fourier transform of the derivatives is found, an inverse Fourier transform (using an FFT, of course) takes Fourier transforms of derivatives and the Fourier transforms of the velocity components and temperature perturbation to real space. The real space variables (u, v, w, Θ) and the derivatives of these variables are used to find the vorticity vector, \mathbf{w} , from which the non-linear term $\mathbf{w} \times \mathbf{u}$ is calculated. The heat flux, $\mathbf{u}\Theta$, is trivially calculated. For these calculations the 3/2 rule is invoked to prevent aliasing errors.
- 4) Linear components of the vector \mathbf{F}_k (eqs. 2.59-2.62) are calculated from the Fourier transformed velocity and temperature components. (The linear components are terms such as $\frac{1}{\text{Ro}} \hat{u}_k^\perp + \left(i \frac{2\mathbf{p} \cdot \mathbf{k} |U_{BS}^\square}{L} \hat{u}_k^\square - \hat{w}_k \frac{dU_{BS}^\square}{dz} \right)$.)
- 5) The Fourier transforms of the non-linear terms ($\mathbf{w} \times \mathbf{u}$, $\mathbf{u}\Theta$) are found and added to the corresponding linear terms. This completes the construction of the vectors, \mathbf{F}_k .
- 6) The vector \mathbf{F}_k is transformed to the vectors \mathbf{T}_k^\parallel , \mathbf{T}_k^\perp , and \mathbf{T}_k^Θ using a so-called forward transformations given by eqs. 2.70, 2.75, and 2.79 for $\mathbf{k} \neq 0$, and analogous expressions for the case $\mathbf{k} = 0$.
- 7) The \mathbf{A} and \mathbf{B} matrices of the semi-discrete equations are calculated. The building block of these matrices (terms such as $\int_0^\infty g_l g_m dz$) can be calculated once and for all and then stored saving considerable computational cost at each time step.
- 8) Time advancement takes place using eq. 2.88 and the new coefficients $(\mathbf{a}_k^\square)^{n+3}$, $(\mathbf{a}_k^\perp)^{n+3}$, and $(\mathbf{a}_k^\Theta)^{n+3}$ are determined.
- 9) We go back to step (1) and repeat the process.

2.3.3 ASSESSING MODEL PERFORMANCE

Does the model described above performed as advertised? We now examine this question. The primary means of evaluating the model is to compare our results with the neutrally stratified results of Coleman et al. (1990a). Our supposition is that the two approaches are similar -- essentially differing only in the vertical mapping -- and therefore simulations from both models should be similar. If this is the case, it is likely that both models are indeed working in accordance with the stated goal providing an accurate solution to the Navier-Stokes equations at low Re .

Of course, the examination of neutrally stratified flow cannot tell us whether the parts of the model associated with stratification are working. Moreover, a direct comparison with the stably stratified simulations of Coleman et al. (1994) is problematic because of the differing lower boundary condition on temperature between his model and the model presented here. Another way of examining the linear aspects of the “stratified part” of the model is through a linear stability analysis, wherein the model can be started from a quiescent state seeded with a low level of noise, and the initial behavior observed. Presumably the early stages of flow will be linear because of the small amplitudes involved, and the modeled flow can be compared with the results of a linear stability analysis to assess whether the model is performing correctly.

Neutral Stratification

Table 4 lists the parameters that describe the mesh structure of our neutrally stratified DNS with a Reynolds number of 400 and $Ri_b = 0$. For the sake of comparison, this table also lists the corresponding parameters for Coleman et al. (1990a) run with $Re = 400$, and Coleman’s (1999) simulation with $Re = 1000$. In this table, N_x and N_y are the number of grid points in the x - and y -directions, and N_z is the number of quadrature points in the vertical direction, with $N_z > 3/2 M$, where M is the number of basis functions used in the vertical discretization. With $N_z > 3/2 M$ aliasing errors are

eliminated through the 3/2-rule. This rule is also applied in the horizontal direction, and therefore, for our model, the “effective” wavenumbers k_x and k_y extend from -15 to 16 , for a total “bandwidth” of 16 in each horizontal direction. In these directions our model’s length (L_x, L_y) is 26 nondimensional length units. The first quadrature point in the vertical, z_0 , is at the surface, $z = 0$, while the point immediately above the surface, z_1 , is equal to 2.43×10^{-3} . The height above the surface of the maximum quadrature point, z_{max} , is 4182 .

Table 4: Numerical parameters for neutrally stratified model runs.

	N_x	N_y	N_z	L_x, L_y	z_1	z_{max}
this study, Re = 400	48	48	55	26	2.43×10^{-3}	4182
Coleman et al. (1990a), Re = 400, Case A90	96	96	45	≈ 26	7.67×10^{-3}	≈ 23.5
Coleman (1999), Re = 1000	384	384	85	≈ 18	unknown	unknown

When compared with DNS runs performed on the latest supercomputers (e.g., for Coleman’s [1999] run with Re = 1000, $N_x = N_y = 384$), the numerical resolution of our model seems admittedly unimpressive. However, as will be discussed below, the results do not seem to suffer greatly from this very modest resolution. It is important to note that the vertical resolution of our model is somewhat greater than Coleman et al.’s (1990a) Re = 400 run and that this enhanced resolution extends further from the lower boundary -- a consequence of the algebraic mapping. This augmented resolution was designed to better capture gravity wave activity should it occur.

The model was initialized with a low level of noise in the form of random Gaussian deviates. Figure 6 shows the time evolution of the friction velocity, u_* / G , as well as the angle, β , that the surface stress vector makes with the geostrophic wind. These quantities have been plotted versus the time, nondimensionalized by $1/f$. (The time

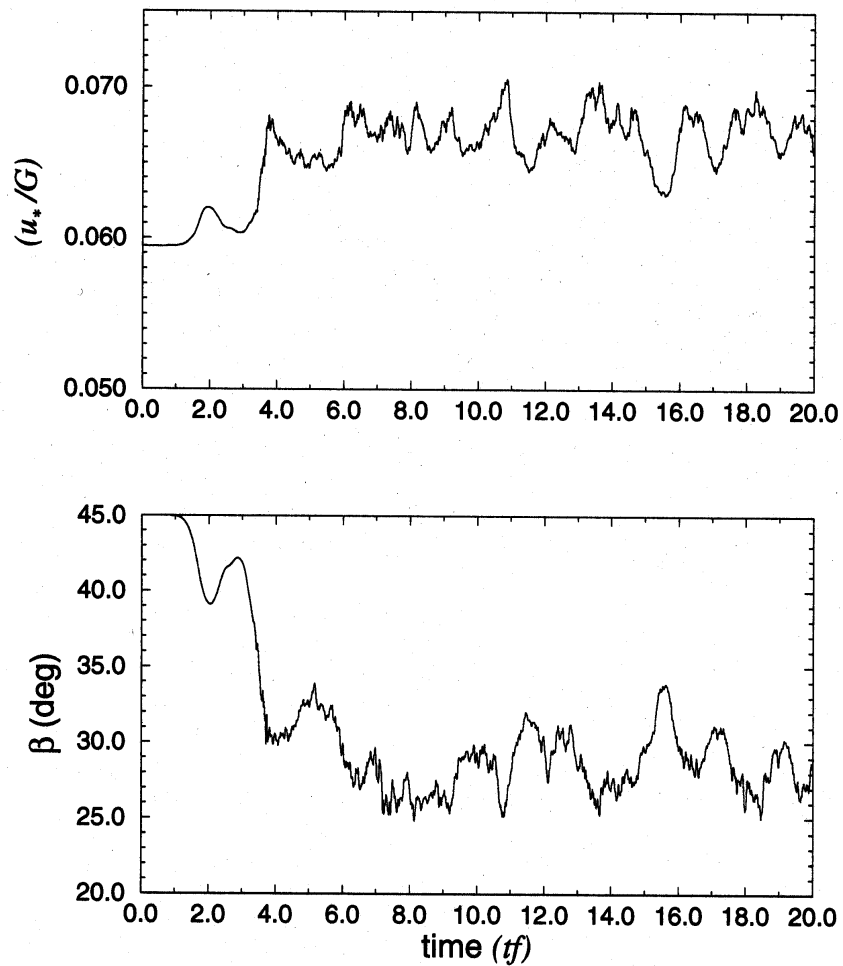


Figure 6: Time series of the friction velocity, u_* / G (top panel), and the angle, β , that the

surface stress vector makes with the geostrophic wind (bottom panel).

scale $1/f$, as opposed to the scale D/G , seems the most sensible scale for examining these results). The span of time for this run, $tf = 20$, requires about 3 days of CPU time on a Sun Ultra 30 workstation. (“ tf ” is the time nondimensionalized by f .) After a time of about $tf = 1/2$ roll cells begin to develop in the flow; these cells are a manifestation of the “inflectional instability” (Lilly, 1966; Brown, 1972) of the laminar Ekman layer. The growth rate of these cells has an e-folding time of about $1/4$ and, after about four time units, the cells begin to break down into turbulence.

The turbulence appears to become in equilibrium (overall production = overall dissipation) with the main flow at about eight time units, because after this time, the quantities u_* / G and \mathbf{b} appear to become stationary, and exhibit fluctuations about steady mean values. These fluctuations are statistical in nature and stem from averaging over a horizontal plane of finite size. In principle, the fluctuations would be reduced or eliminated if the horizontal domain over which the averages are found is infinite in extent; see Coleman et al. (1990a).

An estimate of the mean values of the friction velocity and the stress angle, \mathbf{b} , can be calculated by averaging the time series of these quantities from about $tf = 7.5$ to $tf = 20$. (This encompasses a span of about two inertial periods, where one inertial period has a length of $tf = 2\pi$.) The mean values are listed in Table 5 along with the corresponding

Table 5: Values of the friction velocity, u_* / G , and the stress angle, \mathbf{b} , for various model runs.

u_* / G	\mathbf{b}
-----------	--------------

this study, Re = 400	0.0672	28.4
Coleman et al., (1990a), Re = 400. Run A90	0.0652	28.5
Coleman (1999), Re = 1000	0.0539	19.0

mean values from Coleman et al.'s (1990a) simulation with Re = 400 run, and for the sake of comparison, we have included Coleman's (1999) Re = 1000 run. These "global" results (i.e., averaged results that reflect the state of the entire flow) show fairly good agreement between the model described here and that of Coleman et al. This comparison is certainly useful, but whether it can be used as an indicator of adequate resolution is hard to determine.

A more detailed comparison of the turbulent processes can be obtained by examining vertical profiles of the Reynolds stress from Coleman et al. (1990a) and our work. This comparison is shown in Figure 7 in which the upper panel shows the off-diagonal components of the Reynolds stress tensor from our model (depicted by $\langle uw \rangle$, $\langle uv \rangle$, and $\langle vw \rangle$) while the lower panel shows the same quantities derived from Coleman et al. In both panels, the vertical coordinate is $z/f/u_*$ but it is expressed in the lower panel as z/d where d is this is scale height of the turbulent Ekman layer equal to u_*^2/f (Tennekes and Lumley, 1989). These Reynolds stresses have been time-averaged over a span of at least one inertial period for the results of Coleman et al., and for our model somewhat less than one period. The correspondence between the $\langle uw \rangle$ and $\langle vw \rangle$ is almost exact but there is small but significant difference between the $\langle uv \rangle$ profiles. It is difficult (if not impossible) to track down the cause of this difference. We can only speculate that the lack of complete agreement in the $\langle uv \rangle$ profile could be attributed to differences in either horizontal or vertical resolution. Our horizontal

resolution is one-half that of Coleman et al.'s yet our vertical resolution is greater. It is possible that the enhanced vertical resolution of our model allows it to pick up features that may be missed in the other model. (Of course, this argument could be applied in the reverse direction: the greater horizontal resolution of Coleman et al.'s model may make it the better simulation.) It is also possible, but unlikely, that had we been able to average our profiles over a longer time period, the differences in the $\langle uv \rangle$ profiles would have

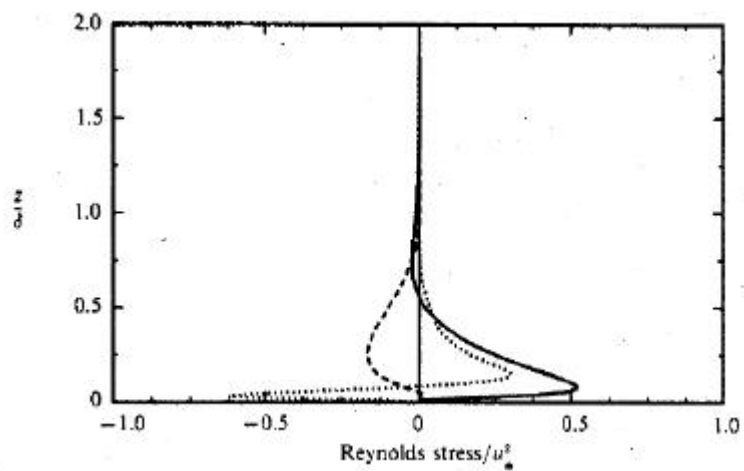
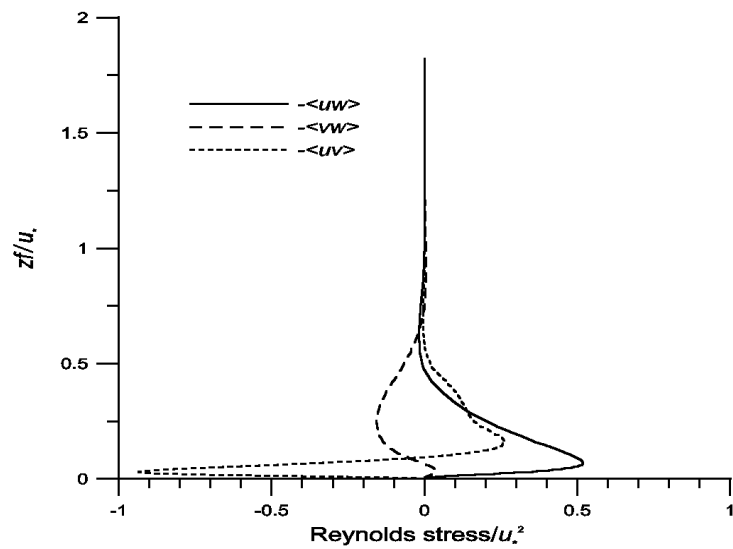


Figure 7: Three components of the Reynolds stress; $-\langle uw \rangle$ is solid line —; $-\langle vw \rangle$ is dashed line -----, $-\langle uv \rangle$ is dotted line ·····; x -axis is aligned with geostrophic wind. The top panel depicts Reynolds stress from this study while the bottom panel is from Coleman et al. (1990b)

disappeared. Despite this difference, the agreement between the stress profiles from the two models is quite good.

A one-dimensional spectrum of w (from our model at a height of $z/D = 0.85$), averaged over time and space, is shown in Figure 8. The spectrum is smooth and if a resolution problem were active, it would show up as “pile up” of energy at the high wavenumbers. Such an upturn is not seen. Upturns in spectra constructed for other heights have never been seen; taken together, these spectra suggest that the resolution is adequate.

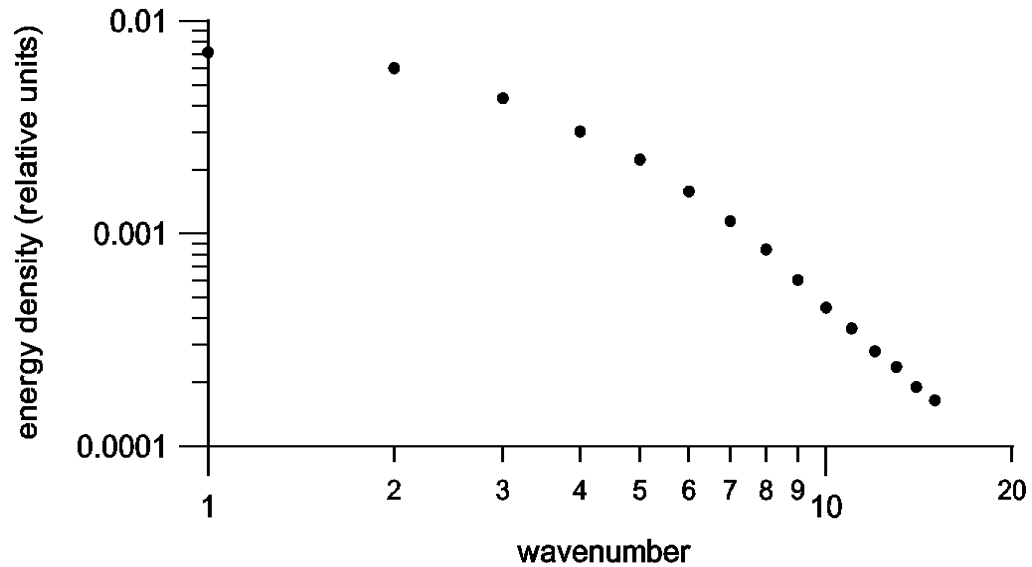


Figure 8: One-dimensional energy spectrum for the vertical velocity, w . The spectrum is taken in a direction parallel to the x -axis.

Before leaving the neutral case we show in passing an example of what could be boundary layer streaks. We will not explore the issue of streaks further here. We merely want to show a plot (Figure 9) that suggests the existence of boundary layer streaks in our DNS. This figure shows a shaded contour plot of the instantaneous vertical velocity, w , taken at a height of $z/D = 0.03$. The elongation and orientation of the contours suggest thin coherent structures with longitudinal axis oriented at angles from about 10 to 30 degrees to the x -axis (the direction of the geostrophic wind). These structures are confined to the lower boundary layer and are not seen elsewhere, and they are consistent with the concept of a boundary layer streak (Drobinski and Foster, 2000; Foster, 1997). The LES simulation depicted in Figure 1 of Moeng and Sullivan (1994) shows “streaky structures” similar to those seen in Figure 9 below.

(Intentionally left blank)

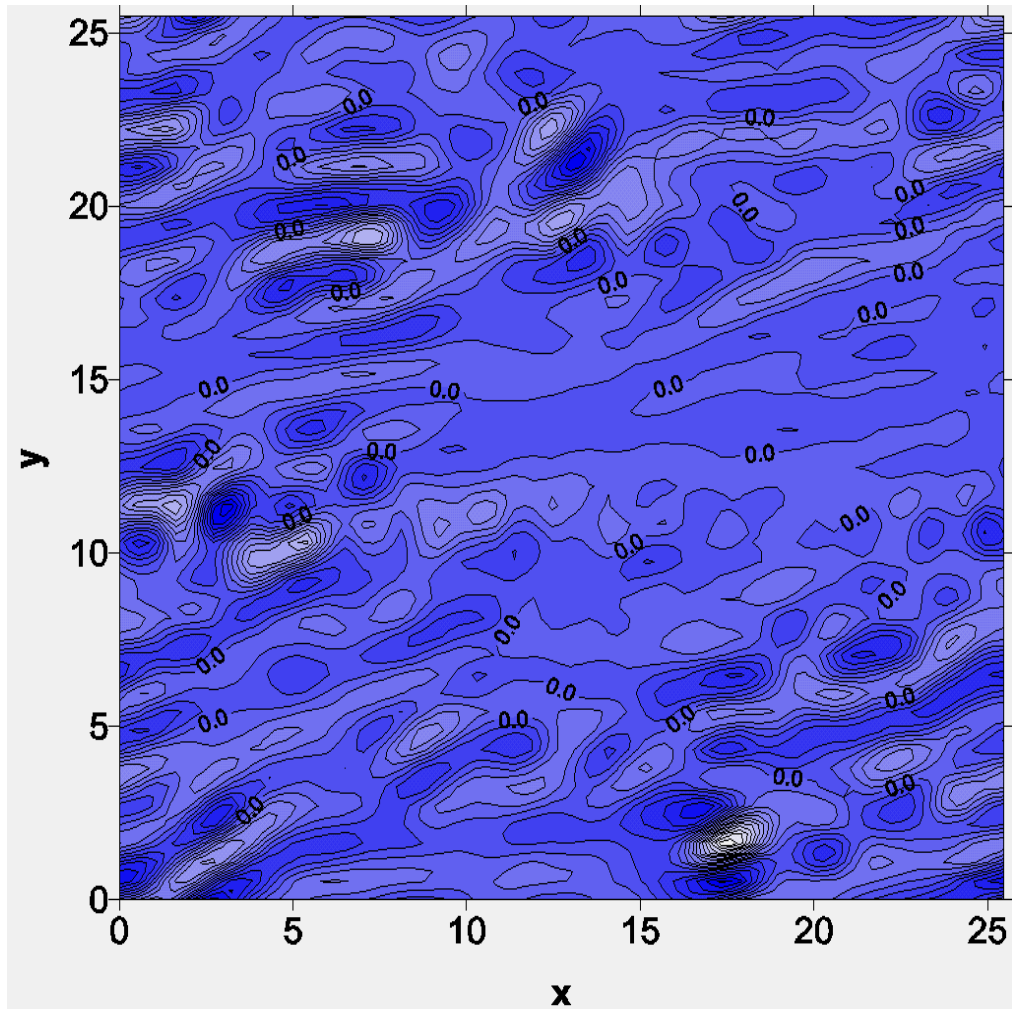


Figure 9: Contour plot of the vertical velocity, w , at a height $z/D = 0.03$.

Stable Stratification

The neutral stratification comparisons discussed above indicate that our model is working well when $Ri_b = 0$. For stable stratification, $Ri_b > 0$, we cannot evaluate our complete model by a similar head-on-head model comparison because, as far as we

know, the constant heat flux lower boundary condition makes our model unique. Comparisons with other models are therefore virtually impossible. However, the linear parts of the model can be assessed by first, turning off the nonlinear parts of the model; second, fixing the temperature profile so that the buoyancy frequency, N , remains constant in time and space; and finally, initializing the model with a low level of Gaussian noise. The model is run, and roll cells develop characteristic of linear Ekman layer stability theory. The growth rates and wavelengths of these cells can be compared to theory, and the degree to which the simulation matches the theory is an indication of how well the linear parts of the full model are working. This comparison is show in Table 6.

Table 6: Growth rates from model and linear stability theory, $Re = 400$, $Pr = 0.7$.

Ri_b	\mathbf{a}	\mathbf{e}_r	growth rate (DNS)	growth rate (linear theory)
0.0	0.5404	26.56	0.019262	0.019263
0.005	0.5404	26.56	0.013342	0.013344
0.01	0.5404	26.56	0.007177	0.007037

In this table \mathbf{a} is the wavenumber of the roll cell and \mathbf{e}_r is the orientation of the cell with respect to the geostrophic wind. \mathbf{a} and \mathbf{e}_r are the same for each run because of the discrete nature of the DNS. The fastest growing roll cell for all Ri_b in this table occurs at discrete wavenumbers of $k_x = -1$ and $k_y = 2$ corresponding to the \mathbf{a} and \mathbf{e}_r indicated above. The agreement between growth rates is very favorable with virtually no difference except at $Ri_b = 0.01$ and here the difference is small. Thus it appears that the linear parts of the model associated with both stratified and unstratified flow are working well. We know that the non-linear parts associated with neutrally

stratification are reliable from the discussion of the previous section, and the non-linear parts of the heat equation were checked for energy conservation. All these checks indicate that the DNS is working well.

We close this section by making a few comments regarding the linear stability code from which the results in Table 6 are obtained. This code was developed using a spectral Galerkin method similar to that described previously, and the vertical discretization is provided by the same basis functions employed in the DNS. This code was checked by writing another code based on an entirely different numerical method (Melander, 1983). When fed the same input conditions the output from both codes is virtually identical and similar to other published results (e.g., Brown, 1972; Coleman et al., 1990b; Kaylor and Fallor, 1972; Lilly, 1966).

The Continuous Spectrum of Eigenvalues

A notable feature of the stability code is its ability to reproduce some of the continuous spectrum of eigenvalues associated with the stable, laminar Ekman layer. Part of the complete eigenvalue spectrum is depicted in Figure 10, where the continuous spectrum is shown by the black dots and the discrete spectrum is shown by the circled dots. This spectrum came from a linear stability analysis with parameters: $Re = 400$, $Pr = 0.7$, $Ri_b = 0.005$, $\mathbf{a} = 0.5404$ and $\mathbf{e}_r = 26.56$. The continuous spectrum consists of three parts: one associated with neutral stratification, and the other two associated with stratification. This three-part structure is evident in Figure 10 as the three prongs of a “pitchfork” pattern. An analysis of the continuous spectrum can be carried out based on an extension of the work of Grosch and Salwen (1978) and Craik (1991) concerned only with the continuous spectrum of the Orr-Sommerville equation over a semi-infinite domain. A comprehensive exposition of the continuous spectrum for the stratified Ekman layer, although interesting, is not central to the goals of this thesis but a brief analysis is outlined in Appendix A.

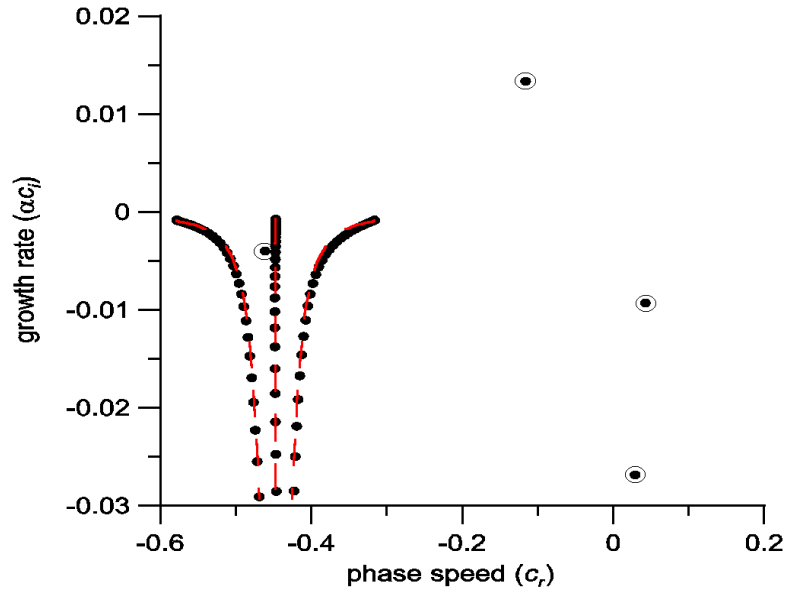


Figure 10: Part of the eigenvalue spectrum derived from a linear stability analysis of the laminar Ekman layer. The dots are the continuous spectrum while the circled dots represent the discrete spectrum. The dashed lines are a closed-form solution for the continuous spectrum, with $Pr = 0.7$.

In this appendix it is shown that for $Pr = 1$, the complex phase speed, c , (where c is in the expression for the disturbance, $\hat{w}_a(z)e^{-ia(x-ct)}$) is given by three simple, closed-form equations (eq. 2.91) where b is a parameter that ranges from zero to infinity, and \mathbf{e}_k is the angle that the wavenumber, \mathbf{k} , of the disturbance makes with the x -axis. The uppermost equation in eq. 2.91 is associated with the continuous spectrum of the Orr-Sommerville equation, while the bottom two components are the continuous spectrum associated with stratification.

$$c = \left\{ \begin{array}{l} \cos(\mathbf{e}_k) - \frac{1}{ia \text{Re}} (b^2 + \mathbf{a}^2) \\ \cos(\mathbf{e}_k) - \frac{\sqrt{\text{Ri}_b + \frac{b^2}{\mathbf{a}^2 \text{Ro}^2}}}{\sqrt{b^2 + \mathbf{a}^2}} - \frac{1}{ia \text{Re}} (b^2 + \mathbf{a}^2) \\ \cos(\mathbf{e}_k) + \frac{\sqrt{\text{Ri}_b + \frac{b^2}{\mathbf{a}^2 \text{Ro}^2}}}{\sqrt{b^2 + \mathbf{a}^2}} - \frac{1}{ia \text{Re}} (b^2 + \mathbf{a}^2) \end{array} \right\} \quad (2.91)$$

The three branches of the continuous spectrum have been added to Figure 10 as the three dashed lines. These three lines have been calculated from theory for $\text{Pr} = 0.7$ (although the difference between the spectra for $\text{Pr} = 0.7$ and $\text{Pr} = 1.0$ results is minimal, and we could just as well use the expressions contained in 2.91 above). The agreement between the numerical and theoretical results is very good in this range of the continuous spectrum. For large negative growth rates, the divergence between the analytic and numerical results becomes larger than what might be surmised from Figure 10.

Summary – Evaluation of Model Performance

Our model has been tested in several ways. The comparison between the neutrally stratified simulations of Coleman et al. (1990a) and our model suggest that the neutrally stratified parts of our model are working well. Based on an examination of 1-D spectra of vertical velocity the resolution of our model appears to be adequate because no peculiarities have been noticed in the spectra that might indicate, for example, a pile up of energy at the high wavenumbers. A comparison of the disturbance growth rates from the fully stratified model (without the nonlinear mechanisms) with the growth rates from a linear stability analysis looks very good. The results from all these tests, taken together, form a picture of a model that is doing

what it is supposed to be doing: accurately solving the Navier-Stokes equations for stratified flow at low Reynolds number.

CHAPTER 3: DIRECT NUMERICAL SIMULATION OF THE VERY STRATIFIED EKMAN LAYER - RESULTS

3.1 DEFINITION OF THE VERY STABLE BOUNDARY LAYER IN TERMS OF VARIOUS STABILITY PARAMETERS

In this chapter we describe the use of the DNS technique to examine the issues brought forth in the Introduction. Taking on the first issue, we ask: How can the VSBL be delineated in terms of various stability parameters (e.g., z/L , z/Λ , B_o/B_{\max} , Ri_b)? As we have repeatedly emphasized, the VSBL is distinguished from its less stable counterpart by the temporal and spatial distribution of turbulence. For the less stable boundary layer the turbulence is continuous while in the VSBL turbulence becomes intermittent or disappears entirely (see Mahrt et al., 1998; see also Mahrt, 1999 for a brief discussion of intermittency). If we consider an ensemble of stable boundary layers, ordered from less stable to more stable in terms of some stability parameter, then the start of VSBL may be considered as that stability parameter at which the turbulence just starts to become intermittent. The goal here is to assign a numerical value to the chosen stability parameter that marks the boundary between the very stable and less stable regimes, and to determine if the value of the DNS-derived parameters are similar with those derived from field studies and theory.

How can the DNS help delineate these parameter values? Our strategy is to run the DNS at various increments of the “intrinsic” stability parameter, Ri_b . Starting from Ri_b equal to zero, the stratification is increased at intervals of 0.001 up to $Ri_b = 0.006$. We also ran a simulation at $Ri_b = 0.10$. All runs start from an initial, neutrally stratified, quiescent state initialized by low levels of Gaussian noise. The runs are allowed to develop under neutral conditions and at time $tf = 15$ -- at which time we

are assured that the neutrally stratified flow is fully developed -- we apply a cooling heat flux at the surface. We then search time series of surface friction velocity as well as other quantities looking for evidence of the intermittency that signals very stable conditions. This procedure is illustrated in Figures 11 and 12 in which time series of the surface friction velocity (u_* / G , Figure 11) and \mathbf{b} (the angle that the stress makes with the geostrophic wind, Figure 12) are shown at Ri_b values of 0.001, 0.004, and 0.005. The “markers” u_* / G and \mathbf{b} serve as rough indicators of the presence or absence of turbulence. However, before identifying areas of possible intermittency, we point out a few general features common to all the time series. The initialization procedure is evident in the first part of all the series, in which a laminar Ekman instability develops (from $tf = 0$ to about $tf = 2$) followed by a transition to turbulence. The transition appears to be complete at about a time of $tf = 8$ and the flow is allowed to continue in this neutrally stratified state until $tf = 15$, at which time the surface is cooled. This cooling quenches the turbulence in rough proportion to the strength of the cooling. As the downward heat flux is increased from one simulation to the next, the stratification eventually will become strong enough so that the turbulence becomes intermittent. Such an intermittent state would consist of quiet, near-laminar flow during which values of u_* / G and \mathbf{b} hover close to their laminar values, juxtaposed against more turbulent states for which these variables move away from their laminar values. A simple analysis applied to the laminar Ekman layer shows that u_* / G and \mathbf{b} have “laminar” values of $(\sqrt{2}/Re)^{1/2}$ ($= 0.05946$ at $Re = 400$) and 45° , respectively. Returning to Figures 11 and 12 we can now screen for states of intermittency as evinced by oscillations of the marker variables (u_* / G) and \mathbf{b} between laminar and turbulent states. Glancing at the uppermost panel, $Ri_b = 0.001$, we see that there are oscillations in the marker variables but the time series show no evidence of laminar conditions after the heat flux is turned on. This is in marked contrast to the later stages

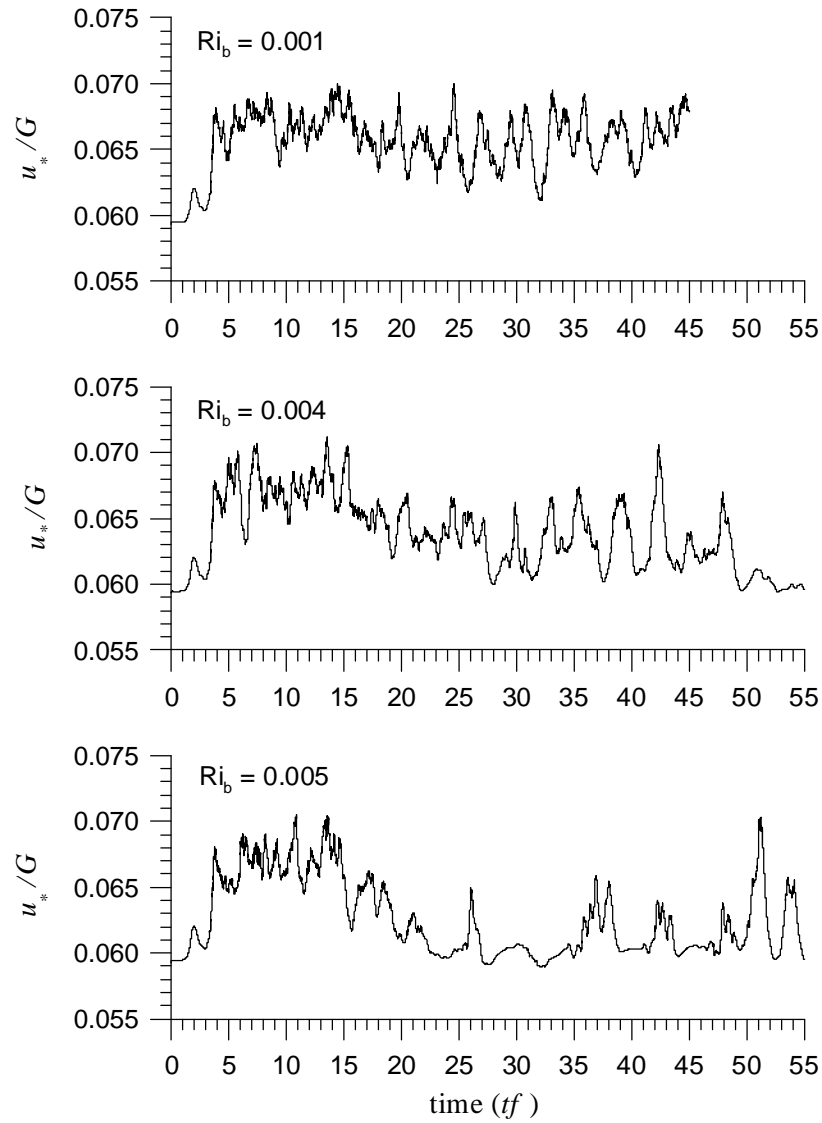


Figure 11: Time series of the surface friction velocity, u_*/G . The times series are plotted for three values of the bulk Richardson number, Ri_b . The surface heat flux is turned on at time $tf = 15$. The case $Ri_b = 0.001$ only extends to time $tf = 45$.

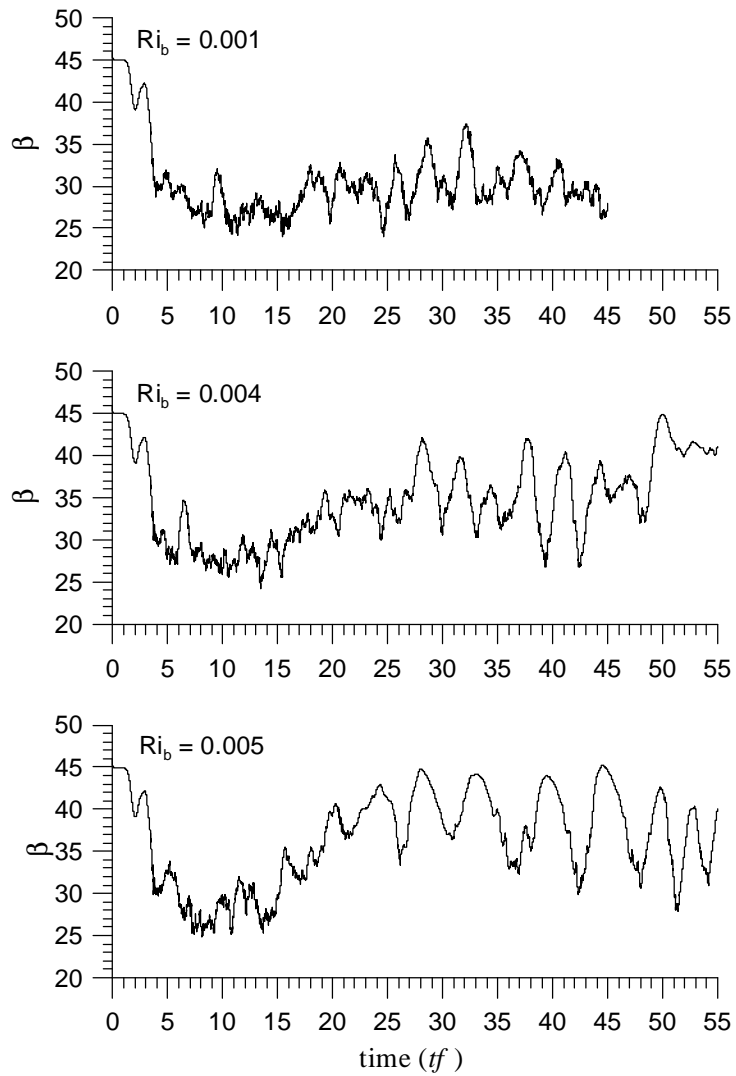


Figure 12: Time series of the β , the angle that the surface stress makes with the geostrophic wind. Three time series are plotted corresponding to Ri_b equal to 0.001, 0.004, and 0.005. The case $Ri_b = 0.001$ extends only to $tf = 45$.

of the $Ri_b = 0.004$ case (tf greater than about 45) and almost all of the $Ri_b = 0.005$ case, after the transient behavior associated with the abrupt cooling has died off (tf greater than about 25). In these time ranges there are frequent excursions of the marker variables to and from their laminar values, and for significant periods of time the flow appears to be in a laminar state. For example, for the case $Ri_b = 0.005$, the flow in the time period between $tf = 39$ and $tf = 42$ looks laminar as signaled by the values of the marker variables, and this period is sandwiched between two turbulent states. A visual examination of the flow fields during this time of supposed laminar behavior reveals that the flow is indeed laminar or nearly laminar (a visual display of the flow will be provided later in this section). It is interesting to note that the interval between two laminar episodes has a period of about $tf = 2\pi$, or one inertial period; this, too, will be discussed later.

A more graphic and detailed illustration of the intermittent nature of the turbulence can be had by a closer examination of the time period $tf = 39$ through $tf = 46$ ($Ri_b = 0.005$). The turbulent (kinematic) heat flux from this period is shown in Figure 13 where the

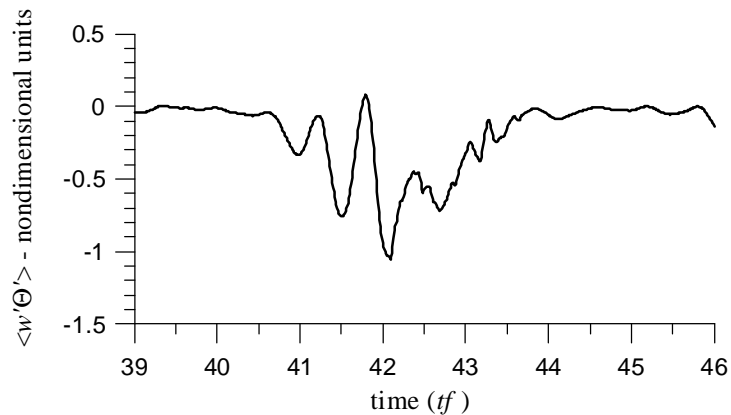


Figure 13: Kinematic turbulent heat flux,
 $Ri_b = 0.005$.

intermittent condition of the turbulent heat flux is vividly apparent. At both ends of the time interval the heat flux is nearly zero, indicating little or no turbulence, while in the center of the interval the heat flux oscillates dramatically and even becomes positive for a short time (a countergradient heat flux!). From this visual appraisal it is possible to identify a bulk Richardson number of about 0.005 (or maybe a little less) as that Richardson number where the VSBL begins.

Merely stating that the VSBL begins at this value of Ri_b is not very useful because in a practical sense the bulk Richardson number as defined here (eq. 2.24) is a quantity that is rarely, if ever, measured in the field, thus rendering comparisons between the DNS and field studies problematic. The analysis of the simulations is much more meaningful if more conventional stability parameters are brought into the picture because meaningful comparisons between the DNS and various modeling and field studies become possible. For each parameter we must find the range of this parameter that “maps” into the VSBL. As discussed in the Introduction, there have been two parameters proposed as signposts for the boundary of the VSBL. These are the surface heat flux (B_o), and one parameter based on the local Obuhkov lengths, z/L . We first examine z/L .

3.1.1 z/L AND THE FLUX INTERMITTENCY FACTOR

One stability parameter that is sometimes measured in the field and that has great theoretical import is the parameter, z/L ¹². Howell and Sun (1999) have identified the VSBL using a flux intermittency factor, I_f , that indicates the presence or absence of

¹² The theoretical significance of this parameter stems from its use in Nieuwstadt’s (1984) local scaling theory. One of the central tenets of this theory is that appropriately scaled variables that describe turbulent flow (variances, covariances, and the gradient Richardson number) should approach constant values as z/L goes to infinity. This idea makes sense because for very stable conditions (large z/L) the turbulence will only be influenced by local conditions -- the vertical transport having been suppressed by the strong stability. This amounts to the “ z -less stratification” proposed by Wyngaard (1973).

significant flux variability over a given interval of time. This factor may be defined in the following manner (adapted from Howell and Sun, 1999). Let \bar{F} be the average (heat or momentum) flux over the time interval Dt ; we divide this interval into N subintervals of duration Dt/N . The flux of each subinterval is f_i , and the fractional contribution that this flux makes to the average flux, \bar{F} , is f_i/N . We then order all the f_i/N from largest to smallest and we form the partial sums, $S(m) = \sum_{i=1}^m f_i/N$, beginning from the largest f_i/N and working toward the smallest. The smallest M such that $S(M) \leq 0.9\bar{F}$ is the minimum number of subintervals required to equal 90% of the average flux \bar{F} . We then define the flux intermittency factor as $I_f = (1-M/N)$, where I_f is a number between zero and one.

One can easily understand the flux intermittency factor by looking at the two asymptotic limits. The first of these is when all f_i are equal to \bar{F} , in which case there is no flux intermittency over the time interval in question because the flux is constant. In this limit, M is approximately equal to N and $I_f \approx 0$. By contrast, assume that all the flux is contained in one subinterval and all the other f_i are zero. In this limit $I_f \approx 1$. Mindful of these two limits, we see that the flux intermittency factor provides an easily understood and conveniently computed measure of the intermittency over any given time interval.

For the DNS simulations, we can find this factor and graph it against the stability measure z/L as was done by Howell and Sun (1999) using actual field data from the MICROFRONTS experiment. As z/L increases, we expect that I_f might increase as well. The field studies show that this increase does not occur in a linear manner and, over a wide range of z/L , I_f remains essentially flat. For convenience, we reproduce below Figure 2 (now labeled Figure 14), and the figure shows this flat behavior up until

$z/L \approx 1$ after which the flux intermittency increases. At this point we say that the VSBL begins.

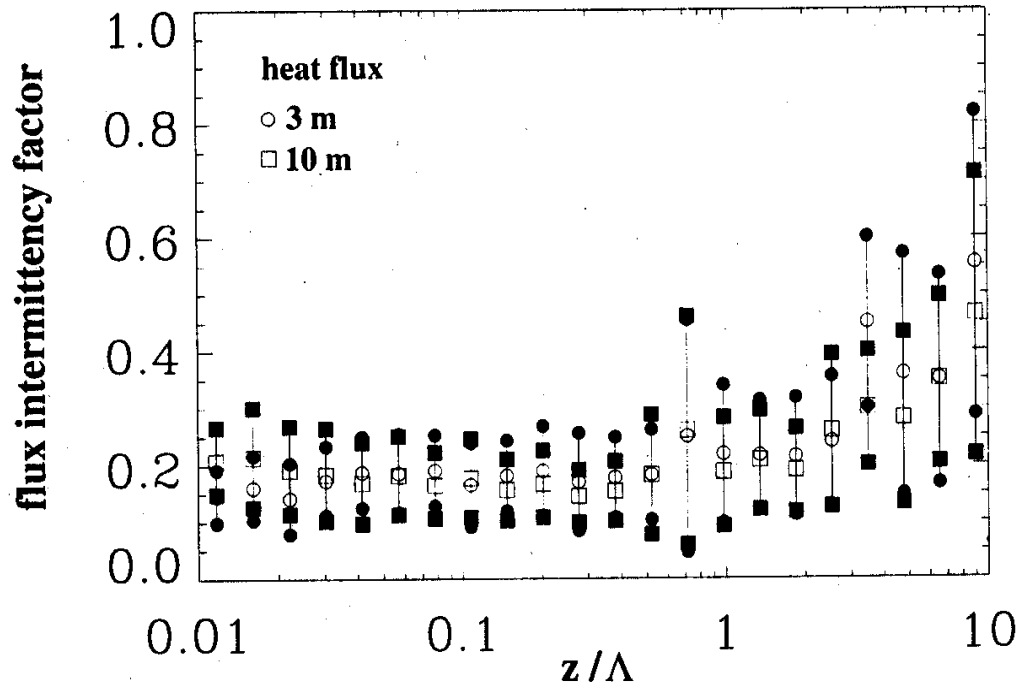


Figure 14: Flux intermittency factor as a function of the stability parameter, z/L . The flux intermittency factor is flat over a wide range of the stability parameter and only begins to increase for $z/L > 1$. (This figure is taken from Howell and Sun, 1999).

The question is whether this behavior will be seen in the DNS. If so, it would suggest that defining the very stable boundary in terms of the parameter z/L is very likely to be a good strategy because it has been confirmed in both modeling and field studies. We remind ourselves that the local Obukhov length, L , is defined in terms of the local

friction velocity and the local heat flux and may be written in nondimensional form

$$\frac{\Lambda}{D} = \frac{\left[\overline{(u'w')^2} + \overline{(v'w')^2} \right]^{3/2}}{\mathbf{k} \text{ Ri}_b \overline{w' \Theta'}} \quad (3.1)$$

where we have used the relationship $u_*^2 = \mathbf{t} / \mathbf{r} = \sqrt{\overline{(u'w')^2} + \overline{(v'w')^2}}$ and the turbulent heat and momentum fluxes are all measured at one specific height, z , above the surface. An important consideration in calculating L from the DNS is this choice of this height.

Observations of the heat flux in stable boundary layers (see Garratt, 1992, who summarizes the work of Nieuwstadt, 1984, and others) indicate that the turbulent heat flux in moderately stable boundary layers decreases linearly with height. This is not true in the DNS because of the low Reynolds number of the flow. This low Reynolds number implies that effect of viscosity is large enough to suppress the turbulence in the vicinity of the lower boundary. Of course, this suppression near a solid boundary happens in flows with very large Reynolds number but, for these flows, the “reach” of viscous effects above the surface is very small and is usually confined to a thin viscous sublayer (Schlichting, 1968, page 531). This is not so in the low Reynolds number simulations performed here in which viscous effects protrude far into the turbulent boundary layer. It seems appropriate, therefore, to pick a height above the surface where viscous effects are considerably diminished.

An examination of turbulent heat flux profiles has shown that the flux is zero at the surface (naturally) and gradually increases with height and reaches a maximum at a height of about $z/D = 2.5$. Even at this height the viscous contribution to the heat flux is on the order of 20%. Above this height, the heat flux decreases to zero in an approximately linear manner. We therefore choose as our reference height $z/D = 2.44$.

This is the quadrature point closest to the level of the maximum heat flux, and we calculate z/L and the flux intermittency factor at this height.

An average z/L and I_f is calculated for each Ri_b between the times of $tf = 25$ and $tf = 45$. We recall that the heat flux is turned on at time $tf = 15$, after which the flow adjusts to a new state of stable stratification. All flows seem to have completely adjusted to the applied heat flux after time $tf = 25$ implying an adjustment time of much less than ten. Coleman et al. (1992) find that for light stratification the adjustment time is very small, $tf = 0.5$, corresponding to about one-half an eddy turn over time (defined as vertical average of q^2/ϵ , where q is the turbulent kinetic energy “velocity” and ϵ is the dissipation rate). This very quick rate of adjustment seems to be observed only for our simulations with mild stratification, $Ri_b = 0.001$. For the more stratified simulations the adjustment appears to take somewhat longer. If we define equilibrium as the achievement of a steady mean in the global variables u_*/G and b , then for the case $Ri_b = 0.004$, equilibrium appears to be reached by time $tf = 25$ and persists until about time $tf = 35$ after which z/L increases with a concomitant increase in the flux intermittency. Therefore for this case we calculate an average z/L and an average I_f for the time interval extending from $tf = 25$ to $tf = 35$ and another set of averages for $tf > 35$.

For the DNS simulations the flux intermittency factor is plotted versus z/L in Figure 15. Comparing this figure to the results of the field studies shown above in Figure 14, it is clear that the pattern of the flux intermittency factor is similar between the two figures: the flux intermittency factor stays flat over a wide range of z/L followed by an increase with larger values of the stability parameter. The DNS results indicate that the increase begins at about a z/L equal to about 0.8, while for the field studies this increase does not start until about $z/L \approx 2$ and the increase is more gradual. Other

studies (Smedman, 1988, as described in Mahrt [1999]) show that markers of intermittency, specifically velocity standard deviations, “turn up” at somewhat lower

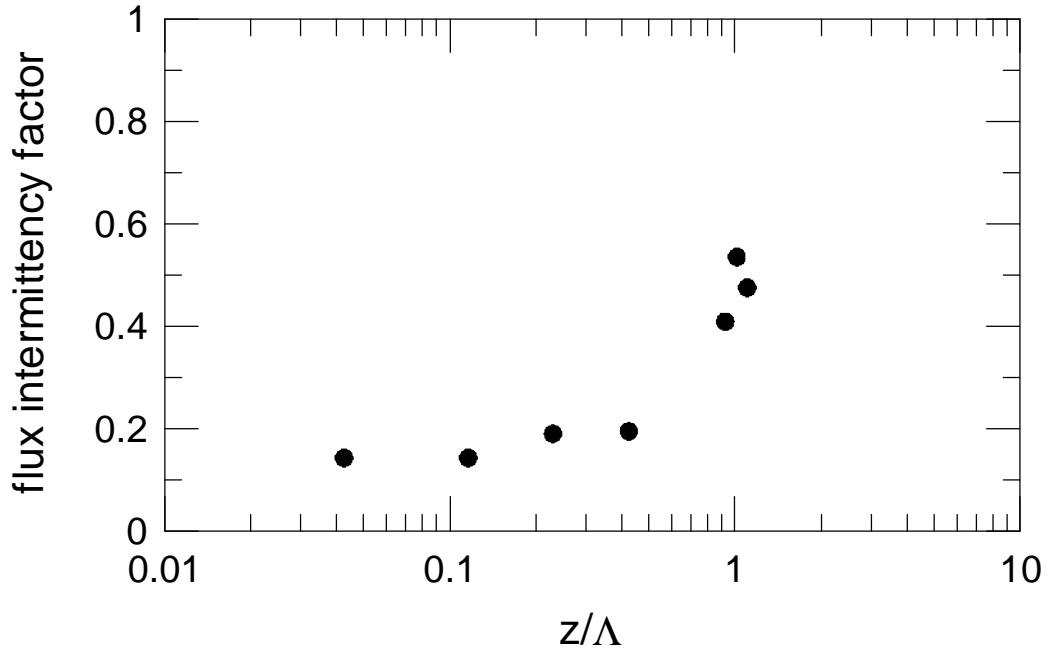


Figure 15: Flux intermittency factor, I_f , calculated from the DNS simulations.

values of z/L ($\approx z/\mathbf{L}$) than the upturn pictured in Howell and Sun. In this regard the findings of Smedman are quite consistent with the DNS results. Given the difference between the very idealized DNS simulation and the real atmosphere, we conclude that the agreement between the simulations and the field studies is very good. This agreement supports the notion expressed by Howell and Sun (1999) that the VSBL exists in the parameter range $z/\mathbf{L} \geq 1$. This good agreement also lends credibility to the DNS as a “reasonable idealization” of real VSBLs.

That the VSBL begins at $z/\mathbf{L} \geq 1$ seems consistent with Nieuwstadt’s local scaling hypothesis (Nieuwstadt, 1984). In this theory the strong stability limit occurs formally

in the asymptotic limit as $z/L \rightarrow \infty$, at which time appropriately scaled dependent variables reach their asymptotic values. One such variable is the gradient Richardson number. Figure 16 (from Nieuwstadt, 1984) shows values of the gradient Richardson number, Ri_g , derived from field data as well as a prediction of Ri_g from a model based on local scaling theory. At $z/L \approx 1$ the gradient Richardson number is close to approaching to its “strong stability” value of about 0.2, thereby suggesting that $z/L \approx 1$ is a reasonable lower limit for the strong stability regime. These findings, considered along with the results from the DNS, Howell and Sun (1999), and Smedman (1988) all paint a fairly consistent picture: the VSBL exists for all z/L such that $z/L \geq 1$.

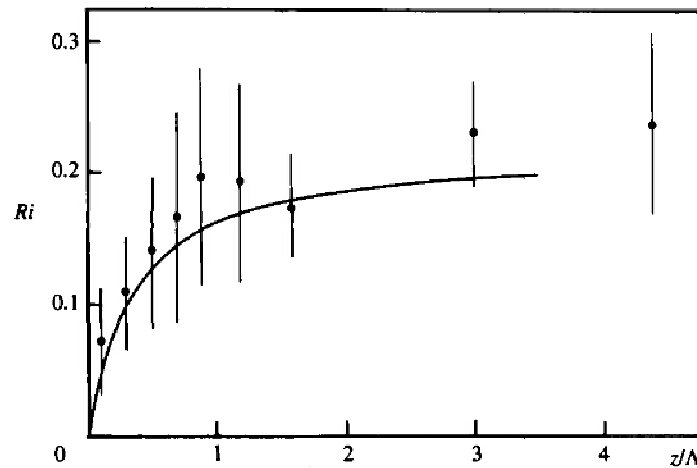


Figure 16: The gradient Richardson number plotted versus the local stability parameter, z/L (adapted from Nieuwstadt, 1984). The curve is from a model based on the local scaling theory while the filled circles with error bar represent values of the gradient Richardson number derived from field studies.

3.1.2 THE MAXIMUM HEAT FLUX CRITERION

In this section, we use DNS to examine the criterion established by Derbyshire (1990) for the start of the VSBL. This criterion, derived from theory, is based on the idea of the maximum surface heat flux, B_{\max} , that can be supported by stationary, fully turbulent flow (Mahrt et al., 1998). For heat fluxes close to this value or just slightly greater, the boundary layer may exhibit the intermittent behavior characteristic of the VSBL.

The maximum heat flux can be formally derived from a singular perturbation (Derbyshire, 1990) but it is perhaps easier to understand this idea using a simple physical argument (also proposed by Derbyshire, 1990, although we present his argument in modified form). The physical underpinnings of the maximum heat flux criterion arise from the energy considerations: the buoyant production/destruction of turbulent kinetic energy (TKE) should be some fraction of the total input of energy to the system. We start from the definition of the flux Richardson number, Rf ,

$$Rf = \frac{\text{buoyant production}}{\text{shear production}} = \frac{\frac{g}{\Theta_o} \overline{w'\Theta'}}{\overline{u'w'} \frac{\partial u}{\partial z} + \overline{v'w'} \frac{\partial v}{\partial z}} \quad (3.2)$$

thus, by definition, $\text{shear production} = \text{buoyant production}/Rf$. For stationary conditions, Rf is approximately constant throughout the boundary layer (Nieuwstadt and Tennekes, 1981; Nieuwstadt, 1984). With Rf constant, we rearrange eq. 3.2 and integrate over the depth of the boundary layer.

$$\int_0^{\infty} (\text{shear production}) dz = \frac{1}{Rf} \int_0^{\infty} (\text{bouyant production}) dz \quad (3.3)$$

An upper bound to the shear production can be estimated by equating the total mechanical input to the atmosphere, T , to the shear production. This is work done against the ambient pressure gradient or

$$T = -\frac{dp}{dy} \int_0^{\infty} v(z) dz > \int_0^{\infty} (\text{shear production}) dz \quad (3.4)$$

In eq. 3.4, $v(z)$ is the mean wind speed in the y direction and dp/dy is the ambient pressure gradient. Continuing on in the spirit of approximations described above, we take $v(z)$ to be $Ge^{-z/D} \sin(z/D)$ and $dp/dy = -fG$. Our estimate of the total mechanical input is therefore $fG^2D/2$ ($> \text{shear production}$).

The total buoyant production (or destruction), K , is given by

$$K = \int_0^{\infty} \frac{g}{\Theta_o} \overline{w'\Theta'} dz \quad (3.5)$$

Theory (Nieuwstadt, 1984) indicates that, for the strongly stratified boundary layer, the turbulent heat flux is a linear function of height, and we have $\overline{w'\Theta'} = \overline{w'\Theta'}_s (1 - z/h)$ for z in the range $[0, h]$ and where $\overline{w'\Theta'}_s$ is the surface heat flux and h is the height of the boundary layer. Integration then yields $K = g/\Theta_o \overline{w'\Theta'}_s h/2$. The flux Richardson number, Rf , under very stable conditions is about $1/4$ (Nieuwstadt, 1984) and D/h is about $1/5$. Solving for the surface (kinematic) heat flux, we have

$$\overline{w'\Theta'}_s < Rf |f| G^2 \frac{\Theta_o}{g} \frac{D}{h} \quad (3.6)$$

With $f = 10^{-4} \text{ sec}^{-1}$, $G = 10 \text{ m/sec}$, $g = 10 \text{ m/sec}^2$, and $\Theta_o = 300^\circ \text{ K}$ we have $\overline{w'\Theta'}_s < 0.015 \text{ m/sec } ^\circ\text{K}$. This amounts to an upper bound for the maximum surface heat flux, B_{\max} , of about 20 W/m^2 . A more refined estimate of B_{\max} can be obtained by a rigorous

calculation based on a singular perturbation (Derbyshire, 1990) in which the heat flux follows naturally in the limit of strong stability. This calculation gives

$$\overline{w'\Theta'_s} < Rf|f|G^2 \frac{\Theta_o}{g} \frac{1}{\sqrt{3}} = B_{\max} \quad (3.7)$$

from which we infer a numerical value of B_{\max} of about 40 W/m^2 (in units of an energy flux). Although the two estimates differ, the important point is that both values are roughly in agreement with observed downward surface heat fluxes in nocturnal boundary layers; the range of observed heat fluxes is about -100 W/m^2 to 0 W/m^2 ; Shaw, 2000 (the negative sign indicates a flux directed towards the surface).

The use of maximum heat flux as a sign for the start of the VSBL poses some problems when this concept is tested using a numerical model. In particular one must distinguish between the downward heat flux imposed at the lower boundary of a model as a boundary condition and the turbulent heat flux within the model's interior. The heat flux at the boundary is specified, and it can assume any value regardless of whether the value is realistic of the atmosphere or not. The turbulent heat flux above the boundary responds to the imposed flux, because in the absence of other effects such as radiative cooling, the surface heat flux "sets" the stability of the atmosphere. The interior, turbulent heat flux responds to the stability, and it may collapse if the imposed downward heat flux is large enough to squelch the turbulence. The interior flux is therefore limited by physics, while the imposed lower heat flux is unlimited and set by fiat of the modeler.

Keeping in mind the difference between the interior flux and the imposed surface flux, the question now becomes: in our DNS simulations can the maximum interior turbulent heat flux be associated with the beginning of VSBL? Our strategy here is to vary the imposed surface heat flux and thereby change the ambient stratification of the flow. We monitor the interior heat flux (averaged over at least several inertial periods) and,

when it reaches a maximum, we then look for evidence that we are in the regime of the VSBL. Again, we are looking for flux intermittency. From this simple test we can assess the validity of the maximum heat flux criterion as a marker for the boundary between the merely stable boundary layer and the VSBL.

To facilitate the comparison between the DNS fluxes and those in the real atmosphere it is useful to “calibrate” the DNS so that the dimensional heat fluxes assume values that are characteristic of the atmosphere. First, we remind the reader that the low Reynolds number of the flow ($Re = 400$) implies, in terms of a physical height, a very small boundary layer. For example, a boundary layer with a scale height about 0.06 meter and a geostrophic wind of about 0.1 m/sec gives a Reynolds number of $GD/\mathbf{n} = (0.06 \text{ m/sec} * 0.1 \text{ m}) / (1.6 \times 10^{-5} \text{ m}^2/\text{sec}) \approx 400$. The heat flux required to cool this small boundary layer by, say, a degree per $\frac{1}{2}$ day (one inertial period) is obviously very small, on the order of 10^{-3} W/m^2 . This tiny flux is very much less than that required to cool an atmospheric boundary layer by a similar rate. The calibration we propose here artificially scales up the simulation so that realistic heat fluxes are calculated.

This calibration follows a simple procedure. From the definition of the bulk Richardson number, eq. 2.24, the downward dimensional surface heat flux, H , may be written as

$$H = \frac{Ri_b}{RePr} \frac{G^2}{gD} r c_p G \Theta_o \quad (3.8)$$

where c_p is the heat capacity of air. With $Ri_b = 0.005$, $Re = 400$, $Pr = 0.7$, $G = 0.06 \text{ m/sec}$, $D = 0.1 \text{ m}$, $\Theta_o = 300 \text{ }^\circ\text{K}$, and $r = 1.25 \text{ kg/m}^3$, the heat flux is equal to about 10^{-3} W/m^2 . By contrast a typical heat flux is 40 W/m^2 and the ratio of the two is our calibration factor of 40×10^3 . To calibrate our DNS surface heat fluxes we merely multiply the DNS flux numbers by this factor. It is interesting to note that when the

Reynolds number of our DNS is multiplied by the calibration factor, the resulting Reynolds number is roughly 10^7 . This is comparable to Reynolds numbers typical of atmospheric boundary layer flow (Stull, 1991, page 93). This result is surprising because there is no reason to expect the heat flux to scale linearly with the Reynolds number and such agreement seems merely a coincidence.

The imposed surface heat flux (dashed line) and the interior turbulent heat flux (dots) are plotted in Figure 17 versus bulk Richardson number, Ri_b . The turbulent heat flux is calculated at discrete values of Ri_b in increments of 0.001 from $Ri_b = 0$ to $Ri_b = 0.006$. An additional DNS simulation provides another point at $Ri_b = 0.01$. The “turbulent” flux at this point is entirely due to laminar motions. The flux (= 0) at $Ri_b=0.02$ is an estimate. At this large stratification we assume that the turbulent flux is completely extinguished by the very strong stratification. A smooth curve has been drawn through the points that represent the turbulent heat flux.

Figure 17 illustrates two points. The first of these is rather trivial: the imposed surface heat flux decreases linearly with an increase in Ri_b and that the imposed flux is generally much larger in magnitude than the interior turbulent heat flux. The second point is much more important and is the crux of our analysis. We see that the turbulent heat flux peaks in magnitude at a Ri_b equal to about 0.005. From our previous examination of the simulations, we have found that this value of Ri_b is about where the turbulence becomes intermittent and the VSBL begins. Thus, our findings support Derbyshire’s supposition that the maximum heat flux may be associated with the beginning of the VSBL.

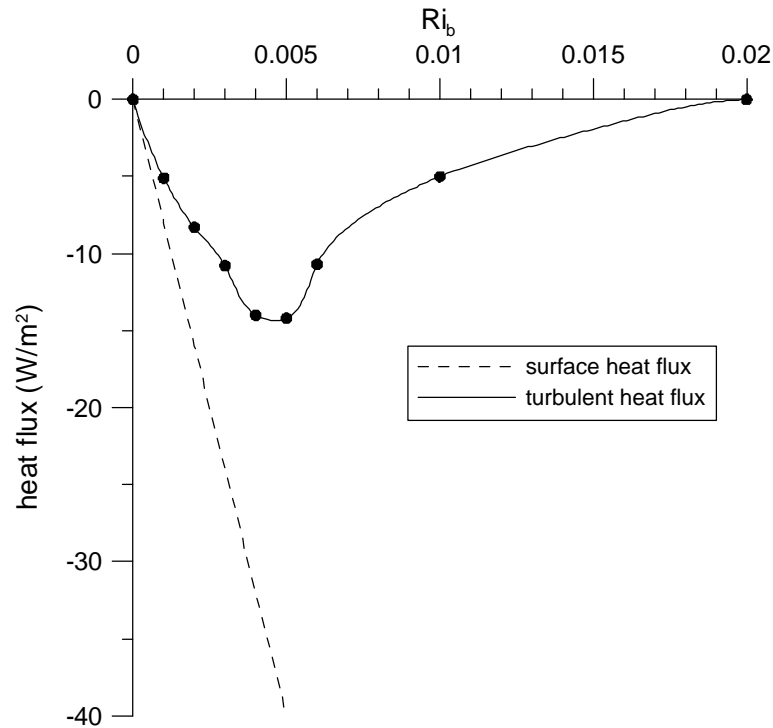


Figure 17: The imposed surface heat flux (dashed line) and the interior turbulent heat flux (dots) plotted versus Ri_b . A smooth curve has been fit to the turbulent heat flux points.

The heat fluxes shown in Figure 17 have been averaged over many inertial periods. (The averaging period began after the initial transient associated with the abrupt application of the surface flux had died off.) The relatively large values of the time-averaged heat flux that occur in the vicinity of $Ri_b = 0.005$ are averages of fluxes that are very intermittent in time (see for example, Figure 13). This very intermittent nature is again illustrated in Table 4, in which the turbulent fluxes are listed as well as their standard deviations over the averaging period. Clearly the flux intermittency as portrayed by the flux standard deviation is very large around $Ri_b = 0.005$ and decreases thereafter. The decrease at $Ri_b = 0.01$ is symptomatic of steady laminar “roll cell” motions that carry the turbulent heat flux

The standard deviations in Table 7 again support the notion of significant flux intermittency occurring when the flux itself is close to or at its maximum value. But after

Table 7: Average turbulent fluxes and flux standard deviations as functions of the bulk Richardson number, Ri_b .

Ri_b	flux (W/m^2)	flux standard deviation (W/m^2)
0	0	0
0.001	-5.1	1.2
0.002	-8.3	2.9
0.003	-10.8	4.5
0.004	-14.0	10.0
0.005	-14.2	14.0
0.006	-10.7	14.3
0.01	-5.0	2.3

reaching this conclusion, our work is still not finished because we must contend with the field study analyzed by Mahrt et al. (1998) in which intermittency did not occur at the point of maximum heat flux. Referring to Figure 2 in the Introduction we see that the maximum heat flux for this one particular study occurred at $z/L \sim 0.1$ whereas our modeling results indicate that the maximum heat flux occurs at an Ri_b equal to about 0.005. In turn, in the DNS a Ri_b value of 0.005 corresponds roughly to a z/L ($\approx z/L$) value of about 1. Thus, the DNS indicates that the maximum heat flux occurs at $z/L \sim 1$, and we have a difference between the DNS and the field study. This difference occurs in spite of the good agreement between modeled and measured flux intermittency as depicted in Figures 14 and 15.

We cannot reconcile this difference. However, it is important to reiterate the comments of Mahrt et al. (1998): “there is no evidence that the value of z/L corresponding to the maximum downward heat flux is universal.” Mahrt et al. also cite the study of Malhi (1995) in which the maximum flux occurs at $z/L = 0.2$. These findings also depend on height above the ground further rendering the situation even more ambiguous, however, from the scant number of field measurements, it does appear that the maximum heat flux occurs for thermal stabilities less than the range of stabilities where flux intermittency is observed. The uncertain nature of these findings underscores the need for more data and more simulations. More data could help resolve the issue of what values of z/L actually correspond to the maximum heat flux or even whether such an association is possible. Simulations run at higher Reynolds number and with a more realistic lower boundary condition on the heat flux (perhaps an actual surface energy budget) might also help reconcile the difference noted here.

Still, we take a justifiably positive tack here (The Dalai Lama and Cutler, 1998), and we assert that the DNS provides significant practical insight into the definition of the VSBL. From this practical, engineering point of view, defining the stable boundary layer in terms of z/L (or z/L) has one substantial advantage over the maximum flux criterion. With a little care these quantities can be readily inferred from field measurements (Arya, 1988) whereas determination of the maximum heat flux might require the examination of lengthy time series of flux data, and concomitant turbulence data, in the hopes of discovering from these measurements the maximum heat flux for which continuous turbulence is maintained. Obviously, at the present time, the maximum heat flux idea is much more a theoretical concept than a workable field parameter.

3.2 MECHANISMS OF INTERMITTENCY

Our discussion of the definition of the stable boundary layer has strengthened the case for using the stability parameter z/L as a practical way to mark the beginning of the VSBL. Once we know where to find the VSBL in “stability parameter space” we can begin to examine that intermittency of turbulence that most distinguishes the VSBL from its less stable counterpart. To discover what mechanisms lead to intermittency we follow a two-step process in which we first visually examine the flow to develop an intuitive understanding of the intermittency mechanism followed by a more rigorous analysis.

We must emphasize that the idealized nature of the DNS technique cannot support all possible mechanisms leading to intermittency. For example, there is no possibility of generating patchy turbulence from gravity waves originating from topographic forcing because there is no topography in the model. The lower boundary is flat! The fact the DNS cannot possibly admit all means of creating intermittency begs the questions to what possible mechanisms will be permitted by the physics and numerical scheme of our DNS.

The possible mechanisms of intermittency have been discussed in the Introduction and for convenience we repeat them here:

- intermittency that stems from gravity waves (breaking gravity waves, interaction with a critical layer, etc.)
- Kelvin-Helmholtz instability
- Ekman layer instabilities
- the Blackadar mechanism

Our arguments regarding what is possible and what is not possible in our DNS will be very qualitative. We first examine the potential of the DNS to propagate gravity waves. If this ability is absent or unlikely, then intermittency that ultimately comes from gravity waves cannot be present in the model. Critical for the existence of gravity waves is a stably stratified profile of temperature. The strength of this stratification is represented by the Brunt-Väisälä frequency, N . Plane linear gravity waves can only exist in the media if the frequency of the gravity wave is less than N , or $\omega < N$, where ω is the frequency of the gravity wave. In our model, an initially unstratified atmosphere with N equal to zero is cooled from below and the resulting diffusive, background temperature profile is such that N is greatest at the boundary and tapers off monotonically to zero with height. Thus plane gravity waves cannot propagate without modification throughout the vertical domain because they will soon reach a height where $\omega > N$. (Gill, 1982, points out that for vertical variations in N , the WKB approximation may be applied to propagating gravity waves to show that wave reflection does not occur; rather in this approximation the wave properties change in response to variations in N .)

An exhaustive analysis of gravity wave propagation in our model is beyond the scope of this study, but it seems reasonable to assert that because of the decline of N with height (a physical reason), and the poor vertical grid resolution above the boundary layer (a numerical reason), the presence of gravity waves in the model is unlikely, and if some gravity wave activity exists, it must be confined near the boundary. Additionally there is no obvious forcing that would beget gravity waves. These waves can be spawned by turbulence (e.g., Carruthers and Hunt, 1986; Riley and Metcalf, 1987) and by topography but the stability structure of the model combined with of the lack of topography would seem to preclude the generation of gravity waves by such means. Considering all these factors, we tentatively conclude that gravity wave activity is likely to be small in our simulations. This assertion was confirmed by a flow

animation that revealed some low amplitude fluid motions that were most likely inertial-gravity waves. These motions did not appear to be dynamically significant.

Next, we move on to the Kelvin-Helmholtz (K-H) mechanism, and we are immediately confronted with a mild philosophical dilemma. The classic K-H instability (Drazin and Reid, 1989) is appropriate for an inviscid, two-layer flow with one layer having a constant density and velocity overriding another layer with another different velocity and “optionally” a different density. This classic problem can be generalized to an inviscid problem with arbitrary background velocity and density as embodied in the Taylor-Goldstein equation. This more general problem is still classified as a K-H instability problem (see Drazin and Reid, 1989, page 321). If we take the Ekman layer as the background velocity profile, add a lower boundary, and then add a viscous term to the equations, this generalized K-H problem becomes that of the instability of a laminar Ekman layer, and our model permits such instabilities by design. We can easily distinguish between the Ekman instability and the traditional K-H instability by noting that the Ekman instability is associated only with the Ekman layer profile while the K-H instability is more general and may be found in any almost sheared flow, stratified or otherwise. (The K-H instability is often connected to roll-ups observed in the atmosphere, see Figure 1.4 in Drazin and Reid, 1989). Both instabilities are so-called inflectional instabilities (Brown, 1974; Drazin and Reid, 1989).

In our model, all of the physics are in place to permit the traditional K-H instability to occur, although the viscosity, relatively large with $Re = 400$, as well as the lower boundary would modify and perhaps completely inhibit the instability from developing. For example, in a DNS of turbulence in stratified sheared flow, Jacobitz et al. (1997) reported a dependence of the critical Richardson number on the (microscale) Reynolds number, and this finding suggests that other DNS simulations might have a Reynolds number dependence. Numerical parameters such as grid spacing and domain size would restrict the maximum and minimum wavelengths of the instability. We must

note, however, that the K-H instability has also been simulated in DNS simulations of unstratified mixing layers in domains that are *fully infinite* in the z -direction. (Rogers and Moser, 1992; for these simulations, the Reynolds number was 500 based on the “half velocity” and the initial vorticity thickness. This definition of the Re is roughly analogous to the definition of the Reynolds number associated with the Ekman layer. See also Staquet and Riley, 1989.) The simulations of Rogers and Moser had numerical resolutions somewhat greater than our model, but not markedly greater thus suggesting the possibility of observing isolated K-H instabilities in our simulations if the flow conditions (i.e., shear and stability profiles) are right. Whether such flow conditions and consequent instabilities show up in the simulations remains to be seen.

Focusing now on the remaining intermittency processes, we remark that, of necessity, the model has been designed to simulate the Ekman layer instability because the turbulence originates from it. The Blackadar mechanism does not rely on any specific instability. It is rather a sequence of events in which the existence of turbulence is modulated by the value of the Richardson number. Because there is nothing in the model design that would prevent such modulation from occurring -- indeed it must occur if the model is to have any physical verisimilitude -- the Blackadar mechanism has the potential of being observed in our simulations. Finally, we cannot help but state that other intermittency mechanisms may occur in the model that have yet to be discovered and named.

3.2.1 FLOW VISUALIZATION

One way to identify which process is active in creating intermittency is through the use of flow visualization. We first chose a period of time from our simulation with $Ri_b = 0.005$ where evidence of intermittency was observed in the time series of surface friction velocity as depicted in Figure 11. The choice of what time period to study is rather arbitrary and we chose the interval of time extending from $tf = 39$ to $tf = 46$ as a

case study. Figure 13 shows the nondimensional heat flux that occurs over this time interval in which irregular behavior is readily observed. A detailed view of this irregular behavior in the surface friction velocity and \mathbf{b} , the angle that the surface stress make with the geostrophic wind, is show in Figure 18 in which time series of these quantities are plotted. Recalling that the laminar values of u_* / G and \mathbf{b} for laminar flow

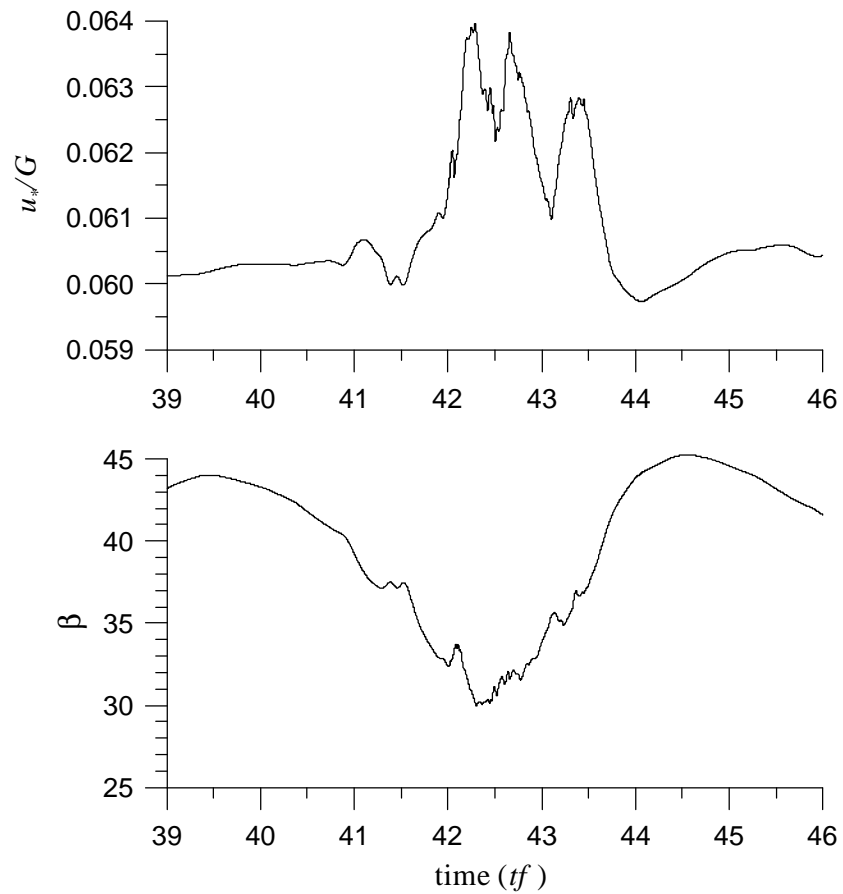


Figure 18: Detailed view of the surface friction velocity (u_* / G) and the angle that the surface stress makes with the geostrophic wind, \mathbf{b} .

are 0.05946 and 45° , respectively, we see evidence of irregular turbulent flow in a time interval extending from about $tf = 41.5$ to about $tf = 44$. On either side of this interval the flow appears to be laminar or near laminar.

Additional confirmation of the intermittent nature of the flow in the chosen time interval can be seen in Figure 19. This figure shows time series of vertical velocity measured by a fictitious probe placed in the fluid at a height of $z/D = 0.751$. The top panel of this figure depicts the vertical velocity measured under stably stratified conditions in the time interval chosen for study. For the sake of comparison, the bottom panel shows the same variable measured at the same height in a neutrally stratified flow. The intermittency of the stably stratified flow is vividly apparent, and the magnitude of the vertical velocity fluctuations in this flow equal or exceed those of the neutrally stratified flow. It is remarkable that the turbulence found in the simulations of the VSBL, when it occurs, is as strong as the turbulence found in the neutrally stratified simulations.

Flow Cross Sections

Once we are convinced that our case study contains significant intermittent behavior we examine cross-sections of the flow sampled from various times within the case study. First, we look at vertical and horizontal cross sections at the beginning of the time interval, $tf = 39.5$, when we suspect that the flow is nearly laminar. A vertical cross section of the temperature structure of the flow, overlaid with vectors that show the (v, w) velocity components of the flow, is shown in the top panel of Figure 20. The bottom panel pictures a horizontal snapshot of the flow with contours of the vertical

velocity, w , and vectors that show the (u, v) velocity components. All the velocity components have been nondimensionalized by the geostrophic wind, G , and the distances x , y , and z have been nondimensionalized by the Ekman depth, D . The flow is smooth and laminar and there is no sign of turbulence.

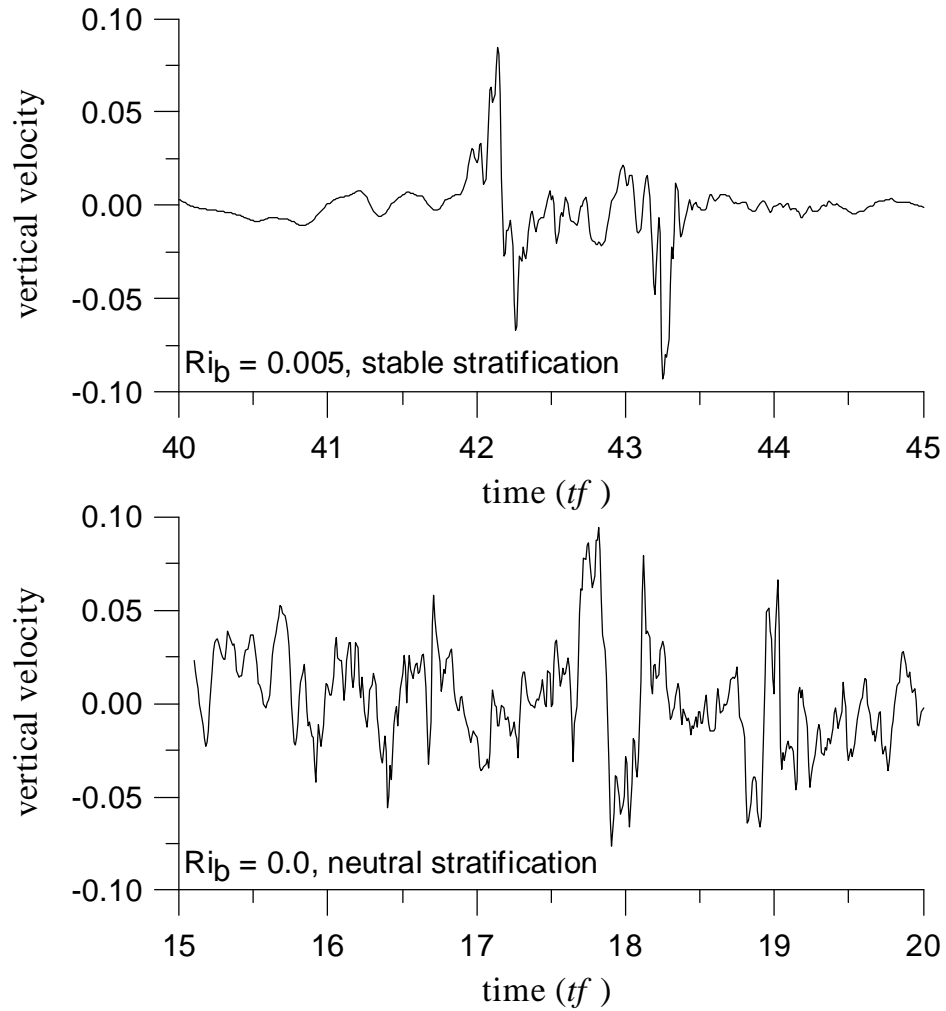


Figure 19: The upper panel shows the vertical velocity measured at a height of $z/D = 0.751$ in

a stably stratified flow while the bottom panel shows the vertical velocity, measured at the same height, in a neutrally stratified flow.

We next show a series of figures serving as an animation that illustrates the flow evolution from the laminar state through the development of sporadic turbulence. This series of five figures starts at Figure 21 and continues through Figure 26; in sequential order the times associated with these figures are $tf = 40.0, 40.5, 41.0, 41.75, 42.0, 42.1$. (Note that increment in time is 0.5 except for the sequence 41.0, 41.75, 42.0; also, the last time is 42.1). These figure show a chain of events:

- (1) the flow remains laminar at $tf = 40.0$ and $tf = 40.5$, but there is evidence of some flow organization as seen by the development of roll structures oriented about 20° to the left of the geostrophic wind (oriented along the x -axis). These roll structures are particularly apparent when looking down on the flow from above; this downward view composes the bottom panels of Figures 21 and 22. The magnitude of the vertical velocity during these times is on the order of 0.01. Relatively speaking, this velocity magnitude is quite low.
- (2) Figures 22 and 23, for times $tf = 40.5$ and $tf = 41.0$, respectively, show the development of a “wave” in the temperature structure. The initial stages of this wave are evident in the lower part of the modeling domain at about $y = 23$ in Figure 22. As time marches forward the wave increases in amplitude. Figure 23 ($tf = 41.0$) shows the buildup of the wave and its translation in the negative y direction. The wave is now positioned at about $y = 10$ (see top panel of Figure 23). The bottom panel of this figure indicates that the roll structures are aligning themselves along the geostrophic wind and that the vertical velocity has increased further; the maximum magnitude of these velocities is now on the order of 0.05.

- (3) At time $tf = 41.75$, the wave structure is well-developed and markedly visible - you just can't miss it in the top panel of Figure 24. The velocity vectors in this figure reveal the development of a strong vortex (or roll cell; we use these terms interchangeably.) Figure 24 also shows that the axis of the roll cell is aligned almost precisely along the geostrophic wind and that the vertical velocities have further increased in magnitude; they are now on the order 0.10. The irregular nature of the roll cell is illustrated by the distribution of the vertical velocity. Contours of this velocity do not line up exactly parallel to the roll's longitudinal axis as would be the case for a "pure" roll cell made up of a single Fourier mode (see for example, the bottom panel of Figure 32 for a picture of "regular" roll cells.) Rather the vertical velocity tends to occur in patches; for example, the largest velocities are located in a patch centered near the coordinates $x = 9$ and $y = 20$.
- (4) Of great importance is the wave's temperature structure as depicted in Figure 24. We see that the circulation of the roll cell has transported cold fluid over warmer fluid. This situation is convectively unstable.
- (5) Figures 25 and 26 show the beginning of the convective breakdown of the roll cell at about $y = 19$ and the development of a new temperature wave at about $y = 8$. The convective breakdown is a violent event that unleashes potential energy which is converted into fluid motion. These motions manifest themselves as the patchiness in the vertical velocity shown in the bottom of Figures 25 and 26. Such patchiness is confined to small areas in which the magnitude of the vertical velocity is quite high, as high as 0.23! An example of such a patch is centered at the coordinates $x = 16$ and $y = 20$ in Figure 25. These outbreaks of extremely large vertical velocities constitute intermittent turbulence. Figures 25 and 26 also show the development of another roll cell. We note for future reference that these vortices all rotate in the same

counterclockwise direction when viewed looking down the direction of the positive x -axis.

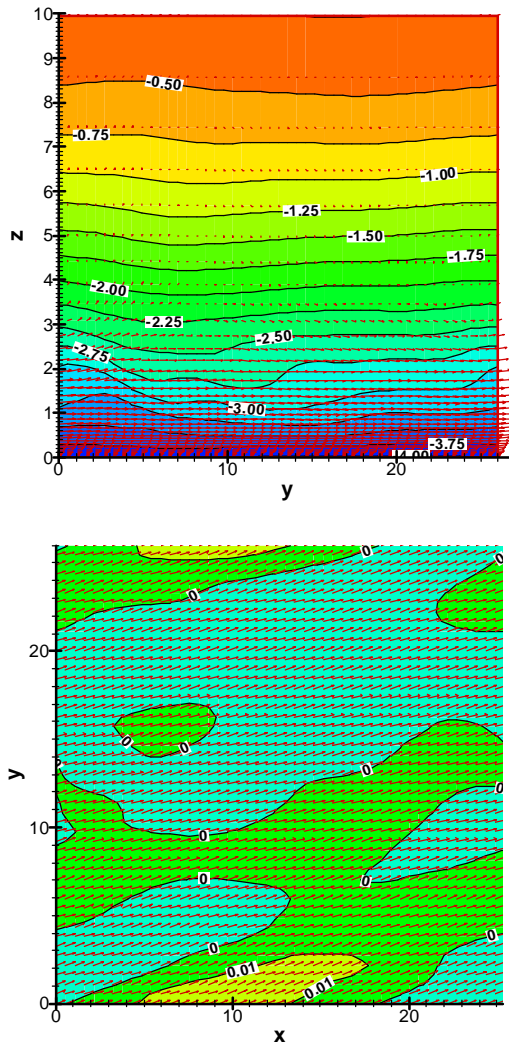


Figure 20: The top panel shows a cross section of the temperature in the y - z plane with the wind components (v, w) indicated by the vectors, $tf = 39.5$. Contours of w are shown in the bottom panel in an x - y plane at a height of

$z/D = 1.38$, and the vectors depict the wind components (u, v) .

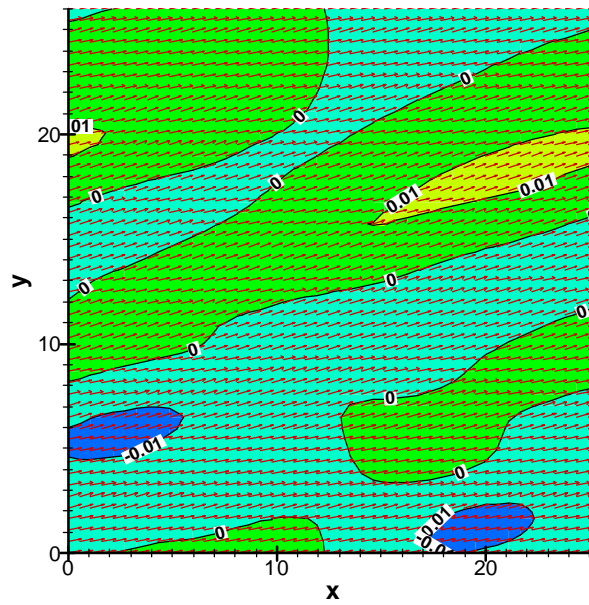
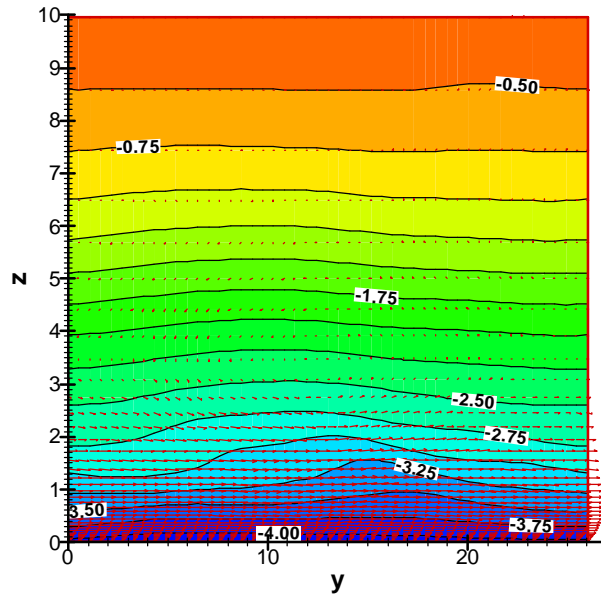


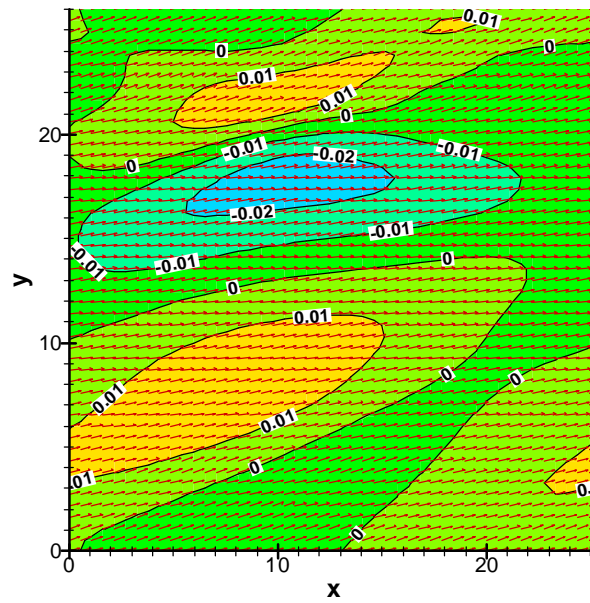
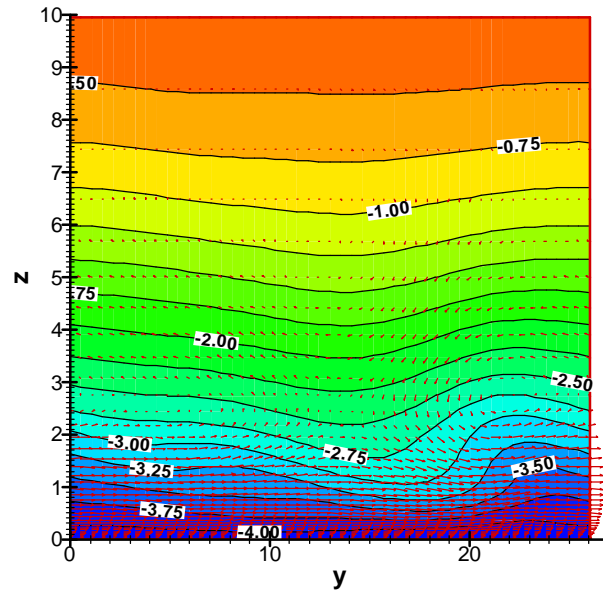
Figure 21: Same as Figure 20, but $tf = 40.0$ 

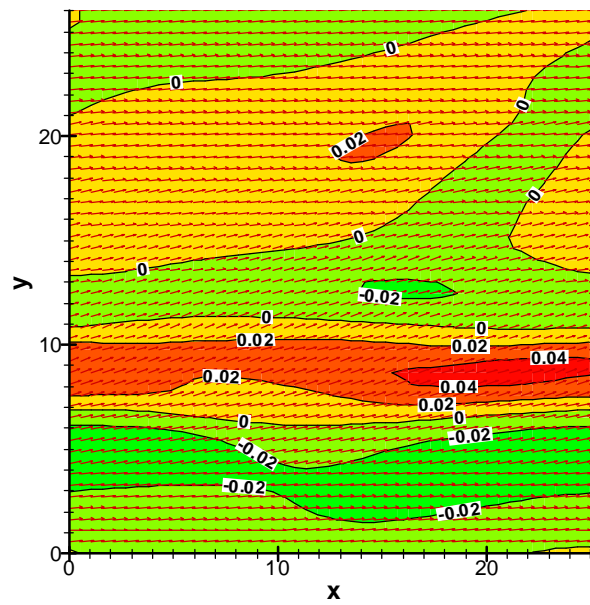
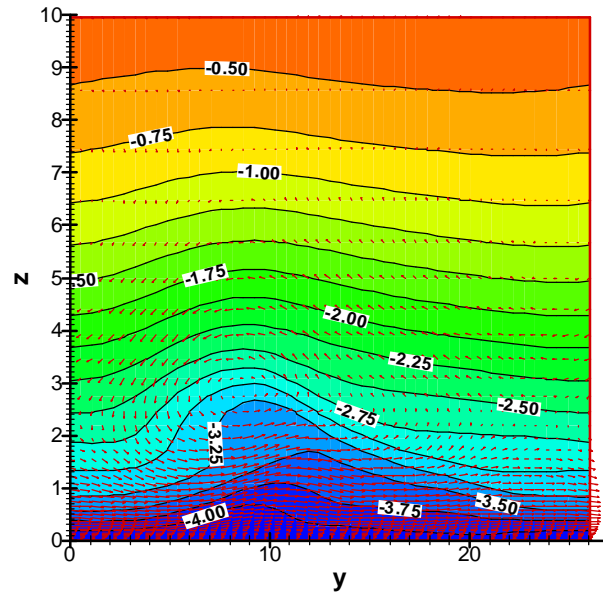
Figure 22: Same as Figure 20, but $tf = 40.50$ 

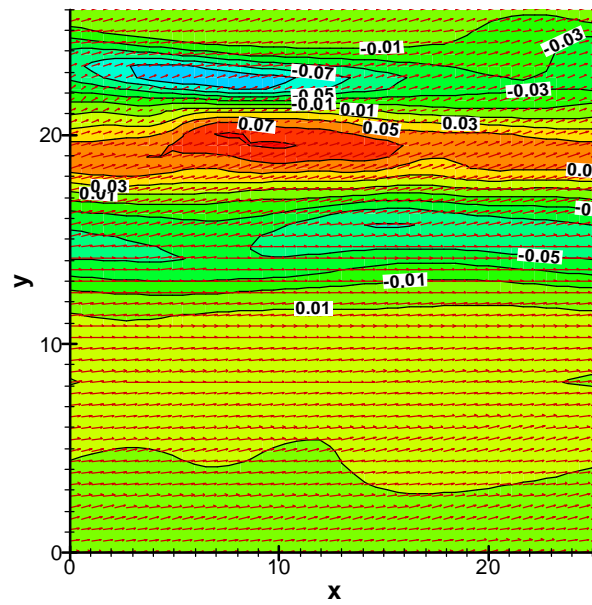
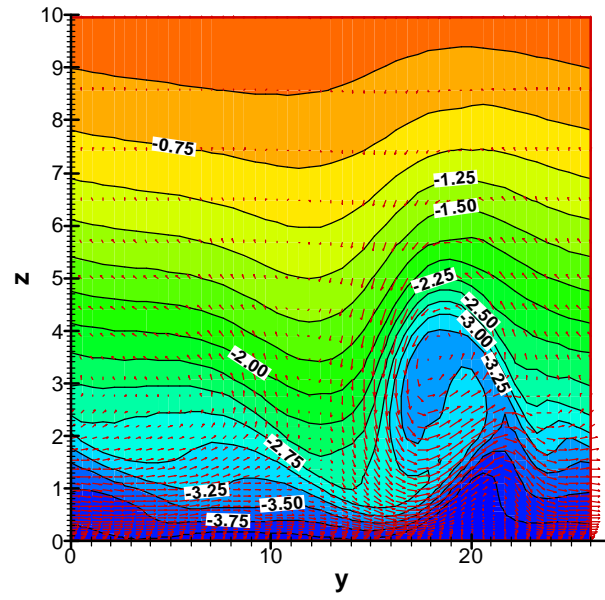
Figure 23: Same as Figure 20, but $tf = 41.0$ 

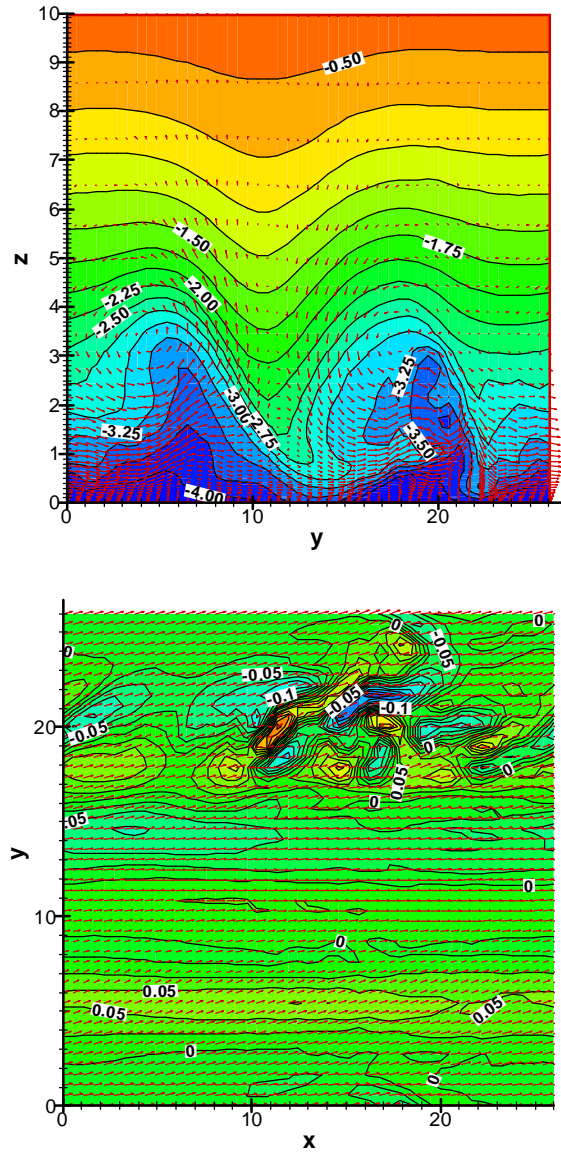
Figure 24: Same as Figure 20, but $tf = 41.75$ 

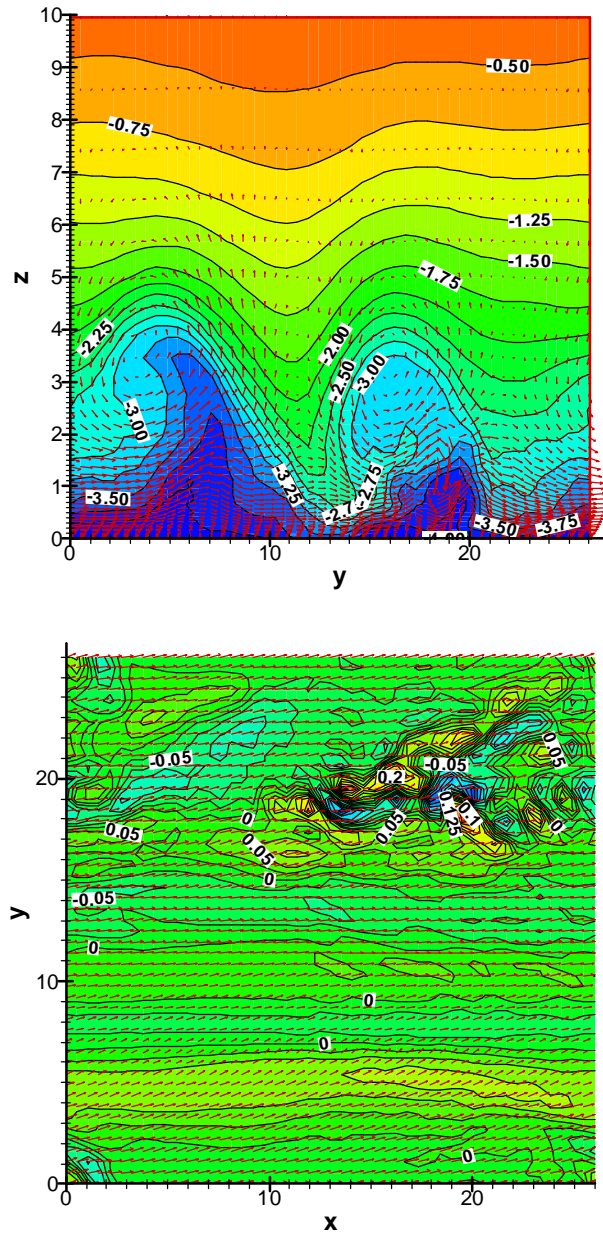
Figure 25: Same as Figure 20, but $tf = 42.0$ 

Figure 26: Same as Figure 20, but $tf = 42.1$

- (6) The final stage of the intermittence mechanism occurs when the first roll cell begins to decay. This disintegration is shown in Figure 27 in which the disintegrating roll cell is found above a position of about $y = 13$. Because the cell is decaying it can no longer lift cold air over warm air and a new convective instability will not occur. Thus, the source of the turbulence is choked off and the turbulence that comes from this particular roll vortex dies away through viscous dissipation.

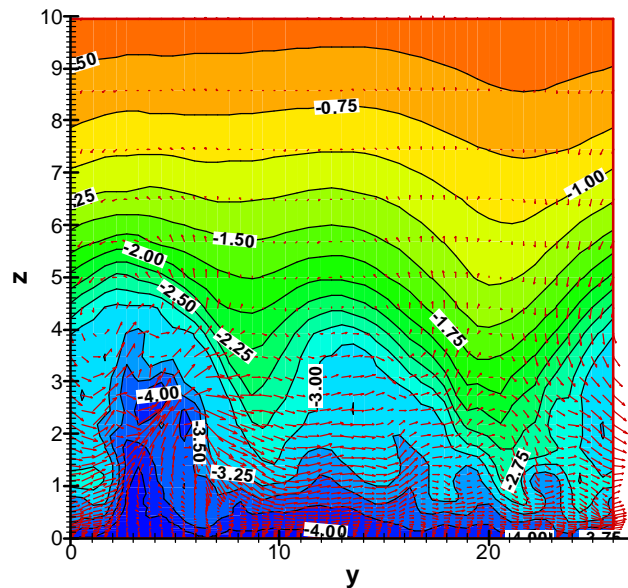


Figure 27: Vertical cross section of the flow, $tf = 42.5$. The roll cell responsible for the patchy

turbulence seen in the previous figures, positioned above $y = 13$, is beginning its decay.

Mean Flow Visualization

The steps described above follow the flow from a smooth, laminar state through the development of small but intense patches of turbulence. The description thus far has examined details of the flow, but the picture is not complete without looking at the mean flow. In particular, we examine profiles of the u and v as functions of time in Figure 28. The point of this figure is to show the time evolution of the mean flow with special emphasis on the times $tf = 39.5$ and $tf = 43.0$. These profiles are denoted by the thick black lines and the thick pink line (with pattern: — ---). At the beginning of our case study, $tf = 39.5$, there is a well-developed nocturnal jet at height $z/D = 3$ with u -component speed of about 1.13. This speed is considerably in excess of the u -component speed (slightly greater than 1.0) found in neutrally stratified flow at this height. As time progresses, the nose of this profile is considerably eroded as indicated by the profile for $tf = 43$ (the pink line). Some or most of this erosion could be attributed to an inertial oscillation as will be discussed below.

The v -component of the mean speed is shown in the bottom panel of Figure 28. Perhaps the most notable feature of this plot is the strong nocturnal jet that develops at a height of $z/D = 4$. This jet is particularly marked at time, $tf = 41.0$ (green broken line). If we assume that this is a manifestation of an inertial oscillation in the jet (Blackadar, 1957), and if we assume that the jet is aligned along the geostrophic wind at $tf = 39.5$, then the rotation of the jet through $1/4$ inertial period should occur in a time interval of $\Delta tf = 2\pi/4 \approx 1.6$. Thus the peak in the v -component of the jet should occur at a time of about 41.0 and it should be pointed perpendicularly to the right of the geostrophic wind, along the negative y -axis. From Figure 28, looking at the green line

for time $tf = 41.0$, we see that this prediction is fulfilled, suggesting the presence of a strong nocturnal jet undergoing an inertial oscillation.

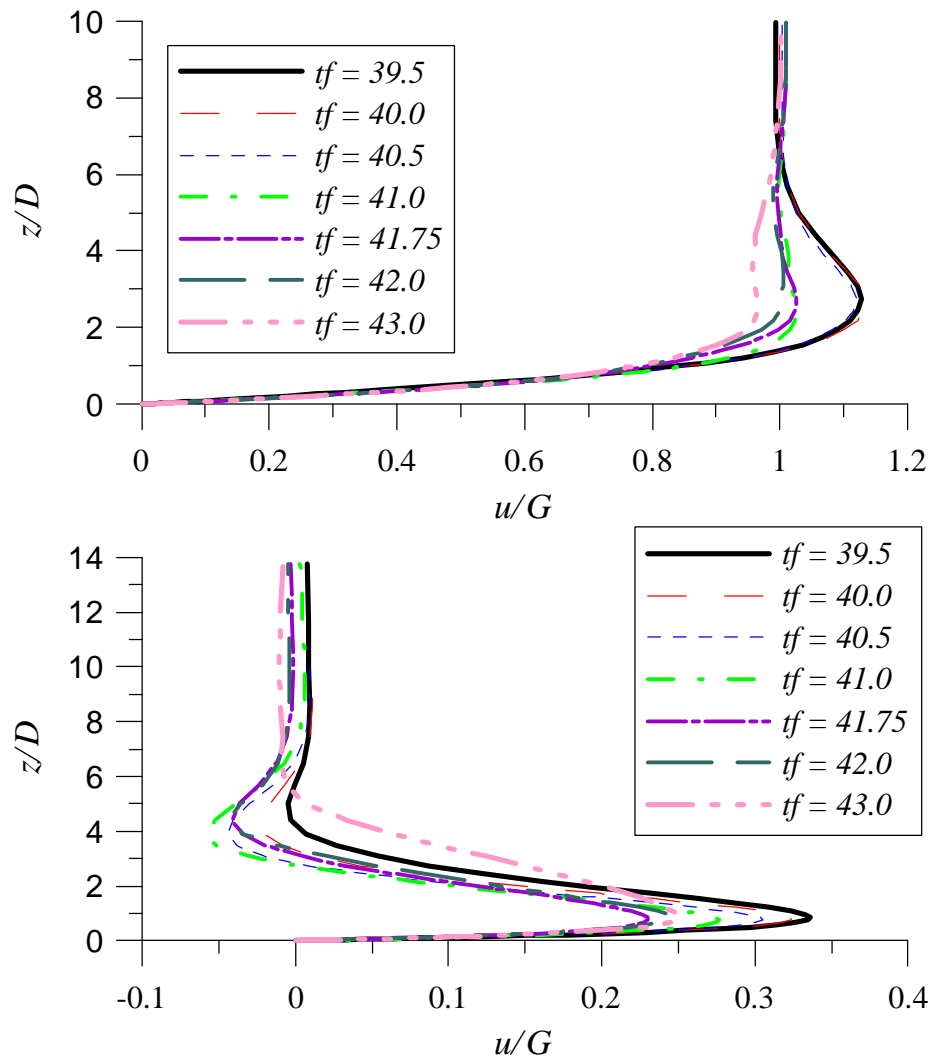


Figure 28: The top panel contains profiles of the mean flow component u while the bottom panel contains profiles of the mean flow component v .

Summary – Flow Visualization

An visual examination of the flow over a period where the flow cycles from quiescent to intermittently turbulent has revealed that the flow is indeed laminar at the start of this period. Organized, but irregular, roll vortices develop that transport cooler air over warmer air and convective instability ensues resulting in patchy turbulence. Eventually the turbulence is extinguished because the roll cell responsible for the turbulence dies away and the flow becomes laminar again. During this process a strong nocturnal jet associated with the mean flow exhibits an inertial oscillation.

3.2.2 A DETAILED EXPLORATION OF THE INTERMITTENCY MECHANISM

Through flow visualization, we have arrived at an empirical picture of the intermittency mechanism. In this section, we add rigor to this empirical picture. Specifically, we seek answers to the following questions:

- (1) Are the observed roll vortices a manifestation of an Ekman layer instability?
- (2) Why do the rolls tend to orient themselves along the geostrophic wind?
- (3) Why do the roll vortices rotate only in the counterclockwise direction (when viewed looking in the positive x direction)?
- (4) Is there some relationship between the inertial oscillation and the development of the intermittent turbulence? Would the same behavior be observed if the inertial oscillation were absent?

The first two questions may be examined as a group, subsumed under the heading of Ekman Layer Instability. Questions 3 and 4 are discussed in following subsections

entitled Counterclockwise Rotation of the Roll Vortices and Intermittency and the Inertial Oscillation.

Ekman Layer Instability

Evidence that the roll vortices stem from an Ekman layer instability modified by the inertial oscillation is very convincing. Such evidence comes from a comparison of the DNS with the results of a linear stability analysis. We were motivated to apply a linear stability analysis to the early phase of intermittency mechanism after looking at flow spectra. These spectra indicate that only a few wavenumbers in the lowest end of the wavenumber range (i.e., largest wavelengths) had appreciable energy while all other parts of a spectrum were virtually zero. Confirmation of this observation was obtained by running a modified DNS model in which the number of wavenumbers was reduced by a factor of four (from 48 to 12). For this special run, the velocity fields generated by this decimated model were identical to the fields derived from the full-sized model. Obviously, the high wavenumber components contribute nothing to the early stages of the flow and only the lowest wavenumbers are “active”.

But for the flow to be linear the amplitude of the energy associated with the active wavenumbers must be small and this requirement was observed to be in force in the early phase of the flow. The low energy values are consistent with the finding, mentioned above, that the vertical velocity levels during the initial stages of the flow evolution were quite low, being on the order of 0.01. On the other hand, spectra obtained from the turbulent phase of the flow revealed that a large number of wavenumbers had been activated and that the energy density associated with these wavenumbers was significant. In this phase of the flow, the assumption of linearity would not be justified. For the case study under consideration, we estimate that the time ranges over which linear processes dominate extends from about $tf = 39.0$ to about $tf = 41.5$. Linearity would also apply to a time period at the end of the case

study when the flow becomes laminar again. However, we will restrict our attention only to the time interval at the beginning of the flow.

Using the mean profiles of temperature, and the mean u and v velocity components obtained from the simulations at a given time, we perform a linear stability analysis to compute the growth rate, phase speed, wavenumber, and roll cell orientation angle. The wavenumber and orientation angle are varied systematically until “optimal” values of the wavenumber and orientation angle are determined at which the growth rate is maximized. At these optimal values the phase speed is also calculated. When deriving the linear stability equations used for this analysis it is necessary to add a Reynolds stress to the flow equations to achieve a balance of forces in the mean flow. For example, the mean flow equation for the u -component of the velocity is

$$\frac{\partial \bar{U}}{\partial t} = \frac{1}{\text{Ro}} \bar{V} + \frac{1}{\text{Re}} \frac{\partial^2 \bar{U}}{\partial z^2} - \frac{\partial(\overline{u'w'})}{\partial z} \quad (3.9)$$

where the overbar represents a horizontally averaged (mean) quantity. The linear stability equations are derived in the usual manner and are identical to those of the laminar Ekman layer (eqs. A.5 through A.9) except that the background velocity components and temperature profile are the mean u , v , and Θ profiles obtained from the simulations. The mean profiles of wind do not follow the traditional laminar Ekman spiral because of the modification by Reynolds stresses and by the inertial oscillation.

For time increments of $\Delta(tf) = 0.1$, we perform the stability analysis from time $tf = 39.0$ to time $tf = 41.5$ and find the maximum growth rate, the phase speed, and the values of the wavelength and orientation angle corresponding to the maximum growth rate. From the simulations, we infer the same parameters and then compare the simulation results with those from the stability analysis.

When performing this comparison, we must be mindful of several important caveats. The first of these is that the linear stability analysis is a static calculation that gives growth rates, phase speeds, etc., which are related only to the mean flow at the specific time under consideration. In this regard, the linear analysis provides an indication of the “forcing” of the flow at the present time; i.e., where growth occurs in wavenumber space and how fast growth occurs. In contrast, the simulations are dynamic and the flow structure at a particular time depends on past history. The difference between a dynamic and static calculation is easily illustrated by considering a simple example. At a particular time, t , the static, linear stability analysis shows that the growth rate is largest at the optimal wavenumber k , yet examination of the simulation at this time shows that disturbances associated with other wavenumbers have larger amplitudes. How could this be? This seeming discrepancy is easily explained. The other disturbances may be larger because of the large growth rates they possessed in the past and therefore these vortices had an opportunity to build up large amplitudes over time. Yet the roll cell with largest growth rate at time t may just be in the initial stages of growth and, with little time to develop its amplitude, it could be much smaller than the others.

The second caveat is also easily understood: the stability analysis is continuous in wavenumber space whereas the numerical construction of the DNS permits only a finite set of discrete wavenumbers to be present. This implies, among other things, that the maximum growth rates derived from the DNS must be less than or equal to those from the stability analysis. Why is this the case? Because the maximum growth rate calculated from the stability analysis will occur at a specific optimal wavenumber, k , and for all other wavenumbers the growth rate will be less than this maximum. Unless the DNS happens to have the optimal k in its discrete wavenumber set (either by coincidence or design), the maximum growth rate of any disturbance in the DNS will be less than the maximum growth rate connected with k .

A third caveat concerns the extraction of the phase speeds, etc. from the simulations. A glance at Figures 20 through 23 shows that the organized structures in the DNS, while readily discernable by eye, are not very regular and they are certainly not as regular as the sinusoidal pattern of the roll cells predicted by theory (see again the bottom panel of Figure 32 for an example of a regular roll cell). This lack of uniformity in the simulations makes the assessment of, say, a disturbance wavenumber somewhat ambiguous. Of the four parameters in which we are interested, the roll cell orientation is most easily and unambiguously determined from a visual inspection. This is not necessarily the case for the other three quantities.

To reduce this ambiguity we developed a simple way of objectively deriving the four disturbance parameters from the flow. This method begins with the horizontal Fourier transform of the w -component of the flow and then finds the three wavenumbers connected with the amplitude of the three largest Fourier components. Call these wavenumbers \mathbf{k}_1 , \mathbf{k}_2 and \mathbf{k}_3 . For a particular time, the orientation and wavelength of the disturbance of the flow is a weighted average over these three wavenumbers, where the weights are the magnitude of the Fourier transform of w . If $\bar{\mathbf{e}}_r$ is the “average” roll cell orientation for the time in question, then

$$\bar{\mathbf{e}}_r = \frac{\mathbf{e}_r^{\mathbf{k}_1} |\hat{w}_{\mathbf{k}_1}| + \mathbf{e}_r^{\mathbf{k}_2} |\hat{w}_{\mathbf{k}_2}| + \mathbf{e}_r^{\mathbf{k}_3} |\hat{w}_{\mathbf{k}_3}|}{|\hat{w}_{\mathbf{k}_1}| + |\hat{w}_{\mathbf{k}_2}| + |\hat{w}_{\mathbf{k}_3}|} \quad (3.10)$$

In this equation $|\hat{w}_{\mathbf{k}}|$ is the magnitude of the Fourier transform at wavenumber \mathbf{k} and $\mathbf{e}_r^{\mathbf{k}}$ is the angle that the longitudinal axis of the roll cell makes with the geostrophic wind. The verisimilitude of this formula was assessed by comparing angles calculated using eq. 3.10 with angles estimated from a visual inspection of the flow field. This evaluation indicated that our objective method works reasonably well. The same formula can be applied to find the average wavenumber, \mathbf{a} , of the growing

disturbances by substituting the magnitude of the wavenumber for orientation angle in this manner,

$$\mathbf{a} = \frac{|\mathbf{k}_1| |\hat{w}_{k_1}| + |\mathbf{k}_2| |\hat{w}_{k_2}| + |\mathbf{k}_3| |\hat{w}_{k_3}|}{|\hat{w}_{k_1}| + |\hat{w}_{k_2}| + |\hat{w}_{k_3}|} \quad (3.11)$$

Diagnosing growth rates and phase speeds from the simulations is slightly more complicated. To obtain these variables, we resort to the following device. Assume that the w -component of the velocity field can be represented by a sum over all Fourier disturbances with complex frequency $\mathbf{w}_k = \text{Re}[\mathbf{w}_k] + i \cdot \text{Im}[\mathbf{w}_k]$,

$$w(x, y, z, t) = \sum_{\mathbf{k}} \hat{w}_{\mathbf{k}}(z) e^{-i\mathbf{w}_{\mathbf{k}} t} e^{i\mathbf{k} \cdot \mathbf{x}} \quad (3.12)$$

After time Δt the expression for the disturbances is

$$w(x, y, z, t) = \sum_{\mathbf{k}} \hat{w}_{\mathbf{k}}(z) e^{-i\mathbf{w}_{\mathbf{k}}(t+\Delta t)} e^{i\mathbf{k} \cdot \mathbf{x}} = \sum_{\mathbf{k}} \hat{w}'_{\mathbf{k}}(z, t + \Delta t) e^{i\mathbf{k} \cdot \mathbf{x}} \quad (3.13)$$

where $\hat{w}'_{\mathbf{k}}(z, t + \Delta t) = \hat{w}_{\mathbf{k}}(z) e^{-i\mathbf{w}_{\mathbf{k}}(t+\Delta t)}$. Focusing on one wavenumber at a time, we can determine the growth rate and phase speeds from the simple numerical formulae

$$\text{growth rate}|_{\mathbf{k}}^{t+\Delta t/2} \approx \text{Re}\left[\frac{1}{\Delta t} \text{Log}(\hat{w}'_{\mathbf{k}}(z, t + \Delta t))\right] \quad (3.14)$$

$$\text{phase speed}|_{\mathbf{k}}^{t+\Delta t/2} \approx -\frac{1}{|\mathbf{k}|} \text{Im}\left[\frac{1}{\Delta t} \text{Log}(\hat{w}'_{\mathbf{k}}(z, t + \Delta t))\right] \quad (3.15)$$

To find an averaged growth rate (or phase speed), we calculate, in an analogous manner to the eq. 3.10, the weighted average using growth rates (or phase speeds) associated with the three largest Fourier coefficients. It was possible to check the skill of the growth rate equation, eq. 3.14, by finding a time series of the maximum vertical

velocity in a specified horizontal plane, $w_{max}(t)$, and then differentiating. The growth rate of the disturbances is approximately $\frac{1}{w_{max}} \frac{dw_{max}}{dt}$. The rates derived from this simple formula are comfortingly similar to rates from eq. 3.14, thus suggesting that this equation is at least approximately correct.

Armed with the set of the four parameters calculated from the simulations, and another set derived from theory, it is possible to appraise how well the simulations follow the theory. This comparison is shown in Figure 29 in which the results from the linear stability analysis and the simulations are shown as lines and black dots, respectively. The parameters originating from the simulations are taken from a field of the vertical velocity, w , in a horizontal plane at a height of $z/D = 2.19$ -- a height where the roll cell structure is well developed. The comparison between the two roll cell orientation angles is pictured in the top panel of this figure. This variable is most easily visualized in the simulations and, considering the caveats expressed above, the agreement between the theory and simulations is surprisingly good. Certainly the trends in time agree very well.

This panel illustrates one of the caveats expressed above: that the simulations are performed in discrete wavenumber space while the linear stability theory is continuous in this space. For times greater than about $tf = 41.0$, the roll cells in the simulations orient themselves exactly parallel to the geostrophic wind (x -axis). This exact orientation is probably due to the fact that the wavenumbers that represent the roll cells must “project” into the discrete wavenumber space inherent to any spectral simulation. For small orientation angles -- close to zero but not exactly equal to zero -- the best possible projection that can occur is along the k_y -axis since other projections would only be appropriate for much larger orientation angles. Projection of the wavenumber onto this axis results in roll cell axis orientations exactly parallel to the x -axis.

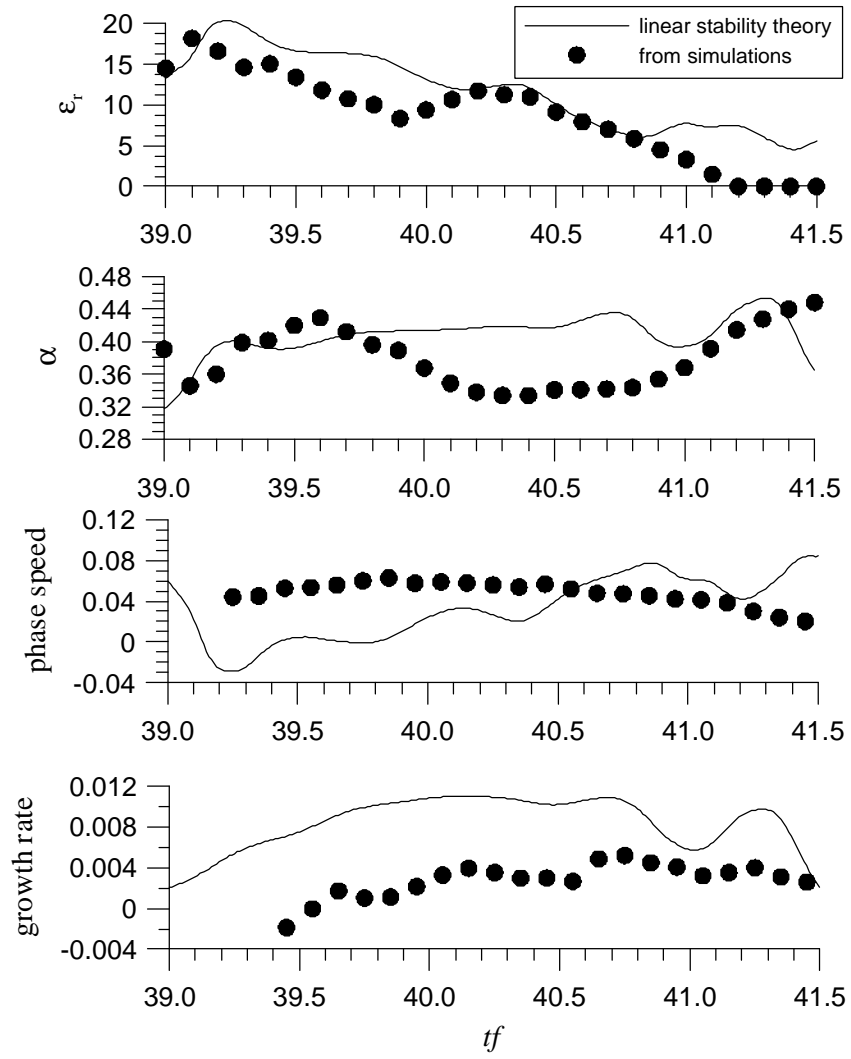


Figure 29: Comparison between four variables derived from linear stability theory (lines) and from the simulations (black dots). The variables are the roll cell orientation, \mathbf{e}_r ; the roll cell wavenumber, $\mathbf{a} = 2\mathbf{p}/\mathbf{l}$, where \mathbf{l} is the roll cell's wavelength; the phase speed, and the growth rate.

Focusing now on the second panel from the top in Figure 28, we see that, as expected, the agreement between the two roll cell wavenumbers is not as good as the agreement obtained for the orientation angles. Still, the agreement is reasonably good given the caveats expressed above. Again we must reemphasize the irregular nature of the roll cells that arise in simulations. These cells are not the roll cells of theory that possess a perfectly uniform sinusoidal pattern in a horizontal direction lateral to the roll cell axis. The absence of perfect regularity makes the precise determination of a roll cell wavenumber somewhat problematic.

Phase speeds and growth rates are pictured in the bottom two panels of Figure 29. (These quantities have been nondimensionalized using the time scale most often used for the Ekman linear stability analysis, D/G , and not the inertial time scale, $1/f$. The ratio of the two scales is $1/f \div D/G = G/fD = \text{Ro} = 200$.) As expected, the growth rates derived from the simulations are less than the theoretical growth rates but the trends show reasonable agreement. The magnitudes of the phase speeds exhibit approximate but not perfect conformity with one another. Intuitively speaking, we guess that the phase speed would be the most difficult variable to extract from the simulations given the irregular shape and meandering orientation of the roll cells.

Taken together, the plots in Figure 29 strongly suggest that the initial part of the intermittency mechanism is a linear response of the flow to an Ekman-type forcing that

gives birth to organized flow structures that resemble roll vortices. This forcing is completely analogous to the forcing that arises from linear Ekman layer stability analysis in which energy is transferred from the mean flow to perturbations with positive growth rates. Unlike the traditional Ekman forcing, however, the mean, background velocity is not steady but rather changes in time in a manner of an inertial oscillation. The time variation of the mean flow is reflected in the changing nature of the flow structures that gradually orient themselves along the x -axis and possess accelerating growth rates.

The case that the flow is responding to an “Ekman forcing”¹³ can be made even stronger by demonstrating mathematically that the only forcing available to the flow in the linear phase is an Ekman forcing. This demonstration starts with the governing equations for the computational variables (i.e., perturbations from the background flow) with the non-linear terms dropped and in which the computational variables have been transformed to Fourier space and cast into \parallel and \perp modes. By deleting the non-linear terms from eqs. (2.39 – 2.42), we have

$$\begin{aligned} \frac{\partial \hat{u}_{\mathbf{k}}^{\square}}{\partial t} = & \\ & i \frac{2\mathbf{p}}{L} |\mathbf{k}| \hat{p}_{\mathbf{k}} + \frac{1}{\text{Re}} \left(\frac{\partial^2}{\partial z^2} - \left(\frac{2\mathbf{p} |\mathbf{k}|}{L} \right)^2 \right) \hat{u}_{\mathbf{k}}^{\square} + \frac{1}{\text{Ro}} \hat{u}_{\mathbf{k}}^{\perp} \\ & + \left(i \frac{2\mathbf{p} |\mathbf{k}| U_{BS}^{\square}}{L} \hat{u}_{\mathbf{k}}^{\square} - \hat{w}_{\mathbf{k}} \frac{dU_{BS}^{\square}}{dz} \right) \end{aligned} \quad (3.16)$$

¹³ We use the term Ekman forcing loosely to mean forcing associated with mean flow profiles that are “Ekman like”. These profiles would include profiles from the laminar Ekman layer, as well as profiles from turbulent Ekman layers.

$$\begin{aligned} \frac{\partial \hat{u}_k^\perp}{\partial t} = & \\ \frac{1}{\text{Re}} \left(\frac{\partial^2}{\partial z^2} - \left(\frac{2\mathbf{p}|\mathbf{k}|}{L} \right)^2 \right) \hat{u}_k^\perp - \frac{1}{\text{Ro}} \hat{u}_k^\square + \left(i \frac{2\mathbf{p}|\mathbf{k}|U_{BS}^\square}{L} \hat{u}_k^\perp - \hat{w}_k \frac{dU_{BS}^\perp}{dz} \right) \end{aligned} \quad (3.17)$$

$$\begin{aligned} \frac{\partial \hat{w}_k}{\partial t} = & \\ -\frac{\partial \hat{p}_k}{\partial z} + \frac{1}{\text{Re}} \left(\frac{\partial^2}{\partial z^2} - \left(\frac{2\mathbf{p}|\mathbf{k}|}{L} \right)^2 \right) \hat{w}_k + \text{Ri}_b \hat{\Theta}_k + i \frac{2\mathbf{p}|\mathbf{k}|U_{BS}^\square}{L} \hat{w}_k \end{aligned} \quad (3.18)$$

$$\begin{aligned} \frac{\partial \hat{\Theta}_k}{\partial t} = & \\ -\hat{w}_k \frac{\partial \Theta_d}{\partial z} + \frac{1}{\text{RePr}} \left(\frac{\partial^2}{\partial z^2} - \left(\frac{2\mathbf{p}|\mathbf{k}|}{L} \right)^2 \right) \hat{\Theta}_k + i \frac{2\mathbf{p}|\mathbf{k}|U_{BS}^\square}{L} \hat{\Theta}_k \end{aligned} \quad (3.19)$$

These equations can be discretized in the z -direction using the Galerkin method described in Chapter 2. (For the sake of brevity we omit a recapitulation of the details). If \mathbf{a}_k is a column vector consisting of the expansion coefficients (\mathbf{a}_k^\square , \mathbf{a}_k^\perp , \mathbf{a}_k^Θ) of the computational variables, then the discretized linear equations may be written in vector- matrix form as

$$\frac{d\mathbf{a}_k}{dt} = \mathbf{A}_k \mathbf{a}_k \quad (3.20)$$

where \mathbf{A}_k is a square matrix, the elements of which depend upon the background velocity profiles at a time t_0 . The solution to this linear equation at a time $t_0 + \Delta t$ is

$$\mathbf{a}_k(t_0 + \Delta t) = \mathbf{S} e^{2t_0} \mathbf{S}^{-1} \mathbf{a}_k(t_0) \quad (3.21)$$

where \mathbf{I} is a diagonal matrix consisting of the eigenvalues of \mathbf{A}_k , and \mathbf{S} is a matrix whose columns are the eigenvectors of \mathbf{A}_k . If we assume that the background velocity profiles at time t_0 are the mean profiles from the simulation at this particular time, an estimate of the expansion coefficients for the perturbation quantities (roll cells) at time $t_0 + \Delta t$ is given by eq. 3.21. The eigenvalues of the matrix \mathbf{A}_k govern which eigenmodes -- the columns of the matrix \mathbf{S} -- grow or decay over the time interval Δt . But these eigenvalues are exactly the eigenvalues¹⁴ obtained from a linear stability analysis of the Ekman layer. With this realization we see that over the increment of time, Δt , the flow modes that receive the largest boost are simply the fastest growing Ekman modes and that no other forcing is operative. This conclusion, of course, would not hold once the flow becomes non-linear.

Counterclockwise Rotation of the Roll Vortices

An additional aspect of the proposed intermittency mechanism that demands an explanation is the observation that the roll vortices only rotate in the counterclockwise direction, when viewed looking along the positive x -axis. The single direction of the rotation is evident in the upper panel of Figure 30 which is a snapshot of the flow in the y - z plane taken at time $tf = 42.1$. The (v, w) velocity field is depicted by the vectors and the black lines are approximate, computer-generated streamlines. A glance at the field unmistakably shows the two “closed cell” roll cells centered at the coordinates $x = 3.5, y = 3.5$ and $x = 16, y = 3.5$. There is no evidence of vortex rotation in the clockwise direction.

We inquire why the vortices rotate in only one direction, particularly when Ekman roll cells tend to come in counterrotating pairs (for example, see Figure 10 in Brown,

¹⁴ The relationship between λ and the eigenvalues of a linear stability analysis, \mathbf{w} , is:

$$\lambda = i \mathbf{w}, \text{ where } i = -\sqrt{-1}.$$

1972). The answer is very simple and can be immediately grasped by considering the difference between the flow consisting of Ekman perturbations only and the total flow consisting of the perturbations and the mean background flow. Both these flows are depicted in Figure 30. In this figure the top panel is the total flow where the vortices rotate in only the counterclockwise direction. The bottom panel is the perturbation flow; that is, the total flow from which the mean, background flow has been subtracted. (We kindly remind the reader that the mean flow in the y - z plane is shown in the bottom panel of Figure 28). In the perturbed flow only a roll cell pair is evident in which one roll of the pair, centered at the coordinates $(x = 3.5, y = 3.5)$ and is rotating in the opposite direction than the other roll, centered at $(x = 3.0, y = 11.5)$.
The

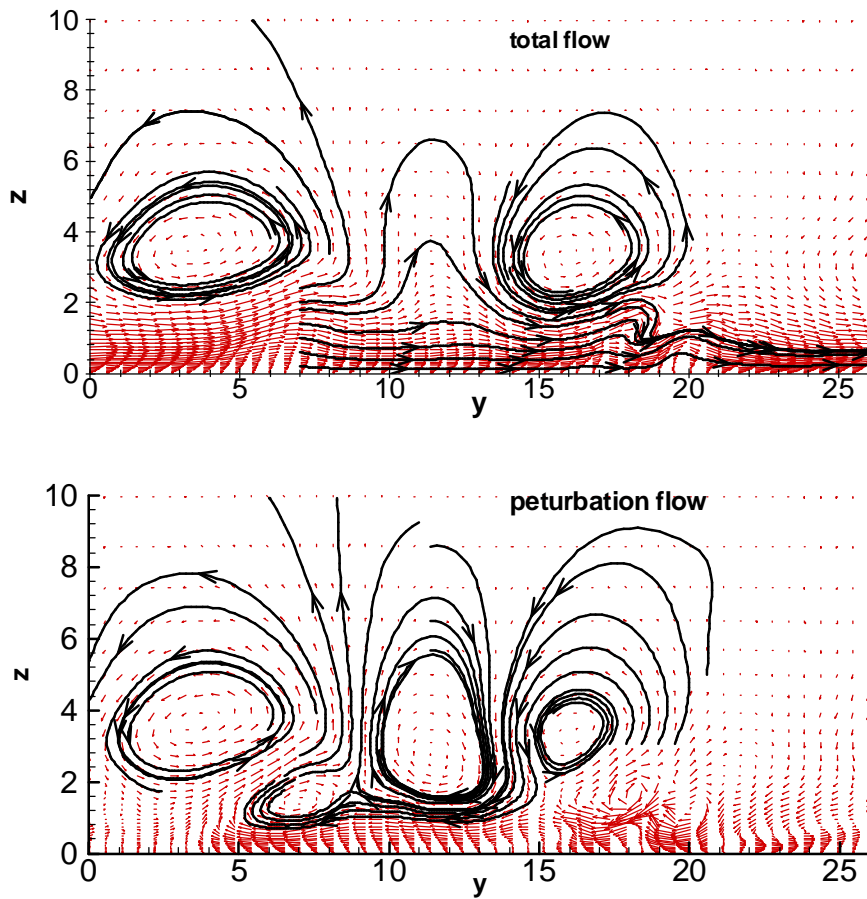


Figure 30: Cross sections of the flow in the y, z plane at time $tf = 42.10$. The vectors show the v, w components of the flow and the black lines are approximate representation of the flow streamlines. The upper panel is the total flow (mean + perturbation) while the bottom panel is the perturbation flow

streamlines of this cell, rotating clockwise, form a pattern that is quite similar to the Ekman perturbations found by Brown (1972).

Apparently, the absence of counterrotating vortices in the full flow stems merely from the effect of adding the mean flow to the perturbation flow. The mean flow in the vertical range $z/D \approx 1$ to $z/D \approx 4$ possesses considerable positive vorticity ($-\partial v/\partial z \approx -\Delta v/\Delta z = 0.3/2 = 0.15$) aligned along the positive x -axis. On the other hand, the roll cell centered at $(x = 3.0, y = 11.5)$ -- the cell with clockwise rotation -- has a negative vorticity of about $-\partial v/\partial z \approx -\Delta v/\Delta z = -(0.03 - (-0.2))/(4.41 - 1.08) = -0.07$ over the vertical range of interest. When the two vorticities are added to find the total flow vorticity, the negative vorticity (clockwise rotation) is completely swamped and canceled by the positive vorticity of the mean flow. Therefore clockwise rotation of the organized structures does not show up in the total flow.

Intermittency and the Inertial Oscillation

In this section we further examine the role that the inertial oscillation plays in the development of intermittent turbulence. We have already seen that the inertial oscillation influences the time development of the roll cell perturbations during the linear phase of the intermittency mechanism. But we wonder if the oscillation might have an even stronger role; for example, would the intermittence occur in the absence of an oscillation?

We cannot answer this question unequivocally, but additional numerical tests suggest that the answer “no”. The intermittency mechanism needs the inertial oscillation to exist! A test simulation (called “TS” for short) from which this conclusion is drawn uses, as its initial condition for temperature, the diffusive temperature profile occurring at the beginning of the case study examined above (i.e., at time $tf = 39.0$). We then effectively erase the inertial oscillation in the velocity initial condition by setting the

mean flow profiles equal to the profiles of the laminar Ekman layer, and we replace the perturbation field existing in the original simulation with low-amplitude, Gaussian deviates. At the start of the test simulation, the flow is therefore just a laminar Ekman layer with the diffusive temperature appropriate for the beginning of our case study.

The DNS is started and run for a time of about $tf = 20.0$. Although roll cells develop (see below) intermittency is NOT observed! This test cannot fully put to rest the issue of whether the inertial oscillation is essential for the existence of the intermittency mechanism described above, but the results are strongly suggestive that it is. For the sake of comparison, we show in Figure 31 the surface friction velocity, u_* / G , and the angle that the surface stress makes with the geostrophic wind, \mathbf{b} , from the test run. To facilitate the comparison between this test run and the previous simulations these parameters are plotted on the same scale as shown in Figures 11 and 12. That these parameters scarcely deviate from their laminar values indicates that the flow remains laminar throughout the duration of the simulation. Also, there is little evidence of any appreciable effect on the mean flow. It, too, remains nearly fixed in a laminar-like state.

Figure 32 shows the flow structure of the vertical velocity at time $tf = 3.0$. The existence of regular Ekman-like roll cell is unmistakable. In contrast to the roll cell structures of the simulations in which the inertial oscillation is present, the cells in the TS runs are very uniform and characterized by very low vertical velocities with magnitudes on the order of 0.01 or less. Obviously, the difference between the flow with and without the inertial oscillation is very marked. The comparison of the flow evolution, with and without the presence of the inertial oscillation, suggests that, when the oscillation is present, energy is extracted from the mean flow and transferred to the smaller scales in a very effective manner. This energy transfer is easily explored by

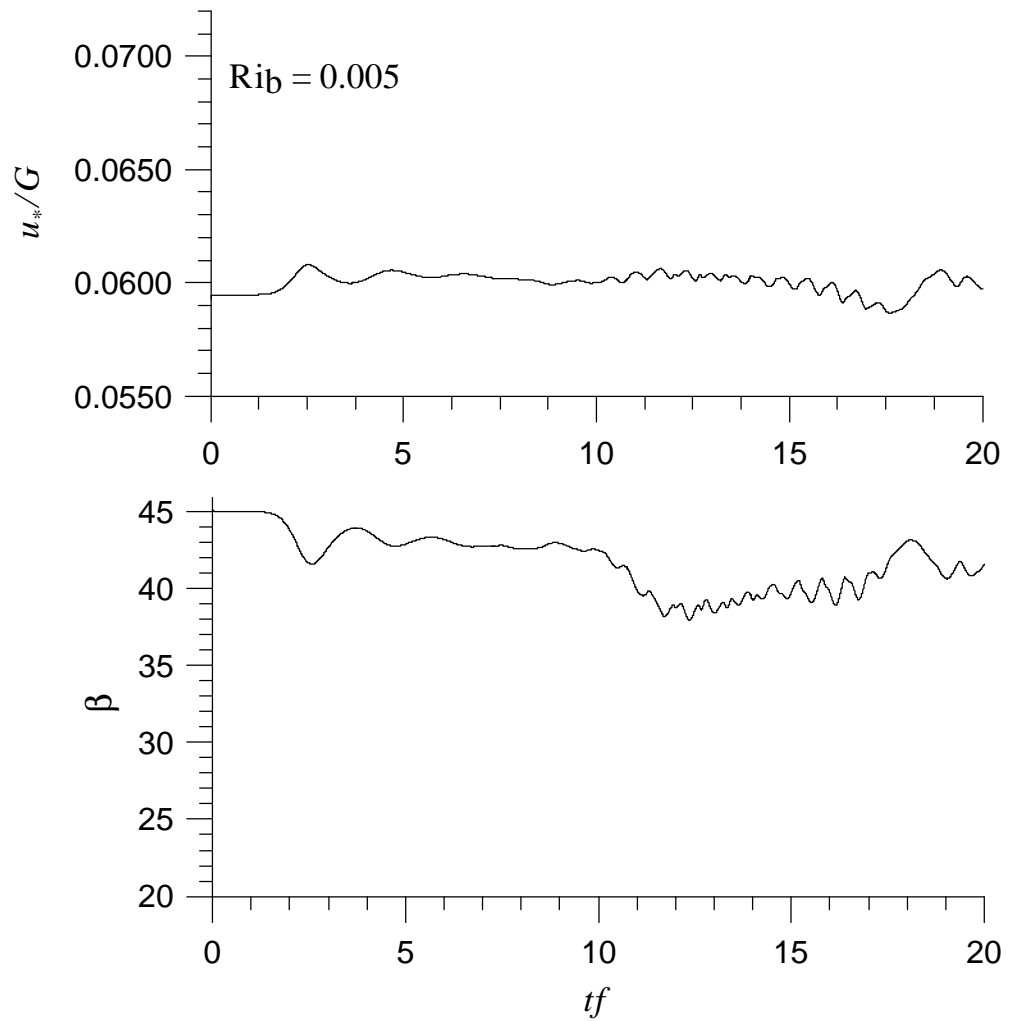


Figure 31: Surface friction velocity, u_*/G , and the angle that the surface stress makes with the geostrophic wind, β , for the test simulation in which the inertial oscillation is erased.

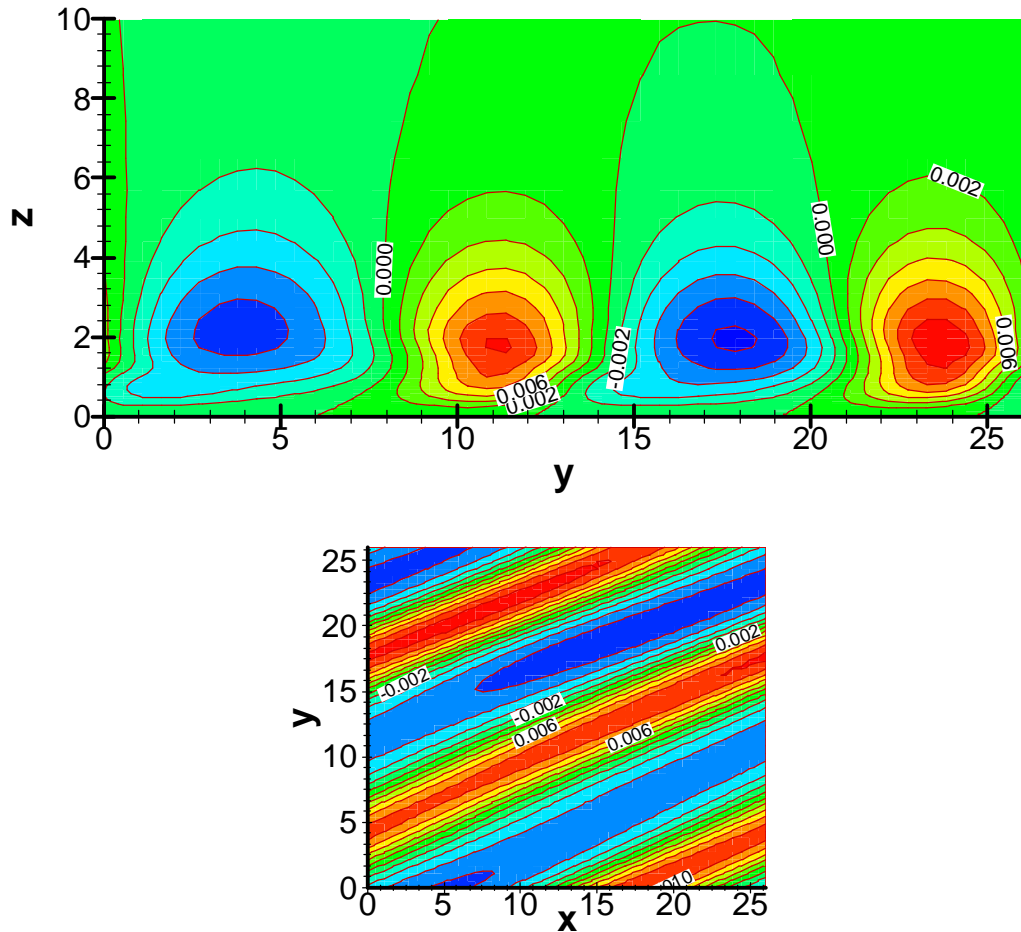


Figure 32: Vertical velocity contours for the TS runs (inertial oscillation removed). The top panel shows the vertical velocity, w , contoured in the y - z plane and the bottom panel shows w contoured in the x - y plane. Note the regular structure of these cells.

looking at the mean flow energetics as embodied in the mechanical energy equation integrated through the depth of the atmosphere:

$$\begin{aligned} \frac{d}{dt} \int_0^{\infty} \frac{(\bar{U}^2 + \bar{V}^2)}{2} dz = \\ \frac{1}{\text{Ro}} \int_0^{\infty} \bar{V} dz - \frac{1}{\text{Re}} \int_0^{\infty} \left(\left(\frac{\partial \bar{U}}{\partial z} \right)^2 + \left(\frac{\partial \bar{V}}{\partial z} \right)^2 \right) dz + \int_0^{\infty} (\overline{u'w'} \frac{\partial \bar{U}}{\partial z} + \overline{v'w'} \frac{\partial \bar{V}}{\partial z}) dz \end{aligned} \quad (3.22)$$

where \bar{U} and \bar{V} are the mean velocity components and the overbar indicates an average over a horizontal plane. The terms in eq. 3.22 are, proceeding from right to left, the rate of change of the mean kinetic energy, the production of kinetic energy from the interaction of the mean flow with the ambient horizontal pressure gradient, molecular dissipation, and the transfer of energy between the mean flow and other scales.

These terms are easily computed from the simulations, and we show them in Figure 33 (with some modification) for the simulations with and without the inertial oscillation, for a time period of about one inertial period ($tf = 2\pi$). In this figure the production and dissipation terms have been lumped together so that a single term, production minus dissipation, is shown. All the terms have been integrated in time. For example, if $T(t)$ is the *rate* of transfer of kinetic energy to the smaller scales – the last term in eq. 3.22, then what we show in Figure 33 is

$$\int_0^t T(t') dt' \quad (3.23)$$

This time integration indicates the total amount of energy that has been interchanged between the mean flow and the smaller scales at time t .

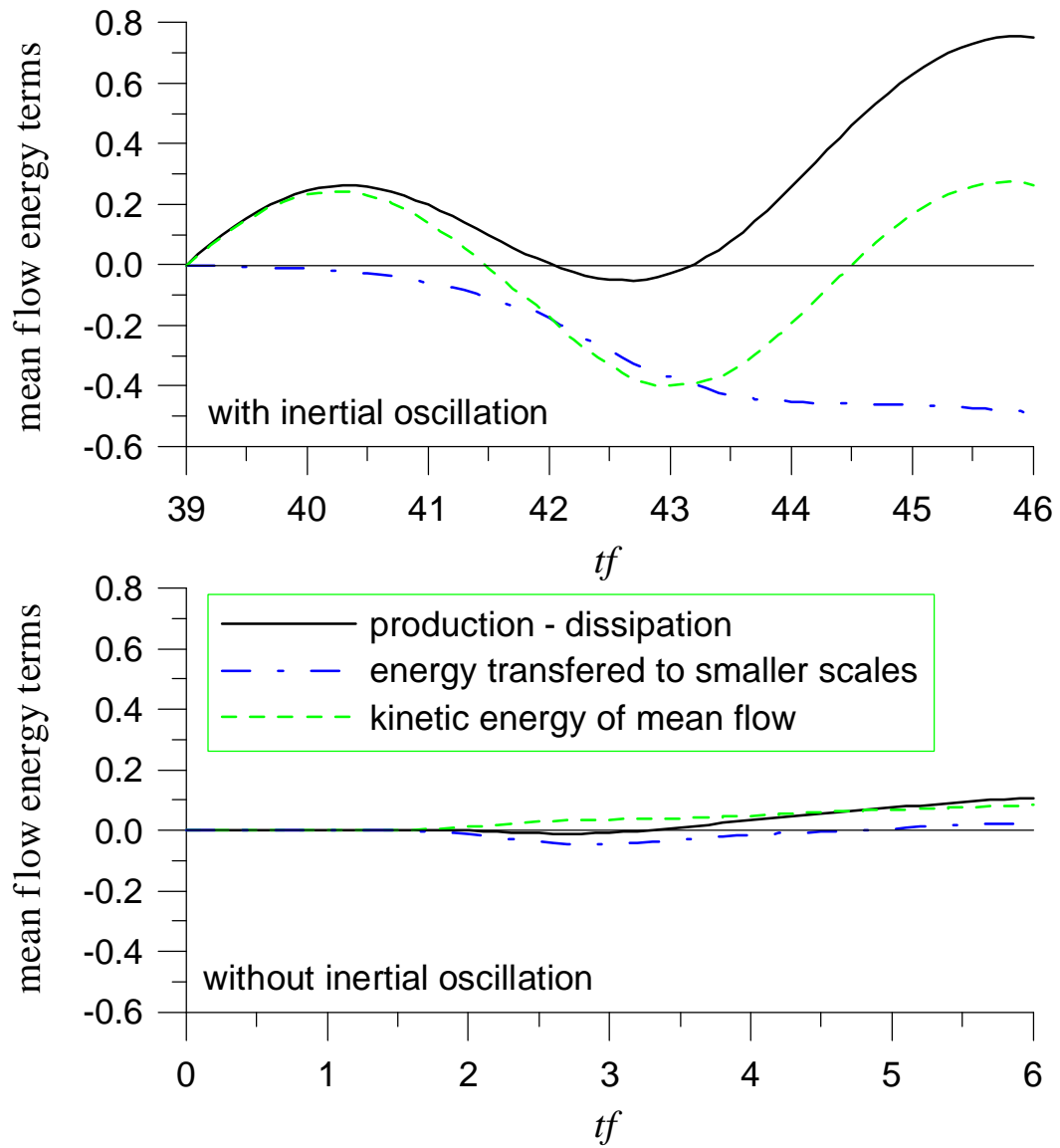


Figure 33: Time integrated terms of the mean flow kinetic energy balance. The top panel shows the balance with the inertial oscillation present, while the bottom panel shows the balance without the oscillation.

Again, we see a big difference between the two flows. Looking first at the top panel (oscillation present) we see that over a period of an inertial oscillation the kinetic energy¹⁵ of the flow (dashed green line) varies in a more-or-less sinusoidal manner, and the amount of kinetic energy is about the same at the beginning and end of the inertial period. The energy transfer to smaller scales is appreciable and about equal to the difference between the maximum and minimum value of the kinetic energy. To facilitate comparison of the energy balance with and without the oscillation, we have kept the scale of the y -axis the same between the top and bottom plots. Looking now at the bottom plot we note the very small transfer of energy to smaller scales; it is about 10% of that when the oscillation is present. Apparently the inertial oscillation's interaction with the smaller scales of the flow is a very effective mechanism of extracting energy from the work done by the mean horizontal pressure gradient and then transferring this energy to smaller scales. Without this energy transfer the intermittency mechanism described above would not exist.

We conjecture that the inertial oscillation plays a major role in the intermittency mechanism during the time that the roll vortex is lifting cold air over warmer air. In the initial stages of the development of the roll vortex, $tf = 39.0$, an intense jet (relative to the laminar profile) exists at a height of $z/D = 1$. This jet is shown in Figure 34 in which the v -component of the mean flow is plotted for various times along with the v -component of the laminar Ekman layer. This jet enhances the counterclockwise motion of the vortex which, in effect, supplies kinetic energy to the vortex. The additional kinetic energy helps overcome the gravitational force when the vortex is transporting cold air upward, and without this additional energy the transport is

¹⁵ In these plots the kinetic energy is "normalized" by setting the kinetic energy equal to zero at the beginning of the time interval in question. The energy can then assume negative values which, of course, are physically unrealistic. The normalization simply helps visualize the rate of change of the kinetic energy.

significantly weakened. While the cold air is lifted, the mean flow changes so that a strong jet

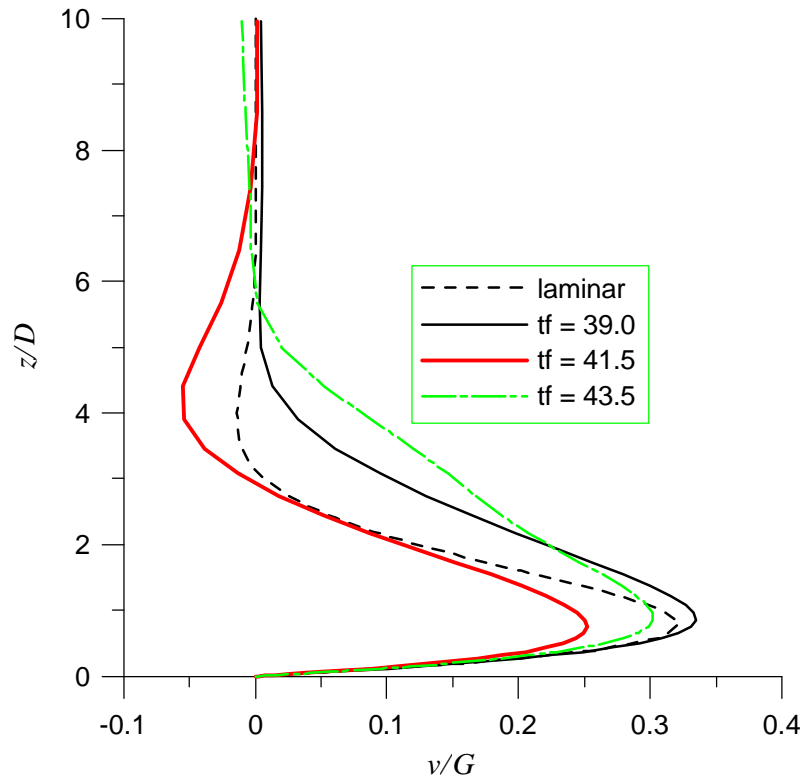


Figure 34: Profiles of the v -component of the mean flow plotted for various times. For the sake of comparison, the v -component of the laminar Ekman layer is shown by the dashed line.

develops in the negative y -direction at a height of $z/D = 4$ (see Figure 34) after a time interval of about one-quarter inertial period, $\mathbf{p}/2$, from $tf = 39.0$. This jet is fully developed at a time of $tf = 41.5$, and at this time, the cold air has reached the jet and the vortex is given another boost in the counterclockwise direction. This again aids the

lifting process and helps push cold air over warmer air so that the convective instability is set up (see the top panel of Figure 24).

Later in the intermittency process, at a time of about $tf = 43.50$, the jet that was formerly at $z/D = 4$ (at $tf = 41.5$), is obliterated. A broad area of motion in the positive y -direction replaces the jet. Such motion inhibits counterclockwise motion of the vortices thus reducing the ability of the vortices to raise cold air. The source of turbulence is therefore choked off, and additional turbulence cannot be produced until the cycle begins again.

In summary, the interaction of the inertial oscillation with the roll vortices is analogous to a pinwheel, in which a force is applied to periphery of a rotating wheel to cause the rotation. In a similar manner, the mean flow applies a boost to the outer parts of the vortices at strategic times and locations to facilitate their rotation in the counterclockwise direction. This boost apparently increases the kinetic energy of the vortices a sufficient amount to raise cold air over warm air. We call this effect the “pinwheel effect.”

Finally, for the sake of completeness, we show the TKE budget of the simulations with the oscillation present. This budget is described by the TKE equation, and for horizontally homogenous conditions, the vertically integrated TKE equation is

$$\frac{d}{dt} \int_0^{\infty} \frac{\overline{(u^2 + v^2 + w^2)}}{2} dz = - \int_0^{\infty} \left(\overline{uw} \frac{\partial \bar{U}}{\partial z} + \overline{vw} \frac{\partial \bar{V}}{\partial z} \right) dz + \text{Ri}_b \int_0^{\infty} \overline{w\Theta} dz - \int_0^{\infty} \mathbf{e} dz \quad (3.24)$$

where, in customary notation, u, v, w are the velocity fluctuations from the mean, \mathbf{e} is the dissipation, and $\overline{w\Theta}$ is the turbulent heat flux. When integrated vertically the transport term disappears. The terms in eq. 3.24 are, from left to right, the rate of change of the TKE, the shear production of TKE, the buoyant production of TKE, and the molecular dissipation. The latter three terms are calculated from the simulation

with the inertial oscillation and they are graphed in Figure 35 (bottom panel) as well as the kinetic energy (top panel). This figure shows the variation in these quantities over the time period of our

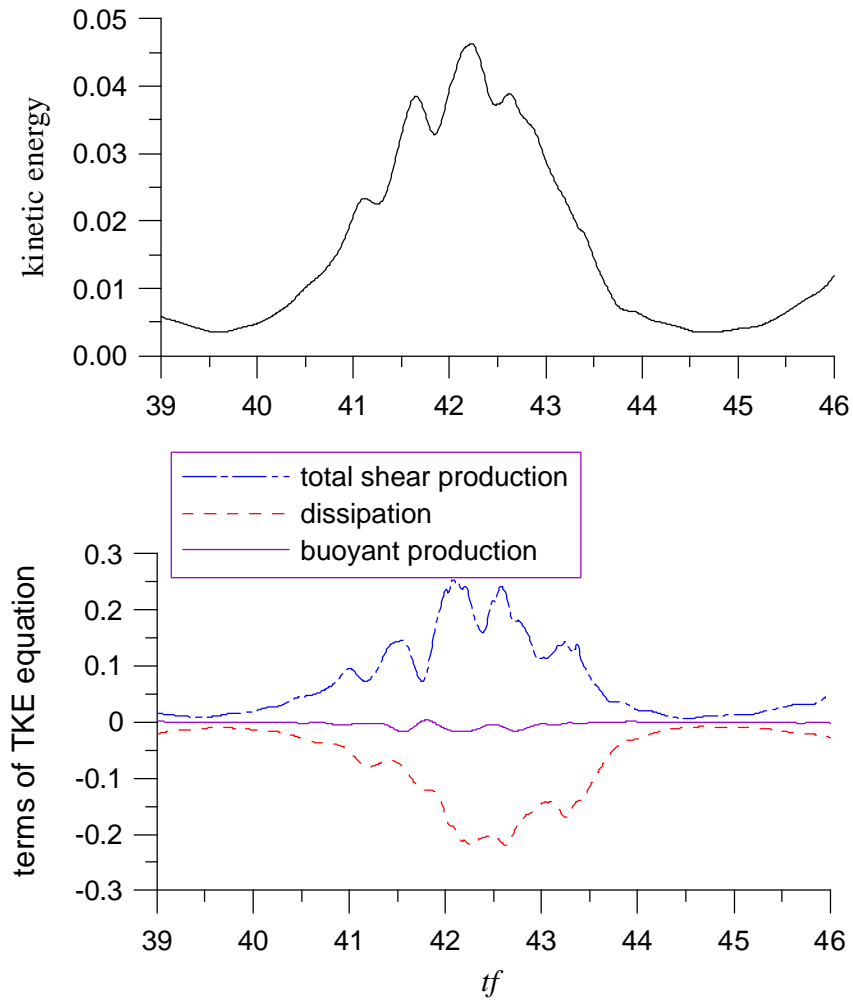


Figure 35: The top panel shows the TKE while the bottom panel shows the various terms in the vertically integrated TKE equation. These quantities have been derived from our case study with $Ri_b = 0.005$.

case study. That the TKE varies dramatically with time reflects the build up of the amplitude of the roll cells and the subsequent development of patchy turbulence. The rate terms in the bottom panel show a variation over time consistent with the kinetic energy variation. The shear production is approximately balanced by the dissipation, and the buoyant production is relatively small. Such results are consistent with measurements in the stable boundary layer, see for example, Lenschow et al. (1988).

Summary

We have put forth a mechanism to describe the origin of turbulence intermittency in the very stable boundary layer. Briefly, this mechanism follows a sequence of events in which an Ekman-like instability grows and carries colder air over warmer air. The resulting convective instability cataclysmically releases the built-up potential energy and patchy turbulence ensues. The turbulence is then quickly extinguished because the source of the turbulence, the roll cell, decays away. A key element of this mechanism is the transfer of energy from the mean flow to smaller scales aided by the inertial oscillation. Without the presence of this oscillation, the mechanism described here would not exist. The possibility that an Ekman instability could lead to turbulence in stable boundary layers was mentioned in passing by Thorpe and Guymer (1977) and our DNS simulation confirms that such a possibility is realized

An important unanswered question is whether this mechanism really exists in nature. Roll cells are easily observable during the day from cloud streets that are commonly observed from satellites or airplanes (see plate 1.3.8 in Scorer, 1972). Whether such cells exist at night under stable conditions is apparently unknown. The irregular shapes of the cells, as suggested by the DNS, would make detection even more difficult. Nevertheless the results from the DNS are not inconsistent with the limited data on turbulent bursts. Referring to Table 1, we see that the observed average number of turbulent bursts per night ranges from a low of three to a high of 18. Two of the three studies measured burst frequencies of about 3 per night. If we take an inertial period ($= \frac{1}{2}$ pendulum day) as the duration of a night, then the simulations produce turbulent bursts with a frequency on the order of 3 per night; see Figure 19 in which two major bursts are evident along with one or two minor bursts. We have placed “probes” in a few other parts of the simulation domain, and we have also found that the number of bursts per night agrees with this frequency. In this regard, the data and the simulations appear consonant.

The top panel of Figure 4 shows vertical velocity standard deviations measured by Coulter (1990). The graph in this panel is a running standard deviation over a 20-minute interval. We have calculated a similar, dimensional quantity from our simulations by a calibration of the DNS using these scale relationships:

- 12 hours = 1 inertial period, from which we conclude that 20 minutes is equal to $1/36$ of an inertial period
- $w_{\text{dimensional}} = w_{\text{nondimensional}}G$, with $G \approx 4.5$ m/sec (from Coulter, 1990)
- boundary layer height = 100 meters ((from Coulter, 1990) $\approx 5 * D$, or $D = 20$ meters)

The uppermost panel of Figure 36 shows the results of applying a running standard deviation of dimensional width “20 minutes” to a vertical velocity time series shown in Figure 19. In the middle panel the same procedure is applied to another vertical velocity time series sensed from a probe at a different height and horizontal position. The standard deviations have been dimensionalized with the velocity scale listed above. The dimensional heights of these “measurements” from the DNS are about 15 and 34 meters, respectively, for the top and middle panels.

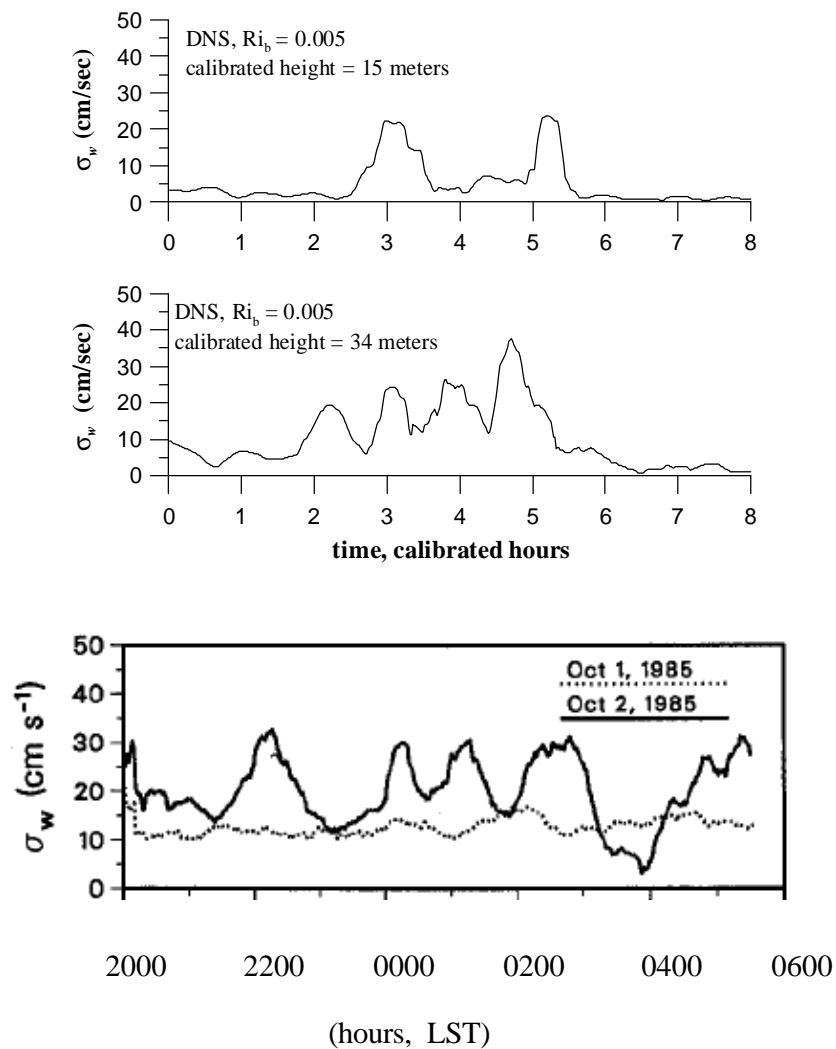


Figure 36: Top panel is a running standard deviation of dimensional width 20 minutes applied to the vertical velocity time series shown in Figure 19. The middle panel is the same for vertical velocities measured at a calibrated height of 34 meters, and the bottom panel (from Coulter, 1990) represents the same quantity, but derived from observations at a height of about 36 meters

Considering the ideal nature of the DNS and the crude calibration mentioned above, a comparison of the running standard deviations in Figure 36 derived from the simulations, with observations of the same in the top panel of Figure 4, is somewhat tenuous.

To facilitate the comparison between the observations and the simulations, this panel of Figure 4 has been reproduced in the bottom panel of Figure 36, and it is important to realize that the measurement height in Figure 4 is roughly 36 meters, about the same as probe height, 34 “calibrated” meters depicted in the middle panel of Figure 36. Focusing on the bottom two panels, we conclude that the agreement between the simulations and the observations is quite reasonable. The magnitude (about 20 - 35 cm/sec, in terms of a calibrated velocity) and spacing of the peaks (1 to 2.5 hours of “calibrated time”) of the DNS-derived standard deviations is certainly consonant with the data. To what extent the agreement is merely coincidental is an issue we cannot answer, but the very least we can say is that the DNS results are NOT inconsistent with these data.

It is also possible that K-H instabilities reported in studies such as Coulter (1990) could be mistaken for roll cell activity¹⁶. Coulter estimates the wavelength of the observed K-H instabilities to be about 540 meters. With the length calibration given above, $D = 20$ meters, we can estimate the wavelength of the roll cells to be about $13D$ or 260 meters. Considering the crude calibration of the DNS, we cannot pretend to achieve exact agreement between the two estimates. But the fact that they agree to better than order of magnitude suggests, in some situations, it could be difficult to distinguish between K-H activity and roll cell activity.

¹⁶ We are not claiming that Coulter's interpretation is in error; we are merely trying to point out that a signature of a roll cell and a K-H could be similar. This similarity could mean that K-H instabilities could be mistaken for roll cells, and visa versa. Of course, the Ekman instability and the K-H instability may be considered as two manifestations of an inflectional instability (Brown, 2000).

CHAPTER 4: CONCLUSIONS

The goal of this study has been to investigate the properties of the VSBL using a DNS of an idealized boundary layer flow, the Ekman layer. We performed a number of simulations in which the Ekman layer was cooled from below after turbulence had fully developed under neutrally stratified conditions. The strength of the cooling was varied from simulation to simulation in an effort to find the characteristic signature, turbulence intermittency, of the VSBL. Once we found simulations in which intermittency was evident, we investigated some important issues concerning the VSBL. These issues are the delineation of boundaries in “stability parameter space” that mark where the VSBL is found and, more importantly, the manner in which intermittent turbulence develops under very stable conditions.

Taking on the issue of boundary demarcation first, we explicitly defined the VSBL in terms of the primary physical property, intermittent turbulence, that distinguishes this boundary layer from less stable ones. Once this definition was established, we studied the mapping of values of various stability parameters to the onset of intermittency, and therefore, to the VSBL. Most of these parameters form a continuum that spans unstable conditions to stable conditions. What is sought is the point along this continuum that serves as a signpost for where the VSBL begins. To this end we examined these proposed boundaries:

- the maximum downward heat flux (Derbyshire, 1990) for which continuous turbulence is maintained; for heat fluxes greater than this value the boundary layer is considered to be very stable.
- $z/L = 1$, as proposed by Howell and Sun (1999); for z/L greater than this value, the boundary layer is very stable.

From the DNS we have concluded that both the maximum heat flux criterion and the value of stability parameter, $z/L = 1$, as proposed by Howell and Sun (1999), serve as appropriate markers of the VSBL. Of these two criteria, the use of z/L to define the VSBL is most practical. We also noted that Mahrt's (1998) analysis of the MICROFRONTS observations indicate that the maximum heat flux occurs at a value of $z/L (\approx z/\Lambda)^{17}$ which is much less than the value, $z/L = 1$, found to be the boundary between moderately stable and very stable conditions. Thus, these observations would imply that the maximum heat flux boundary proposed by Derbyshire (1990) is not correct, or the conclusions drawn by Mahrt et al. (1998) are dependent on the specific data set examined. This last point may have prompted Mahrt (1998) to warn that the exact value of z/L where the maximum heat flux occurs may not be universal (and certainly may vary with height, z).

Next, we examined the specific mechanism that causes turbulence intermittency in the simulations. This intermittency exists only for bulk Richardson numbers, Ri_b , greater than about 0.05. The intermittency develops from an Ekman-like instability following this chain of events. From a laminar flow state, irregular roll cells are generated by the Ekman instability. The cells are vigorous enough to transport patches of colder air over warmer air, at which time a small part of the atmosphere becomes convectively unstable. The instability quickly releases potential energy resulting in intense patches of turbulence. After the turbulence is generated, the roll cell that sets up the convective instability disintegrates and the source of turbulence ceases to exist. Thus, the flow becomes laminar again as the turbulence is dissipated by viscosity.

During the events that lead to turbulence intermittency, an inertial oscillation in the mean flow is observed. This oscillation, working in conjunction with the smaller scale flow, is very effective in transferring energy from the work done by the mean pressure

¹⁷ Note: for the discussion here we may take $L \approx \Lambda$.

gradient to the smaller scales of the flow. This transfer of energy is crucial for the development of roll cells with sufficient strength to lift cold air over warm air. When simulations are run in which the oscillation is effectively erased, intermittency is not observed. The inertial oscillation appears to aid in the development of patch turbulence by enhancing the strength of the roll cell circulation.

Examples of intermittency found in simulations were compared with similar examples obtained from atmospheric measurements. This comparison indicates that the DNS results are not inconsistent with the observations and that the mechanism proposed here may well occur in the atmosphere.

There is some uncertainty as to whether the transition from the moderately stable boundary layer to the VSBL involves a fundamental change in physics of the flow, or whether the stratification becomes so large that the source of the turbulence can no longer support continuous turbulence. The DNS appears to support both these propositions! As pointed out by Brown (1974) energy is transferred from the mean flow to the turbulent flow through various flow instabilities. The two primary types of instability that mediate this energy transfer are the inflectional instability (Drazin and Reid, 1989) and the convective instability. The DNS indicates that both instabilities play important roles in the development of intermittency, but circulations stemming from the inflectional instability precede the convective stability. With this order in mind, we can consider the inflectional instability as the ultimate source of the turbulence. This instability weakens as the stratification becomes larger so that cold air cannot be lifted above warm air. Such weakening is seen in the DNS at large stratifications ($Ri_b = 0.01$) in which very weak, laminar roll cell circulations develop, and these weak circulations cannot lift cold air over warm air. The weakening of the circulations is related to the well-established physics of stratification reducing the growth rates of an inflectional instability.

On the other hand, when intermittency develops according to the scheme discovered here, new physics is brought to bear. This new physics is evident in the interaction of the inertial oscillation with the roll cell circulation -- the pinwheel effect -- without which the intermittency could not develop. Thus, it appears that both new physics (pinwheel effect) and well-established physics (inflectional and convective instabilities) contribute to the intermittency mechanism described in this study.

This mechanism is but one possible way that intermittent turbulence can arise. This brings up yet another question: when is this mechanism operative? We speculate that this mechanism would most likely occur over flat terrain, with clear skies so that the boundary layer cools rapidly after sunset because of strong cooling by longwave radiation to space. This strong cooling would foster the quick development of an inertial oscillation because the near-surface turbulence would be rapidly inhibited by the increase in stable stratification. In complex terrain it is likely that patchy turbulence would tend to develop in other ways because the terrain would facilitate the development of gravity waves that might break and cause turbulence. Which intermittency mechanism would be favored under different conditions is a question that has yet to be answered.

Considering the ever-increasing power of the computer, it would be desirable to repeat the simulations at a larger Reynolds number. Although the framework of intermittency mechanism described above should not depend greatly on the Reynolds number (provided it is sufficiently large, and we think Re is large enough), the details of the mechanism such as roll cell growth rates would be altered. Simulations performed at larger Re would strengthen the conclusions stated here and make the comparison between the simulations and data more secure.

Additional data collection and analysis is a critical activity that should contribute to our understanding of the VSBL. Such data may provide evidence of roll vortices in

VSBLs and therefore substantiate the findings of this study. Field studies designed to measure properties of the stable boundary layers have recently been carried out (for example, CASES – 99, Poulos et al., 2000), and analysis of these data may shed light on what intermittency mechanisms are active.

BIBLIOGRAPHY.

- Andr n, A. and C.-H. Moeng, 1993: Single-point closures in a neutrally stratified boundary layer. *J. Atmos. Sci.*, **50**, 3366-3379.
- Andr n, A., A. R. Brown, J. Graf, P. J. Mason, F. T. M. Nieuwstadt, and U. Schumann, 1994: Large-eddy simulation of a neutrally stratified boundary layer: A comparison of four computer codes. *Q. J. R. Met. Soc.*, **120**, 1457-1484.
- Apel, J. R., 1990: *Principles of Ocean Physics*. International Geophysics Series, Vol. 38, Academic Press, 634 pp.
- Arya, S. P. S., 1981: Parameterizing the height of the stable atmospheric boundary layer. *J. Appl. Meteor.*, **20**, 1192-1202.
- Arya, S. P. S., 1988: *Introduction to Micrometeorology*. Academic Press, Inc., 307 pp.
- Blackadar, A. K., 1957: Boundary layer wind maxima and their significance for the growth of nocturnal inversion. *Bull. Amer. Meteor. Soc.*, **38**, 283-290.
- Blackadar, A. K., 1979: High-resolution models of the planetary boundary layer. *Advances in Environmental Science and Engineering*, J. R. Pfafflin and E. N. Ziegler, Eds., Gordon and Breach Sci. Pub., Inc., 50-85.
- Boyd, J. P., 1982: The optimization of convergence for the Chebyshev polynomial methods in an unbounded domain, *J. Comput. Phys.*, **45**, 43-79.
- Brost, R. A., and J. C. Wyngaard, 1978: A model study of the stably stratified planetary boundary layer. *J. Atmos. Sci.*, **35**, 1427-1440.

- Brown, R. A., 1972: On the inflection point instability of a stratified Ekman boundary layer. *J. Atmos. Sci.*, **29**, 850-859.
- Brown, R. A., 1974: *Analytical Methods in Planetary Boundary-Layer Modeling*. John Wiley & Sons, 148 pp.
- Brown, R. A., 2000: Personal communication.
- Brown, A. R., S. H. Derbyshire, and P. J. Mason, 1994: Large-eddy simulation of stable atmospheric boundary layers with a revised stochastic subgrid model. *Q. J. R. Met. Soc.*, **120**, 1485-1512.
- Businger, J. A., 1973: "Turbulent transfer in the atmospheric surface layer", in *Workshop on Micrometeorology*, D. A. Haugen (ed.) Amer. Meteor. Soc., Boston, Massachusetts, 392 pp.
- Caldwell, D. R., C. W. van Atta, and K. N. Helland. 1972: A laboratory study of the turbulent Ekman layer. *Geophys. Fluid Dyn.*, **3**, 125-348.
- Canuto, C., M. Y. Hussaini, A. Quarteroni, and T. A. Zang. 1988: *Spectral Methods in Fluid Dynamics*. Springer-Verlag, 557 pp.
- Carruthers, D. J. and J. C. R. Hunt, 1986: Velocity fluctuations near an interface between a turbulent region and a stably stratified layer. *J. Fluid Mech.*, **165**, 475-501.
- Coleman, G. N., J. H. Ferziger, and P. R. Spalart, 1990a: A numerical study of the turbulent Ekman layer. *J. Fluid. Mech.*, **213**, 313-348.
- Coleman, G. N., J. H. Ferziger, and P. R. Spalart, 1990b: A numerical study of the stratified turbulent Ekman layer. Department of Mechanical Engineering, Stanford University, Thermosciences Division report No. TF-48, 245 pp.

- Coleman, G. N., J. H. Ferziger, and P. R. Spalart, 1992: Direct simulation of the stably stratified turbulent Ekman layer. *J. Fluid. Mech.*, **244**, 677-712.
- Coleman, G. N., J. H. Ferziger, and P. R. Spalart, 1994: A numerical study of the convective boundary layer. *Boundary-Layer Meteorology*, **70**, 247-272.
- Coleman, G. N., 1999: Similarity statistics from a Direct Numerical Simulation of the neutrally stratified planetary boundary layer. *J. Atmos. Sci.*, **56**, 891-900.
- Coulter, R. L., 1990: A case study of turbulence in the stable nocturnal boundary layer. *Boundary-Layer Meteorology*, **52**, 75-91.
- Craik, A. D. D., 1991: The continuous spectrum of the Orr-Sommerfeld equation: note on a paper of Grosch & Salwen. *J. Fluid Mech.*, **226**, 565-571.
- Dalai Lama, and H. C. Cutler, 1998: *The Art of Happiness*. Rivercourt Books, 322 pp.
- de Bruyn Kops, S. M. and J. J. Riley, 1998: Direct numerical simulation of laboratory experiments in isotropic turbulence. *Phys. Fluids*, **10**, 2125-2127.
- De Bruin, H. A. R., 1994: Analytic solutions of the equations governing the temperature fluctuation method. *Boundary-Layer Meteorology*, **68**, 427-432.
- Derbyshire, S. H., 1990: Nieuwstadt's stable boundary layer revisited. *Q. J. R. Met. Soc.*, **116**, 127-158.
- Derbyshire, S. H., 1999: Stable boundary-layer modeling: Established approaches and beyond. *Boundary-Layer Meteorology*, **90**, 423-446.
- Dörnbach, A., 1998: Turbulent mixing by breaking gravity waves. *J. Fluid Mech.*, **375**, 113-141.

- Drazin, P. G. and W. H. Reid, 1989: *Hydrodynamic Stability*. Cambridge University Press.
- Drobinski, R. and R. C. Foster, 2000: On the dynamics of near surface streaks in the neutrally stratified planetary boundary layer. Submitted to *Boundary-Layer Meteorology*.
- Einaudi, F. and J. J. Finnigan, 1981: The interaction between an internal gravity wave and the planetary boundary layer. Part I: The linear analysis. *Q. J. R. Met. Soc.*, **107**, 793-806.
- Ekman, V. W., 1905: On the influence of the Earth's rotation on ocean currents. *Arkiv för matematik, astronomi o. fysik*, **2**, 1-52.
- Etling, D. and R. A. Brown, 1993: Roll vortices in the planetary boundary layer: a review. *Boundary-Layer Meteorology*, **65**, 215-248.
- Finnigan, J. J. and F. Einaudi, 1981: The interaction between an internal gravity wave and the planetary boundary layer. Part II: Effect of the wave on the turbulence structure. *Quart. J. R. Met. Soc.*, **107**, 807-832.
- Foster, R. C., 1997: Structure and energetics of optimal Ekman layer perturbations. *J. Fluid Mech.*, **333**, 97-123.
- Garratt, J. R., 1992: *The Atmospheric Boundary Layer*. Cambridge University Press, 316 pp.
- Gill, A. E., 1982: *Atmosphere-Ocean Dynamics*. International Geophysics Series, Vol. 30, Academic Press, 662 pp.
- Grosch, C. E., and S. A. Orzag, 1977: Numerical Solution of Problems in Unbounded Regions: Coordinate Transforms. *J. Computational Physics*, **25**, 273-296.

Grosch, C. E., and H. Salwen, 1978: The continuous spectrum of the Orr-Sommerfeld equation. Part 1. The spectrum and the eigenfunctions. *J. Fluid Mech.*, **87**, 33-54.

Gryning, Sven-Erik, 1999: Some aspects of atmospheric dispersion on the stratified atmospheric boundary layer. *Boundary-Layer Meteorology*, **90**, 479-494.

Harrison, R. M., Holman, C. D., McCortney, H. A., and McIlvinn, J. F. R., 1978: Nocturnal Depletion of Photochemical ozone at a rural site, *Atmos. Environ.*, **12**, 2021-2026.

Hartman, J., C. Kottmeier, and S. Raasch, 1997: Roll vortices and boundary-layer development during a cold air outbreak. *Boundary-Layer Meteorology*, **84**, 45-65.

Högström, U., 1996: Review of some basic characteristics of the atmospheric surface layer. *Boundary-Layer Meteorology*, **78**, 215-246.

Howell, J. F., and J. Sun, 1999: Surface layer fluxes in stable conditions, *Boundary-Layer Meteorology*, **90**, 495-520.

Jacobitz, F. G., S. Sarkar, and C. W. Van Atta, 1997: Direct numerical simulations of the turbulence evolution in a uniformly sheared and stably stratified flow. *J. Fluid Mech.*, **342**, 231-261.

Kaylor, R., and A. J. Faller, 1972: Instability of the stratified Ekman boundary layer and the generation of internal waves. *J. Atmos. Sci.*, **29**, 497-509.

Kemp, J. R., and D. J. Thomson, 1996: Dispersion in stable boundary layers using large-eddy simulation. *Atmospheric Environment*, **30**, 2911-2933.

Khana, S., and J. G. Brasseur, 1997: Analysis of Monin-Obukhov similarity from large-eddy simulation. *J. Fluid Mech.*, **345**, 251-286.

- Kosovic, B., and J. A. Curry, 2000: A large eddy simulation of a quasi-steady, stably stratified atmospheric boundary layer. *J. Atmos. Sci.*, **57**, 1052-1068.
- Lenschow, D. H., X. S. Li, C. J. Zhu, and B. B. Stankov, 1988: The stably stratified boundary layer over the Great Plains. I. Mean and turbulence structure. *Boundary-Layer Meteorology*, **42**, 95-121.
- Leonard, A., and A. A. Wray, 1982: In *8th International Conference On Numerical Methods in Fluid Dynamics*, edited by E. Krause, Springer-Verlag.
- Lilly, D. K., 1966: On the instability of Ekman boundary layer flow. *J. Atmos. Sci.*, **23**, 481-494.
- Lombard, P. N., and J. J. Riley, 1996a: Instability and breakdown of internal gravity waves. I. Linear stability analysis. *Phys. Fluids*, **8**, 3271-3287.
- Lombard, P. N., and J. J. Riley, 1996b: On the breakdown into turbulence of propagating internal waves. *Dyn. Atmos. Oceans*, **23**, 345-355.
- Mahrt, L., 1985: Vertical structure and turbulence in a very stable boundary layer. *J. Atmos. Sci.*, **42**, 2333-2349.
- Mahrt, L., J. Sun, W. Blumen, T. Delany, and S. Oncley, 1998: Nocturnal boundary-layer regimes, *Boundary-Layer Meteorology*, **88**, 255-278.
- Mahrt, L., 1998: Stratified atmospheric boundary layers and breakdown of models. *Theor. Comp. Fluid Dyn.*, **11**, 263-280.
- Mahrt, L., 1999: Stratified atmospheric boundary layers, *Boundary-Layer Meteorology*, **90**, 375-396.

- Malhi, Y. S., 1995: The significance of the dual solution for heat fluxes measured by the temperature fluctuation method in stable conditions. *Boundary-Layer Meteorology*, **74**, 389-396.
- Mason, P. J., and S. H. Derbyshire, 1990: Large-eddy simulation of the stably stratified boundary layer. *Boundary-Layer Meteorology*, **53**, 117-162.
- Mason, P. J., and D. J. Thomson, 1992: Stochastic backscatter in the large-eddy simulation of boundary layers. *J. Fluid Mech.*, **242**, 51-78.
- Mason, P. J., 1994: Large-eddy simulation: A critical review of the technique. *Q. J. R. Met. Soc.*, **120**, 1-26.
- McNider, R. T., D. E. England, M. J. Friedman, and X. Shi, 1995: Predictability of the stable atmospheric boundary layer. *J. Atmos. Sci.*, **52**, 1602-1614.
- Melander, M. V., 1983: An algorithmic approach to the linear stability of the Ekman layer. *J. Fluid Mech.*, **132**, 283-293.
- Metcalf, R. W., S. A. Orzag, M. E. Brachet, S. Menon, and J. J. Riley, 1987: Secondary instability of a temporally growing mixing layer, *J. Fluid Mech.*, **184**, 207-243.
- Moeng, C-H., and P. P. Sullivan, 1994: A comparison of shear- and buoyancy-driven planetary boundary layer flows. *J. Atmos. Sci.*, **51**, 999-1022.
- Nappo, C. J., 1991: Sporadic breakdown of stability in the PBL over simple and complex terrain. *Boundary-Layer Meteorology*, **54**, 69-87.
- Nieuwstadt, F. T. M., and H. Tennekes, 1981: A rate equation for the nocturnal boundary-layer height. *J. Atmos. Sci.*, **38**, 1418-1428.

- Nieuwstadt, F. T. M., 1984: The turbulent structure of the stable, nocturnal boundary layer. *J. Atmos. Sci.*, **41**, 2202-2216.
- Nieuwstadt, F. T. M., 1985: A model for the stationary, stable boundary layer. *Turbulence and diffusion in stable environments*, J. C. R. Hunt, Ed., Clarendon Press, Oxford, United Kingdom, 149-179.
- Ohya, Y., D. E. Neff, and R. N. Meroney, 1997: Turbulence structure in a stratified boundary layer under stable conditions. *Boundary-Layer Meteorology*, **83**, 139-161.
- Panton, R. L., 1984: *Incompressible Flow*. Wiley & Sons, 780 pp.
- Poulos, G. S., D. C. Fritts, W. Blumen, and W. D. Bach, 2000: CASES-99 Field Experiment: An Overview, *14th Symposium on Boundary Layer and Turbulence*, Aspen, Colorado.
- Rao, K. S., 1999: Lagrangian stochastic modeling of dispersion in the stable boundary layer. *Boundary-Layer Meteorology*, **90**, 541-549.
- ReVelle, D. O., 1993: Chaos and “bursting” in the planetary boundary layer. *J. Appl. Meteor.*, **32**, 1169-1180.
- Riley, J. J., and R. W. Metcalf, 1987: Direct numerical simulations of turbulent patches in stably stratified fluids. *Third International Symposium on Stratified Flows Vol. I*, Pasadena, California.
- Riley, J. J. and M.-P. Lelong, 2000: Fluid motions in the presence of strong stable stratification. *Annu. Rev. Fluid Mech.*, **32**, 613-657.
- Rogallo, R. S., and P. Moin, 1984: Numerical simulations of turbulent flows. *Ann. Rev. Fluid Mech.*, **16**, 99-137.

- Rogers, M. M. and R. D. Moser, 1992: The three-dimensional evolution of a plane mixing layer: the Kelvin-Helmholtz rollup. *J. Fluid Mech.*, **243**, 183-226.
- Saiki, E. M., C.-H. Moeng, and P. P. Sullivan, 2000: Large-eddy simulation of the stably stratified planetary boundary layer. *Boundary-Layer Meteorology*, **95**, 1-20.
- Schlichting, H., 1968: *Boundary Layer Theory*, McGraw-Hill, 748 pp.
- Schubert, J. F., 1977: Acoustic detection of momentum transfer during the abrupt transition from a laminar to a turbulent atmospheric boundary layer. *J. Appl. Meteor.*, **16**, 1292-1297.
- Scorer, R., 1972. *Clouds of the World. A Complete Colour Encyclopedia*. Lothian Publishing Co. Ltd., 176 pp.
- Shaw, William, 2000. Personal communication.
- Smedman, A-S., 1988: Observations of a multi-level turbulence structure in a very stable atmospheric boundary layer. *Boundary-Layer Meteorology*, **44**, 231-253.
- Sorbjan, Z., 1988: Structure of the stably stratified boundary layer during the SESAME-1979 experiment. *Boundary-Layer Meteorology*, **44**, 255-266.
- Spalart, P. R., R. D. Moser, and M. M. Rogers, 1991: Spectral methods for the Navier-Stokes equations with one infinite and two periodic directions. *J. Comput. Phys.*, **96**, 297-324.
- Staquet, C., and J. J. Riley, 1989: A numerical study of a stably stratified mixing layer. *Turbulent Shear Flows 6*. Springer-Verlag.
- Stull, R., 1991: *An Introduction to Boundary Layer Meteorology*. Kluwer Academic Publishers, 666 pp.

- Tennekes, H., and J. L. Lumley, 1989: *A First Course in Turbulence*. The MIT Press, 300 pp.
- Thorpe, S. A., and T. H. Guymer, 1977: The nocturnal jet. *Q. J. R. Met. Soc.*, **103**, 633-653.
- Townsend, A. A., 1980: *The Structure of Turbulent Shear Flow*. 2d ed. Cambridge University Press, 429 pp.
- Tritton, D. J., 1988: *Physical Fluid Dynamics*. Oxford University Press, 519 pp.
- Winters, K. B., and E. A. D'Asaro, 1989: Two-dimensional instability of finite amplitude internal gravity wave packets near a critical level. *J. Geophysical Res.*, **94**, No. C9, 12709-12719.
- Winters, K. B., and E. A. D'Asaro, 1994: Three-dimensional wave instability near a critical layer. *J. Fluid Mech.*, **272**, 255-284.
- Wyngaard, J. C., 1973: On surface layer turbulence. *Workshop on Micrometeorology*, D. A. Haugen, Ed., American Meteorological Society, 109-149.

APPENDIX A: THE CONTINUOUS SPECTRUM OF THE LAMINAR, STRATIFIED EKMAN LAYER

In this appendix we briefly outline the derivation of the continuous spectrum of eigenvalues associated with the laminar stratified Ekman layer. We begin with the full equation set transformed to Fourier space and then decomposed into the \parallel, \perp form, eqs. 2.39 – 2.42,

$$\begin{aligned} \frac{\partial \hat{u}_{\mathbf{k}}^{\square}}{\partial t} + \frac{k_x \square NL^x_{\mathbf{k}} + k_y \square NL^y_{\mathbf{k}}}{|\mathbf{k}|} = \\ i \frac{2\mathbf{p}}{L} |\mathbf{k}| \hat{p}_{\mathbf{k}} + \frac{1}{\text{Re}} \left(\frac{\partial^2}{\partial z^2} - \left(\frac{2\mathbf{p}|\mathbf{k}|}{L} \right)^2 \right) \hat{u}_{\mathbf{k}}^{\square} + \frac{1}{\text{Ro}} \hat{u}_{\mathbf{k}}^{\perp} + \left(i \frac{2\mathbf{p}|\mathbf{k}| U_{BS}^{\square}}{L} \hat{u}_{\mathbf{k}}^{\square} - \hat{w}_{\mathbf{k}} \frac{dU_{BS}^{\square}}{dz} \right) \end{aligned} \quad (\text{A.1})$$

$$\begin{aligned} \frac{\partial \hat{u}_{\mathbf{k}}^{\perp}}{\partial t} + \frac{k_x \square NL^y_{\mathbf{k}} - k_y \square NL^x_{\mathbf{k}}}{|\mathbf{k}|} = \\ \frac{1}{\text{Re}} \left(\frac{\partial^2}{\partial z^2} - \left(\frac{2\mathbf{p}|\mathbf{k}|}{L} \right)^2 \right) \hat{u}_{\mathbf{k}}^{\perp} - \frac{1}{\text{Ro}} \hat{u}_{\mathbf{k}}^{\square} + \left(i \frac{2\mathbf{p}|\mathbf{k}| U_{BS}^{\square}}{L} \hat{u}_{\mathbf{k}}^{\perp} - \hat{w}_{\mathbf{k}} \frac{dU_{BS}^{\perp}}{dz} \right) \end{aligned} \quad (\text{A.2})$$

$$\begin{aligned} \frac{\partial \hat{w}_{\mathbf{k}}}{\partial t} + \square NL^z_{\mathbf{k}} = \\ - \frac{\partial \hat{p}_{\mathbf{k}}}{\partial z} + \frac{1}{\text{Re}} \left(\frac{\partial^2}{\partial z^2} - \left(\frac{2\mathbf{p}|\mathbf{k}|}{L} \right)^2 \right) \hat{w}_{\mathbf{k}} + \text{Ri}_b \hat{\Theta}_{\mathbf{k}} + i \frac{2\mathbf{p}|\mathbf{k}| U_{BS}^{\square}}{L} \hat{w}_{\mathbf{k}} \end{aligned} \quad (\text{A.3})$$

$$\begin{aligned} \frac{\partial \hat{\Theta}_{\mathbf{k}}}{\partial t} + \left(-i \frac{2\mathbf{p}k_x}{L}, -i \frac{2\mathbf{p}k_y}{L}, \frac{\partial}{\partial z} \right) \cdot \square \hat{\Theta}_{\mathbf{k}} + \hat{w}_{\mathbf{k}} \frac{\partial \Theta_d}{\partial z} = \\ \frac{1}{\text{RePr}} \left(\frac{\partial^2}{\partial z^2} - \left(\frac{2\mathbf{p}|\mathbf{k}|}{L} \right)^2 \right) \hat{\Theta}_{\mathbf{k}} + i \frac{2\mathbf{p}|\mathbf{k}| U_{BS}^{\square}}{L} \hat{\Theta}_{\mathbf{k}} \end{aligned} \quad (\text{A.4})$$

We now: (1) linearize by simply dropping the nonlinear terms, (2) set $\mathbf{a} = 2\mathbf{p}|\mathbf{k}|/L$, (3) assume that the buoyancy frequency, N , is constant with height so that $\partial\Theta_d/\partial z = 1$ everywhere¹⁸; and, finally, (4) assume a time dependence for the independent variables of the form, e^{iact} where c is the complex phase speed. This last assumption implies disturbances of the form $w(x, z, t) = \hat{w}_a(z)e^{-ia(x-ct)}$. The equations now become

$$-i\mathbf{a}(U_{BS}^\square - c)\hat{u}_a^\square = i\mathbf{a}\hat{p}_a + \frac{1}{\text{Re}}\left(\frac{d^2}{dz^2} - \mathbf{a}^2\right)\hat{u}_a^\square + \frac{1}{\text{Ro}}\hat{u}_a^\perp - \hat{w}_a\frac{dU_{BS}^\square}{dz} \quad (\text{A.5})$$

$$-i\mathbf{a}(U_{BS}^\square - c)\hat{u}_a^\perp = \frac{1}{\text{Re}}\left(\frac{d^2}{dz^2} - \mathbf{a}^2\right)\hat{u}_a^\perp - \frac{1}{\text{Ro}}\hat{u}_a^\square - \hat{w}_a\frac{dU_{BS}^\perp}{dz} \quad (\text{A.6})$$

$$-i\mathbf{a}(U_{BS}^\square - c)\hat{w}_a = -\frac{\partial\hat{p}_a}{\partial z} + \frac{1}{\text{Re}}\left(\frac{d^2}{dz^2} - \mathbf{a}^2\right)\hat{w}_a + \text{Ri}_b\hat{\Theta}_a \quad (\text{A.7})$$

$$-i\mathbf{a}(U_{BS}^\square - c)\hat{\Theta}_a + \hat{w}_a = \frac{1}{\text{RePr}}\left(\frac{d^2}{dz^2} - \mathbf{a}^2\right)\hat{\Theta}_a \quad (\text{A.8})$$

The continuity equation is

$$-i\mathbf{a}\hat{u}_a^\square + \frac{\partial\hat{w}_a}{\partial z} = 0 \quad (\text{A.9})$$

The pressure can be eliminated from this set of equations by differentiating eq. A.5 with respect to z and adding the differentiated equation to $i\mathbf{a}$ times eq. A.7 and making

¹⁸ The assumption that N is constant with height implies that $d\Theta_d/dz$ is constant with height. To be compatible with our definition of the lower boundary condition we must have $d\Theta_d/dz$ equal to one.

liberal use of the continuity equation. We are in effect finding a vorticity equation. The resulting equation is

$$\left(-\frac{1}{i\mathbf{a} \operatorname{Re}} \left(\frac{d^2}{dz^2} - \mathbf{a}^2 \right)^2 - (U_{BS}^\square - c) \left(\frac{d^2}{dz^2} - \mathbf{a}^2 \right) + \frac{d^2 U_{BS}^\square}{dz^2} \right) \hat{w}_a = \frac{1}{\operatorname{Ro}} \frac{d\hat{u}_a^\perp}{dz} + i\mathbf{a} \operatorname{Ri}_b \hat{\Theta}_a \quad (\text{A.10})$$

When \hat{u}_a^\square is replaced in eq. A.6 by $\frac{1}{i\mathbf{a}} \frac{d\hat{w}_a}{dz}$ (continuity), eqs. A.10, A.8 and the modified A.6 form a complete set of equations for the variables \hat{w}_a , \hat{u}_a^\perp , and $\hat{\Theta}_a$. Extending the theory of Grosch and Salwen (1978), we seek solutions of these equations that are merely bounded at infinity; that is $|\hat{w}_a|_{z \rightarrow \infty} < \infty$ ¹⁹. This boundary condition is less stringent than that imposed in the normal eigenvalue problem in which we require that the solutions vanish at infinity. To find the nature of these bounded solutions as $z \rightarrow \infty$, we find the asymptotic form of the equations appropriate for $z \rightarrow \infty$. Because U_{BS}^\square becomes constant in this limit ($U_{BS}^\square = \cos(\mathbf{e}_k)$, \mathbf{e}_k is the angle the wavenumber makes with the k_x -axis), all derivatives (d/dz) of U_{BS}^\square are therefore zero as $z \rightarrow \infty$. We furthermore assume that the form of the solution for large z is sinusoidal, or $\hat{w}_a, \hat{u}_a^\perp, \hat{\Theta}_a \sim e^{ibz}$ and derivative operators such as d^2/dz^2 can be replaced by $-b^2$, where b is the vertical wavenumber. The asymptotic equations, valid for $z \rightarrow \infty$, become

$$\left(-\frac{1}{i\mathbf{a} \operatorname{Re}} (-b^2 - \mathbf{a}^2)^2 - (U_{BS}^\square - c) (-b^2 - \mathbf{a}^2) \right) \hat{w}_a - \frac{1}{\operatorname{Ro}} ib\hat{u}_a^\perp - i\mathbf{a} \operatorname{Ri}_b \hat{\Theta}_a = 0 \quad (\text{A.11})$$

¹⁹ Grosch and Salwen (1978) discuss the details of how the boundary condition at $z = 0$ is satisfied.

$$\left(-\frac{1}{ia \operatorname{Re}}(-b^2 - \mathbf{a}^2) - (U_{BS}^\square - c) \right) \hat{u}_a^\perp - \frac{ib}{\mathbf{a}^2} \frac{1}{\operatorname{Ro}} \hat{w}_a = 0 \quad (\text{A.12})$$

$$\left(-\frac{1}{ia \operatorname{RePr}}(-b^2 - \mathbf{a}^2) - (U_{BS}^\square - c) \right) \hat{\Theta}_a - \frac{i\hat{w}_a}{\mathbf{a}} = 0 \quad (\text{A.13})$$

The equations A.11 through A.13 form a homogenous equation set and for a solution to exist the determinant must vanish. This requirement results in a third order polynomial, and the roots of this equation are the eigenvalues c of the continuous spectrum. Because a closed form solution exists for the roots of a cubic polynomial, it is possible to find a closed form solution for the eigenvalues. For $\operatorname{Pr} = 1$, this closed form solution takes the very simple form embodied in eq. 2.91 and eq. A.14 below.

Knowledge of the continuous spectrum is very useful for several reasons. First, we can determine if any disturbance associated with the spectrum grows or decays. For this analysis we shall assume for the sake of simplicity that $\operatorname{Pr} = 1$, but the analysis can be extended to other Prandtl numbers as well. For $\operatorname{Pr} = 1$, the eigenvalues are (eq 2.91)

$$c = \left\{ \begin{array}{l} \cos(\mathbf{e}_k) - \frac{1}{ia \operatorname{Re}}(b^2 + \mathbf{a}^2) \\ \cos(\mathbf{e}_k) - \frac{\sqrt{\operatorname{Ri}_b + \frac{b^2}{\mathbf{a}^2 \operatorname{Ro}^2}}}{\sqrt{b^2 + \mathbf{a}^2}} - \frac{1}{ia \operatorname{Re}}(b^2 + \mathbf{a}^2) \\ \cos(\mathbf{e}_k) + \frac{\sqrt{\operatorname{Ri}_b + \frac{b^2}{\mathbf{a}^2 \operatorname{Ro}^2}}}{\sqrt{b^2 + \mathbf{a}^2}} - \frac{1}{ia \operatorname{Re}}(b^2 + \mathbf{a}^2) \end{array} \right\} \quad (\text{A.14})$$

For the case $\operatorname{Ri}_b + \frac{b^2}{\mathbf{a}^2 \operatorname{Ro}^2} > 0$, the growth rate, $-\mathbf{a}c_i = -\frac{1}{\operatorname{Re}}(b^2 + \mathbf{a}^2)$, is largest for $b = 0$

and it is equal to $-\frac{1}{\operatorname{Re}}\mathbf{a}^2$. Since the maximum growth rate is negative, we reach the

useful conclusion that all disturbances associated with the continuous spectrum decay

with time for all $Ri_b \geq 0$. Therefore all disturbances decay for neutral and stable stratification (for $Pr = 1$). Furthermore, because the real part of the eigenvalues satisfy the dispersion relationship for inertial-gravity waves (Apel, 1990), we can interpret the asymptotic nature ($z \rightarrow \infty$) of the disturbances as damped, plane inertial-gravity waves. The case for $Pr \neq 1$ is algebraically much more complex and is beyond the scope of this simple discussion.

VITA

James Coles Barnard

University of Washington

2000

Mr. Barnard has graduate degrees from the University of Washington (M.S., Applied Mathematics) and the Massachusetts Institute of Technology (M.S., Meteorology). He currently is a Senior Research Engineer at Pacific Northwest National Laboratory. His areas of expertise include applied mathematics, fluid mechanics, and radiative transfer with particular emphasis on applications of these disciplines to the atmosphere.